MECHANICS OF DEFORMATION AND FAILURE IN RECHARGEABLE BATTERY MATERIALS

A Dissertation
Presented to
The Academic Faculty

by

Xueju Wang

In Partial Fulfillment
of the Requirements for the Degree
Doctor of Philosophy in the
School of MECHANICAL ENGINEERING

Georgia Institute of Technology
December, 2016

MECHANICS OF DEFORMATION AND FAILURE IN RECHARGEABLE BATTERY MATERIALS

Approved by:

Dr. Shuman Xia, Advisor
School of Mechanical Engineering
Georgia Institute of Technology

Dr. Gleb Yushin
School of Materials Science and Engineering
Georgia Institute of Technology

Dr. Hailong Chen
School of Mechanical Engineering
Georgia Institute of Technology

Dr. Min Zhou
School of Mechanical Engineering
Georgia Institute of Technology

Dr. David McDowell
School of Mechanical Engineering
Georgia Institute of Technology

Dr. Ting Zhu
School of Mechanical Engineering
Georgia Institute of Technology

Date Approved: August 12, 2016

To my family.

ACKNOWLEDGEMENTS

While my thesis is turning into its final shape, I start to look back my four and half years' life at Georgia Tech. I feel so lucky to have so many great people to inspire me and assist me to go through this journey. Without them, this thesis would not have been possible.

First, I would like to express my deepest gratitude to my advisor, Dr. Shuman Xia, for his invaluable guidance and continuous support for my Ph.D. study and research. Shuman admitted me to Georgia Tech four and half years' ago and has guided me with enormous patience. His vast knowledge and enthusiasm for science have greatly influenced me. His critical and creative thinking have shaped my research. I also have learned a lot from his emphasis on understanding the essential physics when approaching a problem. Shuman is also an exceptional motivator. I have learned from his perseverance. The times of starting from scratch and trial and error in carrying out my project are still vivid in my memory. Without substantial persistence and continuous efforts, the project cannot come to fruition. I feel so lucky to have the opportunity to learn those great traits from him during my Ph.D. study and carry them forward throughout the rest of my research career.

Deep gratitude is also due to the other members of my thesis committee, Dr. David McDowell, Dr. Min Zhou, Dr. Ting Zhu, Dr. Hailong Chen, and Dr. Gleb Yushin for their insightful suggestions and comments on this thesis. Their interest and appreciation gave me incredible confidence to carry on this research.

I would also like to convey my appreciation to the training and generous help from the staff members, Charlie Suh, Hang Chen, Chris Yang, John Pham, and Eric Woods, at the institute for electronics and nanotechnology at Georgia Tech.

I also wish to express my sincere thanks to my labmates, Jingwen Zhang, Neng Wang, Zhipeng Pan, Noah Dennis, Avery Yang, Mu Lu, and Marc Papakyriakou for their great assistance and accompany. I would like extend my gratitude to my other friends, Dr. Yan Li, Dr. Yifan Gao, Dr. Feifei Fan, Dr. Ran Liu, Dr. Weijian Diao, Dr. Yunya Zhang, Dr. Yiling Dai, Dr. Tianyuan Xie, Yitao Liu, Yuan Li, Hao Luo, Zhi Zeng, Tianyuan Liu, Seokpum Kim, and Xu Du. Their kind help and the friendship with them have made my Ph.D. life so enjoyable.

Finally, I would like to dedicate this thesis to my family. Thanks for my parents, my sisters, and my brother for their unconditional love, support, and encouragement. I feel so lucky to grow up in such a big family and appreciate so much for the sacrifices my parents have made for us. I also would like to thank my husband, Yi Zhang, for his enormous love and support along this journey. We have grown a lot together through the years. Our daughter, Amy Zhang, has brought so much fun to my life and makes me feel much stronger both physically and spiritually than I have ever imagined. Deep gratitude is also due to my parents-in-law for their love and support.

TABLE OF CONTENTS

LIST OF TABLES

Page

LIST OF FIGURES

Page

LIST OF SYMBOLS

a	center-to-corner distance of an indent
a_{c}	crack length
$\alpha_i (i = 1, \ ..., m)$	parameters used to describe the displacement field
$\beta(\xi)$	volume change of solid
c	average radial crack length in residue indents
C	cross-correlation function
$C^{\mathrm{A}}, C^{\mathrm{B}}$	The stoichiometric concentration of species A and B
D	diffusion coefficient of guest species A in $\mathrm{A}_{\xi}\mathrm{B}$
δ_{ij}	Kronecker delta
$\nabla \mathbf{U}(\mathbf{X}_0)$	gradient of displacement at $\mathbf{X}_0$
$\mathrm{erf}(\cdot)$	Gauss error function
E_{ij}^{c}	compositional strain
E_{ij}^{e}	elastic strain
E_{ij}^{p}	plastic strain
ε_{ij}^{e}	infinitesimal elastic strain
$\varepsilon_{\mathrm{m}}^{\mathrm{e}}$	the hydrostatic part of elastic strain
$\left(\varepsilon_{ij}^{\mathrm{e}}\right)^{\mathrm{dev}}$	the deviatoric part of the elastic strain
ε_{R}	reaction-induced strain

ε_{xx}, ε_{yy}	horizontal and vertical strain components
$\lvert \varepsilon_{xx}^{\mathrm{m}} \rvert, \lvert \varepsilon_{yy}^{\mathrm{m}} \rvert$	absolute mean strain components
E, E_s	Young's modulus
f	image at the reference configuration
F_{kl}^{c}	deformation gradient related to volume change
F_{ik}^{e}	elastic deformation gradient
F_{lj}^{p}	plastic deformation gradient
Φ	sum-squared difference function
Ψ	factor related to the elastic mismatch ratio
g	image at the deformed configuration
G_{c}	fracture energy
G_c^0	fracture energy with ion concentration ξ_0
$G_{\mathrm{c}}^{\mathrm{eff}}$	effective fracture energy
h_f^0, h_f	initial film thickness and film thickness after lithiation
h_s	the thickness of the substrate
J	J-integral
J_i	flux of guest species
K_{IC}	fracture toughness
K_{IC}^F	film stress component of fracture toughness
K_{IC}^W	wedging component of fracture toughness
K_{IC}^E	elastic component of fracture toughness

k_{B}	Boltzmann constant
κ_1	curvature changes in the substrate induced by film sputtering
κ_2	curvature changes in the substrate induced by electrochemical testing
ξ	molar concentration of A in $\mathrm{A}_{\xi}\mathrm{B}$
χ	dimensionless parameter denoting the normalized gradient of fracture energy
χ^W, χ^E	semi-empirical constants
l_c	characteristic crack length
L	finite element size
L_{ij}^e	elastic velocity gradient
L_{ij}^c	velocity gradient due to the insertion of guest species
L_{ij}^p	velocity gradient due to plastic flow
μ	electrochemical potential of guest species
μ_{chem}	the potential of solid due to chemical reactions
n_i	unit outward normal
ν	Poisson's ratio
υ_s	Poisson's ratio of the substrate
$N_i(\mathbf{X})$	polynomial shape functions
Ω	a parameter relating the guest species concentration to the volume change of the ionic solid
$\tilde{\Omega}$	a parameter relating the mechanical response of the solid to its electrochemical potential
P	peak indentation load

σ	in-plane biaxial stress
r_{p}	cohesive zone size
σ_{m}	strength of the interphase
σ_{ij}^{dev}	deviatoric stress
σ_{Y}	yield stress
$\sigma_{u_x}, \sigma_{u_y}$	standard deviations of displacement
$\sigma_{\varepsilon_{xx}}, \sigma_{\varepsilon_{yy}}$	standard deviations of strain
$\sigma_{ij}^{PK1}, \sigma_{ij}^{PK2}$	first and second Piola-Kirchhoff stresses
T	temperature
Γ	contour
u_x^0, u_y^0	rigid-body displacement components of the unreacted Si region
$\mathbf{U}(\mathbf{X})$	displacement vector at $\mathbf{x}$
$\mathbf{U}_{\mathrm{Trial}}(\mathbf{X})$	trial displacement field
u_x, u_y	horizontal and vertical displacement components
v_c	crack growth velocity
v_{app}	applied crack growth velocity
V_Γ	the crack tip domain bounded by Γ
w^{e}	elastic energy density
w^p	plastic potential
x	molar ratio of Li to Ge
$\mathbf{x}$	coordinates in the reference description
X	coordinates in the deformed description

$\mathbf{x}_0$	center of the subset

SUMMARY

Rechargeable batteries are the current dominant energy storage solution for portable electronics, electric vehicles and stationary power management. The growing demand in these applications, however, requires next-generation batteries with an unprecedented combination of low cost, high capacity, and high reliability. To meet this end, much of the research effort has focused on developing new electrode and electrolyte materials with improved performance. Nevertheless, the mechanical degradation and failure in these materials during electrochemical cycling have hindered their wider use in advanced batteries. To obtain a thorough understanding of the deformation and fracture characteristics of these battery materials, an integrated experimental and computational investigation is presented in this study.

We have conducted a nanomechanical study on the damage tolerance of electrochemically lilthiated silicon. Both in-situ transmission electron microscopy (TEM) experiments and quantitative fracture toughness measurements by nanoindentation reveal a rapid brittle-to-ductile transition of fracture as lithiation proceeds. The mechanistic underpinnings of this transition are elucidated by molecular dynamics simulations and attributed to atomic bonding and lithiation-induced toughening. We also present experimentally measured fracture toughness of lithiated germanium by nanoidentation for the first time, which is found to increase monotonically with increasing Li concentration. A comparison between the fracture energy of lithiated germanium and that of lithiated silicon reveals that germanium possesses much higher fracture resistance than Si in the

lithiated state and thereby is a potential candidate for durable, high-capacity, and high-rate lithium-ion batteries.

In this work, we have also developed a nanoscale deformation analysis method and applied it to investigate the deformation of electrode materials. A widely used full-field, noncontact deformation measurement method, digital image correlation analysis, is performed on high-resolution TEM images of lithiated amorphous silicon ($a-\mathrm{Si}$). We show that the lithiation in $a-\mathrm{Si}$ occurs by the movement of an atomistically sharp phase boundary between the $a-\mathrm{Si}$ product and an amorphous $a-\mathrm{Li}_x\mathrm{Si}$ product ($x=2.33$).

Informed by the experimentally measured fracture and deformation characteristics of electrode materials, we develop a computational cohesive zone model and integrate it with a chemo-mechanical two-way coupling continuum model. This integrated computational framework is applied to investigate the effective fracture properties of ion-storage materials and fracture behaviors of lithiated nanostructures.

This highly integrative experimental and computational work has profound implications for the design and development of next-generation, high-performance rechargeable batteries. Furthermore, the proposed experimental and computational methodologies can be applied to study other nano- or micro-structured electrode/electrolyte architectures in various electrochemical systems.

CHAPTER 1 INTRODUCTION

1.1 Background and motivation

1.1.1 High-performance electrode materials for lithium-ion batteries

Energy storage with high performance and low cost is critical for applications in consumer electronics, zero-emission electric vehicles, and stationary power management [1, 2]. Lithium-ion batteries (LIBs) are a widely used energy storage system due to their superior performance [3-5]. There is, however, increasing demand for LIBs with high capacity, good cyclability, and high safety. Many companies are already planning concepts around the promise of cheaper, higher-capacity batteries. Tesla, one of the major electric automakers, is building a $5 billion gigafactory aiming to reduce the per-kilowatt-hour cost of its LIB packs by over 30% by the end of 2017. The reduced cost in batteries can enable an electric car that is 50% cheaper than its current luxury Model S.

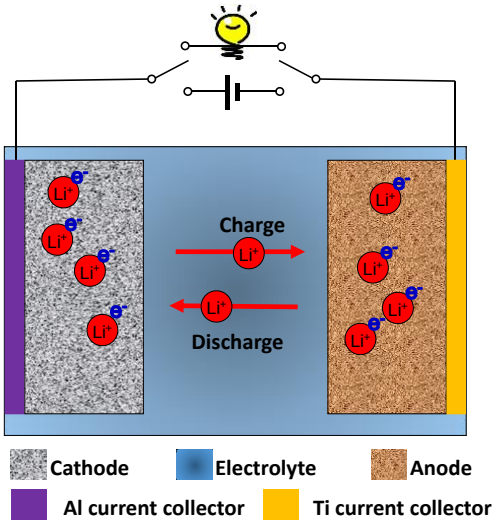

Figure 1.1 Illustration of the working principle of a lithium-ion battery.

A LIB consists of three major components: anode, cathode, and electrolyte (Fig. 1.1). The anode and cathode materials are solids that serve as lithium-ion hosts. During charging and discharging of a LIB, the lithium ions migrate back and forth between the two electrodes through the electrolyte. The energy storage capacity of a battery is proportional to the maximum amount of lithium that can be hosted in the electrode materials. Much of the research effort to-date has been devoted to developing new electrode materials that can store more lithium ions than the current available technology.

In commercial LIBs, graphite of 372 mAh g^{-1} capacity is being used as the anode material [6, 7]. However, there is a strong tendency to replace graphite with other high-capacity anode materials such as silicon (Si) of 3579 mAh g^{-1} capacity [8, 9] and germanium (Ge) of 1384 mAh g^{-1} capacity [10]. One major drawback of these high-capacity anode materials is the huge volume change of nearly 400% during cycling [11, 12]. This large volume deformation, when occurring inhomogeneously or under mechanical constraint, can cause high tensile stress to develop, resulting in massive electrode cracking and fracture [13]. Fracture causes the loss of active materials and yields more surface areas for solid electrolyte interphase (SEI) growth, both of which contribute to the fast capacity fade of LIBs.

To mitigate the mechanical degradation in LIBs, it is essential to quantitatively understand the electrochemically-induced mechanical responses as well as the fundamental mechanical properties of high-capacity electrode materials. The past decade has witnessed a marked increase in studies on the mechanical behaviors of high-capacity electrode materials [14-29]. Focusing on the promise of Si and Ge as the next-generation anode materials, significant progress has been made in the experimental measurement

and modeling of lithiation/delithiation-induced stresses [19, 30], lithium-concentration dependent modulus and hardness[31-33], time-dependent creep [33, 34], and strain-rate sensitivities [35]. However, there is still a critical lack of fundamental understanding on the fracture-related properties [36, 37], which ultimately dictate the resistance of the electrode material to mechanical degradation and failure.

1.1.2 Nanoscale deformation analysis in electrode materials

In addition to the fracture properties, recently the fundamental mechanisms of electrochemical reaction, microstructural evolution, and mechanical degradation in various rechargeable battery electrodes have also been extensively investigated by *in situ* transmission electron microscopy (TEM) at the nanoscale. However, much of the TEM work till date has been focused on direct imaging and crystallographic analysis. Quantitative deformation measurement is still lacking.

Due to its high accuracy and ease of use, the technique of digital image correlation (DIC) has emerged as a powerful tool for conducting full-field, noncontact deformation measurement [38-41]. In a DIC analysis, the displacement distribution of a test specimen is obtained by correlation comparison between two high contrast digital speckle images taken from the deformed and undeformed states. The use of image correlation, as opposed to tracking the movement of individual pixels, allows full-field displacement data to be measured at the sub-pixel level. Combined with various optical imaging methods, DIC has been used for a wide spectrum of applications across multiple length scales, ranging from landslide monitoring using high-resolution satellite imagery [42] to microscale deformation analysis of biological tissues [43].

Driven by the recent advances in materials and biological research, there is a growing need for quantitative deformation analysis at the nanoscale. Due to the diffraction of visible light, the standard optical microscopy has a limited spatial resolution about half the light wavelength, thus invalidating the optical-based DIC method for nanoscale deformation measurement. To resolve this issue, attempts have been made to combine DIC with other high-resolution microscopy techniques. The high-resolution transmission electron microscopy (HRTEM) offers a unique capability for characterizing internal material structures with sub-atomic spatial resolution [44, 45]. Quantitative full-field analysis of TEM images with DIC analysis can provide unprecedented nanoscale characterization capabilities that are not possible with optical and SEM-based DIC. The nanoscale deformation analysis method can be applied to study the deformation in electrode materials during electrochemical testing.

1.1.3 Computational modeling of fracture in ion-storage materials

In parallel with the experimental studies on deformation and fracture in LIBs, extensive computational work has also been conducted in this field. As previously discussed, in ion-storage material systems, ion transport and diffusion often induce large volumetric change, which, if not accommodated appropriately, generates substantial stress. The stress can cause the fracture and ultimate failure of these material systems. For the rational design of energy storage and conversion systems using ion-storage materials, the effects of both electrochemical and mechanical driving forces on fracture must be thoroughly understood.

The general thermodynamic framework accounting for stresses associated with compositional change was established by Larche and Cahn [46], which was initially

developed for metallic systems [47-50] and later extended to ionic solids [51-53]. For example, a stress-dependent electrochemical potential has been developed for ionic solids and applied to study the stress-transport interaction in the electrolyte as well as stress-oxidation interaction in alloys for solid oxide fuel cells [54-58].

To address the stress buildup problem, extensive work has been conducted for experimental measurement [19, 59] as well as modeling of stresses [60-64] in electrode materials. Christensen and Newman are among the first to study the coupling between mechanical stress and Li diffusion in electrode materials using a mathematical model for diffusion-induced stresses [65, 66]. The model was subsequently extended to include elastic-plastic material behaviors and large deformation [60, 67-70]. In addition, analytical approaches have been taken to derive closed-form relationships among relevant quantities to characterize stress buildup in electrode materials [17, 64, 71]. The experimentally measured as well as theoretically computed stresses are further used to derive critical conditions under which electrode materials may fracture [72-76]. Fracture within solid electrodes caused by diffusion-induced stresses has been investigated extensively in literature, including the estimation of critical crack size using Griffith's criterion [77] and the study of electrode size and cycling rate effects on fracture by employing the stress intensity factor and strain energy release rate criteria [27, 78, 79]. In addition, a cohesive zone approach has also been used to study crack nucleation and propagation in electrode materials [80, 81] by assuming a constant fracture energy value.

In ion-storage materials, the interaction between ions and stress fields around the crack tip has a profound influence on the fracture behaviors of these material systems. Such interaction has been widely studied in the context of hydrogen diffusion in metals

by considering solute trapping at material defects and plasticity ahead of the crack tip. It has been suggested that in ion-storage materials, high ionic mobility as well as diffusion-deformation coupling in these material systems can facilitate fast ion redistribution around the crack tip, and thus might alter the effective fracture resistance at the macroscopic scale. Despite its importance, the intriguing interaction between ion diffusion and crack growth remains poorly understood.

1.2 Objective, scope and organization of this thesis

This thesis is to employ an integrated experimental and computational approach to study the deformation and fracture in rechargeable battery materials with a focus on the following three sub-objectives:

(1) Quantitative measurements of the fracture properties of high-capacity anode materials as lithiation proceeds.

(2) Nanoscale deformation analysis in lithiated electrode materials.

(3) Continuum modeling of fracture in ion-storage materials for fuel cells and batteries.

The remainder of this thesis is organized as follows. In Chapter 2, the fracture properties of high-capacity electrode materials are investigated to achieve objective (1). In-situ TEM experiments and quantitative fracture toughness measurements by nanoindentation are conducted to study the damage tolerance of lithiated Si. The experimental results are elucidated by performing molecular dynamics modeling. The developed experimental technique is also used to characterize the fracture properties of lithiated germanium. Chapter 3 is dedicated to objective (2) by quantitatively studying the deformation in electrode materials during electrochemical cycling inside a TEM. A

method based on the digital image correlation analysis of high-resolution TEM images is developed and applied to the nanoscale deformation analysis of a two-phase lithiation process in amorphous Si. Informed by the fracture and deformation analysis in Chapters 2 and 3, a computational cohesive zone model is developed and integrated with a chemo-mechanical two-way coupling continuum model in Chapter 4 to study the effective fracture properties of ion-storage materials and fracture behaviors in lithiated Si and Ge nanostructures. Chapter 5 summarizes contributions of this study and future research directions.

CHAPTER 2 FRACTURE MECHANICS OF HIGH-PERFORMANCE ELECTRODE MATERIALS FOR LITHIUM-ION BATTERIES

2.1 High-damage tolerance of electrochemically lithiated silicon

2.1.1 Introduction

Si is a promising anode material candidate for next-generation LIBs because of its high capacity. Nevertheless, the large volume changes of Si during electrochemical cycling lead to substantial stresses and the fracture of electrodes. In this section, we conducted an integrated experimental and computational study on the damage tolerance of lithiated Si. An *in situ* nanomechanical bending test was performed on a partially lithiated Si nanowire inside a transmission electron microscope (TEM). In addition, we conducted systematic measurements of the fracture toughness of lithiated Si thin films with nanoindentation. We also performed continuum finite element (FE) and molecular dynamics (MD) simulations to interpret these experimental findings, thereby gaining mechanistic insights into the fracture mechanisms of lithiated Si. These results have important implications for the development of durable Si-based anodes for next-generation LIBs.

2.1.2 Methods

In situ electrochemical and bending tests of Si nanowires. Figures 2.1a and 2.1b show the schematic illustrations of *in situ* electrochemical lithiation and fracture testing of a single Si nanowire inside a TEM. The nano-sized electrochemical cell [82] consisted

of a Si nanowire on Si substrate as the working electrode and a Li probe as the counter electrode; the native Li_2O layer on Li surface served as a solid electrolyte. The $\langle 111 \rangle$-oriented single crystal Si nanowire had an initial diameter of about 142 nm. To start the lithiation, the Li probe was brought into contact with the free end of the Si nanowire and then a bias voltage of -2 V was applied between the working and counter electrodes. After the lithiation experiment, the partially lithiated Si nanowire was subjected to *in situ* compression by the Li probe, as shown in Fig. 2.1b.

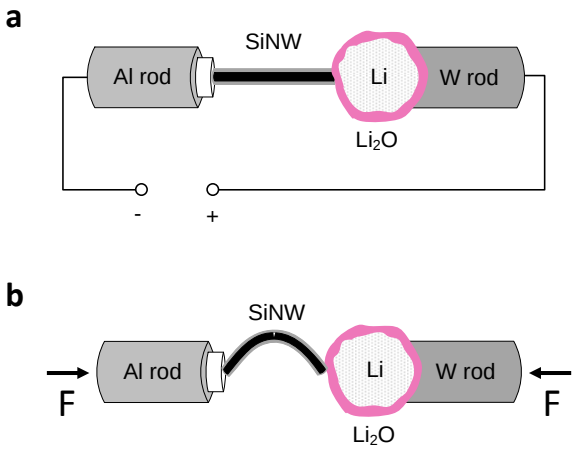

Figure 2.1 (a) Schematic of the *in situ* TEM setup for a nano-sized electrochemical cell. (b) Schematic of the buckling and bending test of a partially lithiated Si nanowire subjected to the compressive force F.

Fracture toughness measurements of lithiated Si. To quantitatively study the damage tolerance of electrochemically lithiated Si at different Li concentrations, we employed an in-house developed nanoindentation system to characterize the fracture toughness of *a*-Li_xSi, a property that describes the ability of a material to resist crack propagation [83].

Thin-film electrode fabrication and electrochemical cell assembly. The electrodes for nanoindentation tests were fabricated in a thin-film form by sputter deposition. Single-side polished titanium (Ti) plates with a thickness of 0.5 mm were used as substrates for fabrication of thin-film electrodes, and they also served as current collectors for electrochemical measurements. Before a Ti substrate was placed inside the deposition system (Denton Discovery RF/DC Sputterer), it was etched with 5% HCl to remove the surface Ti oxide. A 26 nm Ti thin film was first sputtered onto the polished side of the Ti substrate, followed by the deposition of a 350 nm-thick Si film. The Ti interlayer, serving as an adhesion promoting layer, was prepared by DC sputtering of a Ti target (3" diameter disc, 99.995% Ti, Kurt J. Lesker Co., Livermore, CA) at a power of 53 W and a pressure of 6.29 mTorr of argon. The Si film was prepared by RF magnetron sputtering of an Si target (3" diameter disc, 99.995% Si, Kurt J. Lesker Co., Livermore, CA) at a power of 200 W and a pressure of 5 mTorr of argon. Previous studies have shown that Si thin films formed under these sputtering conditions are amorphous [60].

After Si was deposited on the polished side of the Ti substrate, a thin layer of polydimethylsiloxane (PDMS) was coated on the unpolished side of the Ti substrate to prevent the formation of a solid electrolyte interphase (SEI) layer on the Ti surface. The Si film-coated Ti electrode was then assembled into a custom-fabricated Teflon electrochemical cell with a glass window (Fig. 2.2) inside an argon-filled glove box that was maintained at less than 0.1 ppm of O_2 and H_2O. A Li foil was used as the reference/counter electrode, and 1 M of lithium hexafluoro-phosphate ($LiPF_6$) in 1:1:1 (weight %) ratio of ethylene carbonate (EC) to dimethyl carbonate (DMC) to diethyl carbonate (DEC) was used as the electrolyte.

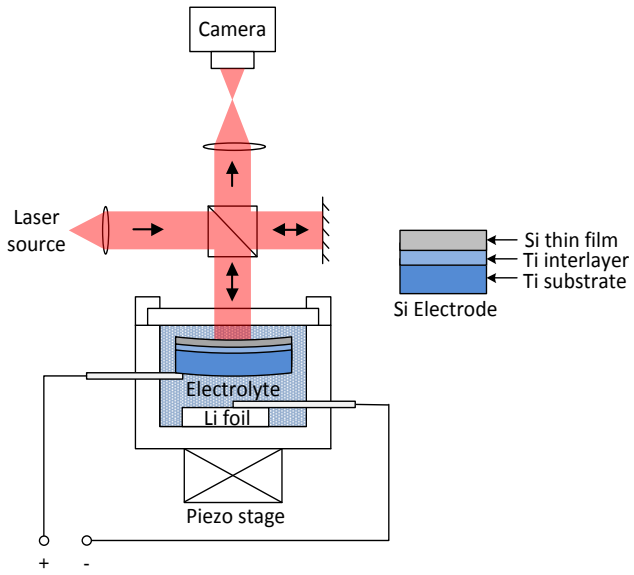

Figure 2.2 Schematic illustration of an electrochemical cell, consisting of a Si thin-film working electrode, a liquid electrolyte, and a Li foil counter electrode, as well as a Michelson interferometer setup for *in situ* film stress measurement.

Electrochemical measurement. The electrochemical measurement was conducted with a battery tester (UBA 5, Vencon Technologies, Ontario, Canada). Five electrode samples were first lithiated galvanostatically at 20 μA cm^{-2} with pre-determined cutoff potentials. The lithiation was followed by delithation at the same current density until potentials of 0.2-0.3 V versus Li/Li^+ above the cutoff potentials for lithiation were reached. Subsequently, delithiation was continued potentiostatically until the current was reduced below 0.2 μA cm^{-2}. The Si electrodes were then removed from the cell inside the glove box and thoroughly cleaned by rinsing them with DMC.

Electrochemical and in situ film stress measurement. The electrochemical measurement was conducted with a battery tester (UBA 5, Vencon Technologies, Ontario, Canada). Five Si electrode samples were first lithiated galvanostatically at 20 μA cm^{-2} with pre-determined cutoff potentials. The lithiation was followed by delithation at the same current density until potentials of 0.2-0.3 V versus Li/Li^+ above the cutoff

potentials for lithiation were reached. Subsequently, delithiation was continued potentiostatically until the current was reduced below 0.2 μA cm^{-2}. The Si electrodes were then removed from the cell inside the glove box and thoroughly cleaned by rinsing them with DMC. Stress evolution in the Si films during lithiation and delithiation was measured by monitoring the substrate curvature with a Michelson interferometer. The biaxial film stress was deduced from the measured curvature using Stoney's equation [84] in the form of

$$\sigma = \frac{E_s h_s^2}{6h_f(1-\upsilon_s)}(\kappa_1 + \kappa_2), \tag{2.1}$$

where σ is the average in-plane biaxial stress in the film, E_s and υ_s are the Young's modulus and Poisson's ratio of the substrate, h_s is the thickness of the substrate, and κ_1 and κ_2 are the curvature changes in the substrate induced by the film sputtering and electrochemical lithiation/delithiation processes, respectively. The thickness of the lithiated Si film (h_f) is given by

$$h_f = h_f^0(1+0.72x), \tag{2.2}$$

where h_f^0 is the initial thickness of the film, and *x* is the molar ratio of Li to Si (*x* = 0 for pristine Si; *x* = 3.75 for fully lithiated Si). This expression reflects the fact that the volume expansion is 370% at full lithiation [85, 86] and assumes a linear relationship between the volume expansion and the lithium concentration.

Fracture toughness measurement by nanoindentation. An in-house developed nanoindentation system situated inside an argon-filled glove box, as shown in Fig. 2.3, was employed to measure the fracture toughness of lithiated electrodes. Peak loads,

ranging from 1 to 93 mN at constant loading and unloading rates of 500 μN s^{-1}, were used during nanoindentation tests. Ten indents at each load were made for each Si electrode sample and spaced 100 μm apart. The indented Si electrodes were imaged by a Zeiss Ultra60 field-emission scanning electron microscope (FE-SEM, Carl Zeiss Microscopy, LLC, North America, Peabody, MA) operated at an accelerating voltage of 5 kV. During the sample transfer from the glove box to the SEM chamber, the lithiated Si electrodes were coated with a thin layer of anhydrous DMC to avoid the reaction of lithiated Si with ambient oxygen and moisture.

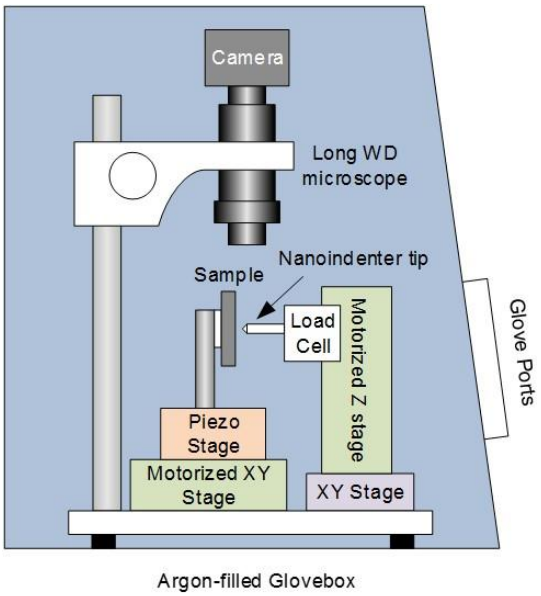

Figure 2.3 Schematic diagram of an in-house developed nanoindenter for fracture toughness measurement. The nanoindenter is situated inside an argon-filled glove box to avoid exposure of the test material to ambient humidity and oxygen.

The fracture toughness of the lithiated Si electrodes was deduced from the peak indentation loads, the indent sizes, the dimensions of indentation-induced radial cracks, and the measured film stress and thickness using the Morris model [87, 88]. Many nanoindentation models, such as the well-known Oliver-Pharr model [89] and Lawn-

Evans-Marshall (LEM) model [90], have been developed for the mechanical property characterization of bulk materials. When these models are applied for thin film measurement, the indentation depth should be limited to a small fraction of the film thickness. However, the Morris model used in this work has been developed taking the substrate effect into consideration, and is therefore suitable for fracture toughness measurement of thin films without any constraint on the indentation depth. The validity and accuracy of this indentation model has been demonstrated by both theoretical analysis and experimental results [88].

In the Morris model, thin film cracking caused by a sharp indenter tip is governed by the pre-existing film-stress field and two elastic stress fields due to indentation, i.e., a short-range "wedging" stress field and a long-range elastic-contact stress field. The fracture toughness of the test material is comprised of three components arising from these stress fields:

$$K_{IC} = K_{IC}^{F} + K_{IC}^{W} + K_{IC}^{E}. \tag{2.3}$$

The three components are then calculated by the following formulas:

$$K_{IC}^{F} = \Psi\sigma\left(h_f\right)^{1/2}, \tag{2.4}$$

$$K_{IC}^{W} = \chi^{W}\frac{P}{c^{3/2}}\left[\frac{c}{a} + \frac{a}{c}\ln\frac{2c}{a}\right], \tag{2.5}$$

$$K_{IC}^{E} = \chi^{E}\frac{P}{c^{3/2}}\left[\frac{c}{a}\right], \tag{2.6}$$

where P is the peak indentation load, and χ^{W} and χ^{E} are semi-empirical constants relating the wedging and elastic-contact components to the probe acuity and the Poisson's ratio of the material. Ψ is a factor related to the elastic mismatch ratio between the

substrate and the film. Parameter a refers to the center-to-corner distance of the indent, and c refers to the average radial crack length measured from the center of the indent to the ends of the radial cracks.

Atomistic modelling of fracture in lithiated Si. To elucidate experimental results, molecular dynamics simulations were performed using the large-scale atomic molecular massively parallel simulator (LAMMPS). Atomic interactions were modeled by a reactive force field developed for Li-Si alloys[30]. The *a*-Li_xSi samples were prepared from melting-and-quenching simulations with a quench rate of 2×10^{12} K s^{-1}. In these simulations, the initial structures were created by randomly inserting Li atoms into a crystalline Si lattice. After quenching at zero stresses, the *a*-Li_xSi samples had the final dimensions of ~16 nm × 10 nm × 1.5 nm. A sharp crack with a length of ~3 nm was created in each sample. The pre-cracked samples were then loaded in tension with a strain rate of 5×10^{8} s^{-1}, while the system temperature was maintained at 5 K. Periodic boundary conditions were applied along the loading and the thickness directions. A plane-strain condition was imposed by fixing the thickness of the simulation box. The time step in all the MD simulations was 1 fs.

2.1.3 Results and discussion

***In situ* electrochemical and bending tests of Si nanowires.** Because Li diffusion/reaction on the surface of Si is much faster than that in the bulk [22], Li ions first migrated preferably along the free surface of the Si nanowire and then diffused towards its center. In the bulk of the Si nanowire, lithiation proceeded in a core-shell mode, yielding a core of crystalline Si (*c*-Si) and a shell of amorphous Li_xSi (*a*-Li_xSi, $x \approx 3.75$). The core-shell interface was atomically sharp and oriented parallel to the

longitudinal axis of the nanowire [20]. Across this interface, an abrupt change of Li concentration occurred, resulting in high compressive stresses near the core-shell interface (*i.e.*, behind the lithiation front) [91]. The lithiation-induced compression slowed down and eventually stalled the movement of the interface. At the end of the lithiation process, the diameter of the unlithiated *c*-Si core was 85 nm; the thicknesses of the *a*-$Li_{3.75}Si$ shell and the layer of lithiated surface oxide (Li_ySiO_z) were 47 nm and 17 nm, respectively.

After the lithiation experiment, the partially lithiated Si nanowire was subjected to *in situ* compression by the Li probe, as shown in Fig. 2.4. As the compressive load was increased, the nanowire buckled and subsequently bent, resulting in a single sharp kink in the nanowire. Figure 2.4b shows a zoom-in TEM image near the kinked region. It is seen that brittle fracture occurred in the unlithiated *c*-Si core, evidenced by the nearly flat fracture surfaces. The fracture strength of the *c*-Si core was determined to be about 7.7 GPa, which is consistent with the literature data on the strength of pristine $\langle 111 \rangle$-oriented Si nanowires with similar sizes. In contrast, the *a*-$Li_{3.75}Si$ shell underwent considerably large tensile deformation accompanied by pronounced lateral thinning, without observable damages such as cracking or shear banding. The lithiated surface oxide layer (Li_ySiO_z) remained coherent to the *a*-$Li_{3.75}Si$ shell and thus underwent similar straining as the latter. Figure 2.4c shows the result of a continuum FE simulation of large local deformation near the kinked region. In the FE simulation, we assumed that the brittle fracture of the *c*-Si core was a much faster process than the elastic-plastic deformation in the *a*-$Li_{3.75}Si$ shell, such that the latter occurred after the crack in the *c*-Si core had been fully formed. As a result, the large tensile deformation in the *a*-$Li_{3.75}Si$ shell was

primarily accommodated by the sliding at the core-shell interface, yielding a large crack opening in the *c*-Si core near the core-shell interface. The deformation morphology from the FE simulation (Fig. 2.4c) was in close agreement with that in the TEM image (Fig. 2.4b). The most striking observation from Figs. 2.4b and 2.4c is the large tensile (plastic) strain of ~ 47% occurring in the *a*-$Li_{3.75}Si$ shell, with a concurrent large lateral contraction (*i.e.*, thinning) of ~ 45%. Therefore, the *in situ* TEM experiment and FE simulation demonstrate that the amorphous Li-rich Si alloy (*a*-$Li_{3.75}Si$) exhibits extraordinary damage tolerance, while *c*-Si is brittle as expected.

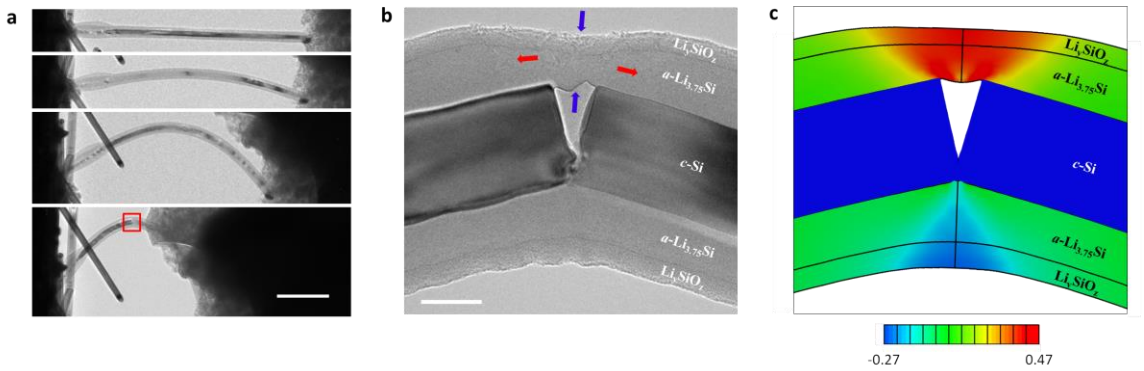

Figure 2.4 *In situ* electrochemical and bending test of a Si nanowire. (a) Sequential TEM images showing the process of axial compression; bucking and bending of the partially lithiated Si nanowire gave rise to a sharply kinked region indicated by the red box (scale bar, 1 μm). (b) Zoom-in TEM image (i.e., the red box region in (a)) showing the brittle fracture of the unlithiated *c*-Si core, as well as the large tensile deformation (red arrows) and lateral thinning (blue arrows) of the lithiated *a*-$Li_{3.75}Si$ shell (scale bar, 50 nm). (c**)** Finite element result showing the simulated elastic-plastic deformation in the nanowire that agrees with the TEM image in (**b**). Color contour reveals the distribution of axial strain in the lithiated *a*-$Li_{3.75}Si$ shell, with an extraordinarily large tensile strain of about 47% occurring in the free-standing part of *a*-$Li_{3.75}Si$.

Fracture toughness measurements of lithiated Si. To quantitatively study the damage tolerance of electrochemically lithiated Si at different Li concentrations, we

employed an in-house developed nanoindentation system to characterize the fracture toughness of *a*-Li_xSi, a property that describes the ability of a material to resist crack propagation [83]. Figures 2.5a and 2.5b show the electrochemical profiles and corresponding film stresses measured for five *a*-Si thin-film electrodes. The Li concentrations in these electrodes were controlled by galvanostatical lithiation at 20 μA cm^{-2} to different cutoff potentials. The sloping voltage profiles below 0.5 V versus Li/Li^+ suggest the formation of a single-phase *a*-Li_xSi during lithiation. As shown in Fig. 2.5b, all thin-film electrodes exhibited an initial compressive stress of about 200 MPa that resulted from the sputtering process. The compressive stress in the thin-film electrodes increased to 500-800 MPa at the end of lithiation, due to the substrate constraint on lithiation-induced volume expansion. This large residual compressive stress may impede crack growth during nanoindentation testing and thus affect the measurement of fracture toughness. To reduce the influence of those residual stresses, we first lithiated the *a*-Si electrode to a targeted Li concentration and then delithiated it to 0.25-0.3 V above the lithiation cutoff potential. During the delithiation, a small fraction of Li was extracted from the electrodes, resulting in small volume shrinkages so as to reverse the film stress from compression to tension. The tensile stress in the thin film was small, but found to be beneficial for promoting the nanoindentation-induced cracking and enabling the evaluation of fracture toughness of *a*-Li_xSi. The effects of SEI formation on electrode cracking were estimated to be negligibly small [92] and therefore were not considered in the fracture toughness measurement.

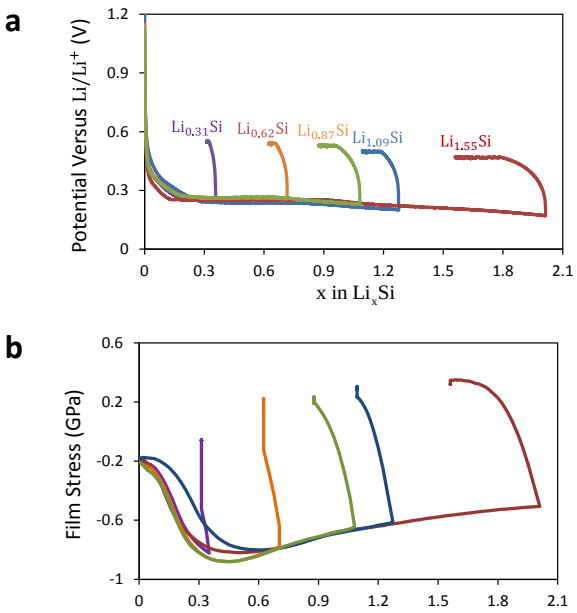

Figure 2.5 Electro-chemo-mechanical characterization of Si electrodes. (a) Electrochemical profiles of five 325 nm Si electrodes that were galvanostatically lithiated and delithiated to various Li concentrations, followed by potentiostatic delithiation. (b) Evolution of the film stress in the five Si electrodes corresponding to the electrochemical profiles in (a).

To measure the facture toughness, the *a*-Li_xSi thin-film electrodes were indented with a cube-corner indenter tip in an argon-filled glove box. Figures 2.6(a-c) show the nanoindentation results for a partially-lithiated Si electrode with low Li concentration ($Li_{0.87}Si$) under different indentation loads, which exhibit distinct cracking behaviors including (i) no cracking, (ii) indent corner cracking, and (iii) massive cracking. Specifically, under a small load of 3.92 mN, residual plastic deformation at the permanent indent was observed without obvious cracking (Fig. 2.6a). As the load was increased to 9.8 mN, three radial cracks emanated from the sharp corners of the indent (Fig. 2.6b). A further increase in the indentation load to 29.4 mN resulted in massive cracking around the indent (Fig. 2.6c). Similar cracking behaviors were observed for low Li concentrations from $x = 0$ to 1.09. However, as the Li:Si ratio was increased to above

1.56, no cracking was observed from indents for a wide range of indentation loads up to 93 mN, as shown in Figs. 2.6(d-f). Critical indentation loads separating the above three regimes of cracking behaviors are plotted in Fig. 2.6g. The two critical load curves respectively represent the upper load limit above which massive cracking occurred and the lower limit below which no crack was induced. The upper load limit curve varies substantially with the Li concentration when x exceeds 0.6, indicating that the fracture toughness of lithiated Si starts to depend sensitively on the Li concentration. Similar drastic change of the lower load limit curve can be inferred as x varies from 1.09 to 1.56 (as indicated by the dashed line), since no cracking was observed for indentation loads up to 93 mN when x = 1.56. Therefore, our results indicate that a brittle-to-ductile transition of fracture occurs when the Li composition falls in the range of x = 1.09 ~ 1.56. For $x \leq 1.09$, the indentation loads in between the two limits induced well-developed radial cracks. We used these loads to evaluate the fracture toughness of a-Li$_x$Si with the Morris nanoindentation model.

Figure 2.6h shows the measured fracture toughness, K_{IC}, as a function of Li concentration. Also shown in this figure is the fracture energy, defined as $\Gamma = K_{\mathrm{IC}}^2 / E$, where E is the Young's modulus of lithiated Si taken from the experimental measurement [32]. Figure 2.6h clearly reveals that the fracture toughness of a-Li$_x$Si alloys depends sensitively on the Li concentration. The fracture toughness and fracture energy of unlithiated a-Si are 0.51 ± 0.014 $\mathrm{MPa}\sqrt{\mathrm{m}}$ and 2.85 ± 0.15 J m^{-2}, respectively. These low values are typical of brittle materials with little fracture resistance [83]. As the Li concentration increases, the fracture resistance of lithiated Si first decreases slightly, indicating lithiation-induced embrittlement. This trend is in qualitative agreement with

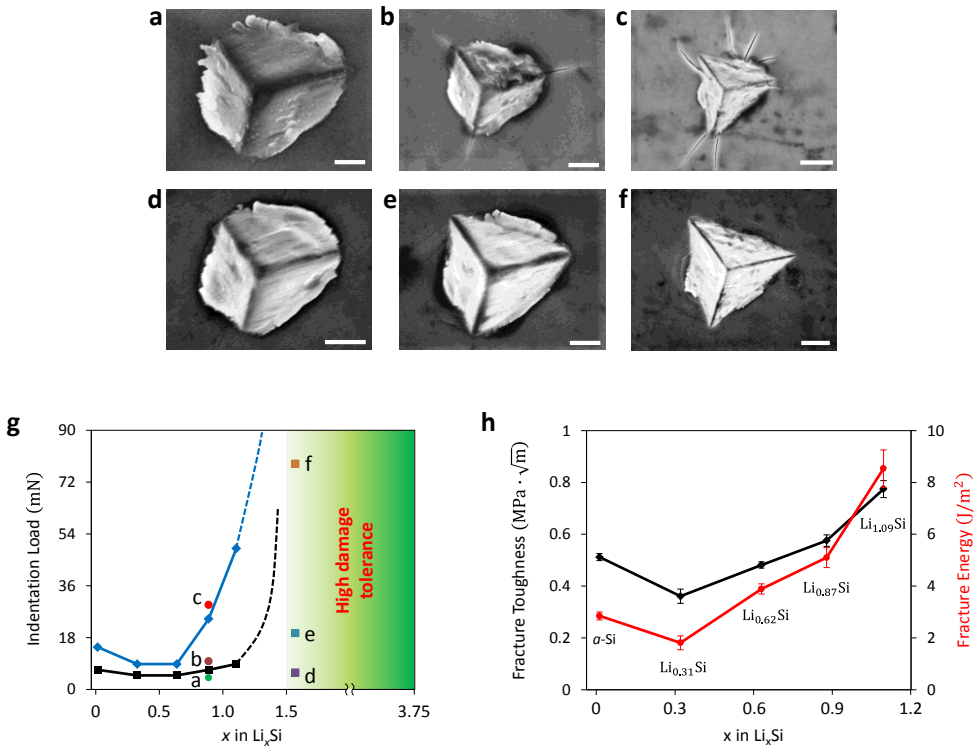

Figure 2.6 Fracture toughness measurement by nanoindentation. (a)-(c) SEM images of residual indents for a lithiated electrode of $Li_{0.87}Si$, , showing (a) no cracking, (b) radial cracking, and (c) massive cracking subjected to different applied indentation loads (scale bar: 0.5 μm in (a); 1 μm in (b); 2 μm in (c)). (d)-(f) SEM images of residual indents for a lithiated Si electrode of $Li_{1.56}Si$, showing no cracking subjected to different applied indentation loads (scale bar: 1 μm in (d) and (e); 2 μm in (f)). (g) The indentation loads (symbols) applied to the lithiated electrodes with different Li contents, corresponding to images in (a-f). The blue solid curve represents the upper load limit above which massive cracking occurred and the black solid curve the lower limit below which no crack was induced. The dashed lines show the qualitative trends interpolated from the data. (h) Fracture toughness and fracture energy of lithiated Si as a function of Li concentration.

the recent *ab initio* calculations [93] which show a small amount of Li insertion into Si substantially weakens Si-Si bonds, and hence reduces the surface energy of the material. However, upon further lithiation beyond $x = 0.31$, both the measured fracture toughness and fracture energy increase substantially with increasing Li concentration, reaching 0.77 ± 0.03 $MPa\sqrt{m}$ and 8.54 ± 0.72 J m^{-2} for $Li_{1.09}Si$, respectively. Since a further increase

in Li concentration gave rise to large residual plastic deformation at and around indents without cracking (*e.g.*, Figs. 2.6d-f), we take the Li:Si ratio of $x \approx 1.5$ as the characteristic composition above which the brittle-to-ductile transition of fracture occurs in *a*-Li_xSi alloys.

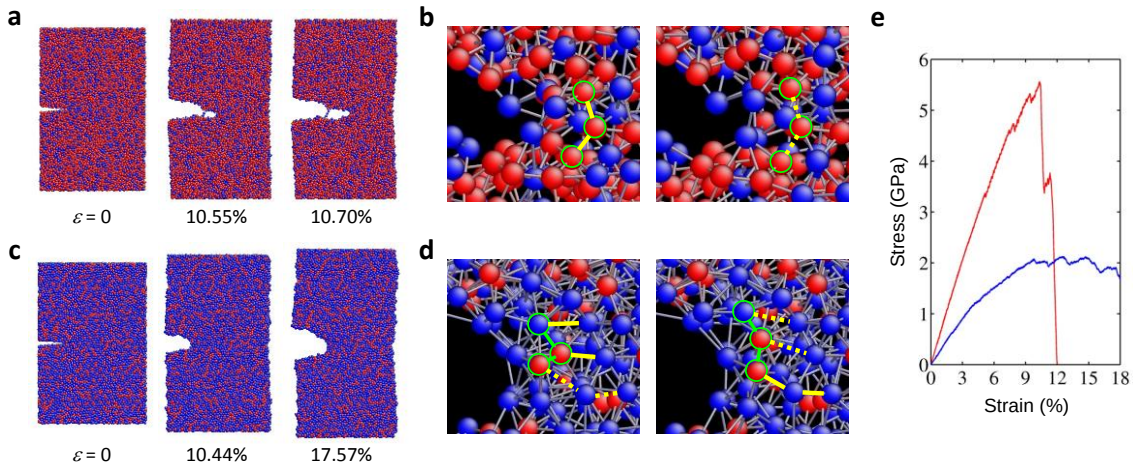

Figure 2.7 Molecular dynamics (MD) simulations. (a) MD snapshots of brittle fracture in Li-lean Si (*a*-$Li_{0.5}Si$) at various stages of applied strain load ε, showing the growth of an atomically sharp crack. (b) Zoom-in images near the crack tip in strained *a*-$Li_{0.5}Si$, showing the characteristic atomic processes of Si-Si bond breaking (from solid to dashed lines). (c) MD snapshots of ductile response in Li-rich Si (*a*-$Li_{2.5}Si$) at various stages of applied strain load ε, showing the crack-tip blunting. (d) Zoom-in images near the crack tip in strained *a*-$Li_{2.5}Si$, showing the characteristic atomic processes of bond breaking (from solid to dashed lines), formation (from dashed to solid lines) and rotation (angle change between two green lines). Si atoms are colored by red and Li by blue in (a-d). (e) Overall stress-strain responses of *a*-$Li_{0.5}Si$ (red curve) and *a*-$Li_{2.5}Si$ (blue curve).

Atomistic modelling of fracture in lithiated Si. To understand the experimentally measured brittle-to-ductile transition phenomenon, we performed MD simulations of deformation and fracture in *a*-Li_xSi alloys using the reactive force field (ReaxFF) [30]. In Fig. 2.7, we contrast the MD results by showing the brittle crack growth in Li-lean *a*-$Li_{0.5}Si$ versus the ductile crack blunting in Li-rich *a*-$Li_{2.5}Si$. In both cases, MD simulations were performed for samples containing a sharp edge pre-crack

and subjected to a far-field tensile load. Figure 2.7a presents a sequence of MD snapshots showing brittle crack growth in *a*-$Li_{0.5}Si$. In this case, the local tensile deformation near the crack tip is primarily accommodated by the stretching and breaking of Si-Si bonds, as shown in Fig. 2.7b. Due to the high fraction of strong covalent Si bonds, the bond alteration events are mostly discrete and disruptive, lacking bond reformation. A small damage zone forms near the crack tip, and it contains a high fraction of dangling bonds and atomic-sized voids. As the crack extends through such a damage zone, the crack faces become atomically rough, but the crack tip remains sharp, as seen from Fig. 2.7a. In contrast, Figure 2.7c presents a sequence of MD snapshots showing the crack blunting in *a*-$Li_{2.5}Si$. In this case, the local tensile deformation near the crack tip is accommodated by the stretching, rotation, breaking, and frequent reformation of atomic bonds, as shown in Fig. 2.7d. Several Li atoms often collectively participate in a bond-switching process, so that the amorphous structure near the crack tip remains nearly homogenous without significant damage. As a result, the crack tip becomes considerably blunt without apparent crack growth, as seen from Fig. 2.7c. In addition, we compare the stress-strain curves during tensile straining of the above two pre-cracked samples in Fig. 2.7e; the fast brittle fracture in *a*-$Li_{0.5}Si$ is manifested as a sharp load drop, while the ductile crack blunting in *a*-$Li_{2.5}Si$ is characterized by a gradual load decrease indicative of extensive plastic deformation near the crack tip. The above MD results of brittle versus ductile behaviors in Li-lean and Li-rich *a*-Li_xSi alloys are consistent with the trend in nanoindentation measurements. Hence, our MD study reveals a plausible atomistic mechanism of brittle-to-ductile transition in *a*-Li_xSi alloys, namely, the decreasing fraction of strong covalent Si bonding and the concomitant increasing fraction of

delocalized metallic Li bonding give rise to an alteration of the dominant atomic-level processes of deformation and fracture with increasing Li concentration.

The above experimental and modeling results underscore the notion of the high damage tolerance of amorphous Li-rich Si alloys and thus have important implications for the design of durable Si-based anodes for next-generation LIBs. Recently, lithiation experiments have been conducted with *a*-Si nanoparticles with a wide range of diameters up to 870 nm [25], as well as with *a*-Si pillars of a few microns in diameter [94]. In those experiments, no cracking and fracture were observed in lithiated *a*-Si electrodes. However, it has been shown that the surface layers of lithiated *a*-Si particles and wires should have underwent a large hoop tensile deformation resulting from the two-phase lithiation and associated volume expansion at curved phase boundaries [25]. Given the large hoop tension and accordingly high driving force of fracture, the lack of observed cracking [94, 95] implies that the fully lithiated *a*-Si should be mechanically robust. In this work, our *in situ* TEM and nanoindentation experiments collectively provide direct evidence for the high damage tolerance (*i.e.*, high tensile ductility and high fracture toughness) of Li-rich Si alloys, which is the essential mechanistic information for the design of durable Si-based electrodes. In addition, the quantitative fracture characteristics obtained in our work constitute an important input for optimizing the microstructures and lithiation/delithiation windows of Si-based LIBs. Incidentally, the mechanical robustness of lithiated *a*-Si is in contrast with the commonly observed surface cracking and fracture after lithiation in large *c*-Si nanostructures [24, 26]. The ease of fracture in lithiated *c*-Si has been attributed to a crystallographic effect on the lithiation anisotropy, resulting in inhomogeneous phases and deformation near the interface between anisotropically

lithiated domains [96]. For *a*-Si electrodes, there is no such lithiation anisotropy. As a result, both the lithiated phases and deformation processes in *a*-Si particles and wires are more homogenous than those in *c*-Si counterparts, which contribute to the high mechanical robustness of the former.

2.1.4 Summary

To conclude, we have integrated experiments and modeling to reveal the high damage tolerance of electrochemically lithiated Si electrodes. The *in situ* TEM experiment on a partially lithiated Si nanowire showed a striking contrast of the brittle fracture in the unlithiated Si core versus the ductile tensile deformation in the lithiated Si shell. The nanoindentation testing of amorphous lithiated Si alloys indicated a drastic increase of fracture toughness as the Li to Si ratio was increased to above 1.5. Our atomistic simulations elucidated the mechanistic underpinnings of the brittle-to-ductile transition in terms of atomic bonding and lithiation-induced toughening. The quantitative characterization and mechanistic understanding of high damage tolerance of Li-rich Si alloys represent a critical step toward the rational design of durable Si-based electrodes for next-generation LIBs. Broadly, our integrated experimental and modeling approach can be applied to the mechanical characterization of a wide range of electrochemically active materials for energy storage applications.

2.2 Fracture toughness characterization of lithiated germanium

2.2.1 Introduction

In today's commercial LIBs, graphite of 372 $mAhg^{-1}$ capacity is being widely used as the anode material [6, 7]. There has been a strong tendency to replace graphite

with other high-capacity anode materials such as silicon (Si) of 3579 $mAhg^{-1}$ capacity [8, 9] and germanium (Ge) of 1384 $mAhg^{-1}$ capacity [10]. Compared with carbon- and Si-based anodes, Ge-based ones have not been studied as much, primarily because of the higher manufacturing cost of Ge at present. Nevertheless, Ge possesses several advantages over Si as a high-performance anode material. Due to the smaller band gap of Ge (band gap energy E_g = 0.66 eV at 300 K) than that of Si (E_g = 1.12 eV at 300 K), Ge has a four orders of magnitude higher electronic conductivity [97]. Besides, the Li diffusivity in Ge is much higher than in Si (400 times faster) [10, 98]. Fast transport of both electrons and Li ions enable a high charging/discharging rate for LIBs [99-101]. Although Ge is less earth abundant than other high-capacity anode materials, the price of Ge could potentially decrease with increased interest in Ge anodes and technical improvements in the production of Ge. Furthermore, by alloying Ge with other elements such as Si, Sn, and carbon, it is possible to reduce the manufacturing cost and in the meantime to enhance the overall electrochemical and mechanical performance.

Despite the superior characteristics of Ge as a promising anode material, Ge undergoes colossal volume expansion of nearly 400% when fully lithiated [12]. This large volumetric deformation, when occurring inhomogeneously or under mechanical constraint, can cause high tensile stress to develop, resulting in massive electrode cracking and capacity fade of the battery. To minimize the mechanical stress induced by volume change, various nanostructures of Ge electrodes, such as nanowires [102], nanotubes [103], nanoparticles [99, 100], and thin films [101, 104] have been studied for improvement in capacity retention. For instance, Park et al. used a high-yielding synthetic method to fabricate Ge nanotubes, which exhibited high rate capability and capacity

retention of more than 1000 $mAhg^{-1}$ over 400 cycles [103]. Besides engineering nanostructured Ge anodes to mitigate mechanical degradation, Ge alloyed with other elements such as Si, Sn, Cu, and carbon has also been studied. Song et al. developed a Si/Ge double-layered nanotube array electrode and showed that this type of electrode demonstrated improved cyclability (capacity retention of 85% after 50 cycles) and rate capability (doubled capacity at a 3C rate) compared with homogeneous Si systems [105].

Recently, *in situ* transmission electron microscopy (TEM) has been employed to investigate the fundamental mechanisms of electrochemical reaction, microstructural evolution, and mechanical degradation in various rechargeable battery electrodes at the nanoscale [12, 85, 106]. Ge nanoparticles (GeNPs) have been found to expand isotropically upon lithiation and undergo no visible cracking after multiple charge-discharge cycles [86], in distinct contrast to the size-dependent fracture of SiNPs upon the first lithiation [24]. More recently, it has been reported that Ge pillars exhibited slight anisotropic expansion and size-dependent fracture upon lithiation, which, however, displayed a much greater critical size for fracture than its Si counterparts [107, 108]. The robust mechanical behaviors of Ge electrodes offer substantial potential for the development of durable, high-capacity, and high-rate LIBs. However, it remains largely unclear why the Ge nanoparticles and pillars are more resistant to damage and fracture. In this study, we address this issue by investigating the intrinsic fracture toughness of lithiated Ge at various levels of Li content. The fracture toughness of a material (commonly denoted by K_{IC}) is one of the key parameters describing the ability of a material to resist fracture. In the present work, the direct measurement of the fracture toughness of lithiated Ge is performed by applying a nanoindentation method that we

have previously developed [109]. Furthermore, we compare the fracture resistance of lithiated Ge with that of lithiated Si [109] and assess the suitability of the materials for use in high-performance LIBs. The quantitative fracture characteristics obtained in our work provide fundamental insights for engineering new Ge-based electrodes and optimizing the microstructures of advanced LIBs.

2.2.2 Methods

All Ge electrodes used in this study were fabricated and fracture tested with nanoindentation in the same way as the Si electrodes previously presented, and therefore will not be discussed here. It is worth noting that we performed one additional testing on the Ge electrode to study its fracture behavior over electrochemical cycling. In this testing, the Ge electrode was cycled galvanostatically at a current density of 20 $\mu A/cm^2$ between 0.01 V and 1.5 V for five cycles. A digital CMOS camera (DFK 72AUC02, Imaging Source, Charlotte, NC) equipped with a 35 mm focal length lens (HF35HA-1B, Fujinon, Stamford, CT) was used to monitor the morphological changes of the Ge electrode surface during cycling. To obtain more details of the surface morphology, the Ge electrode was further imaged with an optical microscope of higher magnification after the electrochemical testing.

2.2.3 Results and discussion

A plot of the voltage profiles from a Ge film electrode is shown in Fig. 2.8. At the initial stage of the first lithiation, the cell potential abruptly drops to below 0.7 V due to the SEI formation and irreversible lithiation of the surface GeO_2 layer. The voltage subsequently decreases slowly, indicating that the lithiation of Ge begins approximately at below 0.7 V. This trend is consistent with the previously reported data [10]. During the

lithiation and initial delithiation of the first cycle, no obvious morphological changes are observed for the Li_xGe thin films (image a, pristine Ge and image b, $Li_{2.1}Ge$). However, cracks start to form on the lithiated Ge electrode at the end of the first delithiation cycle

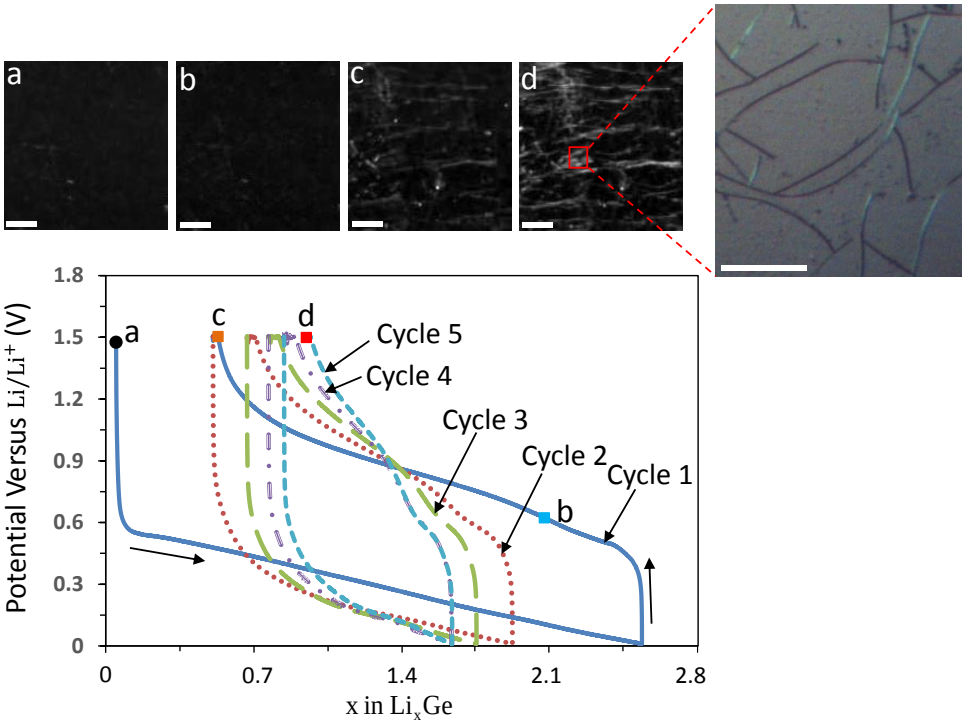

Figure 2.8 Voltage profiles of a thin-film Ge electrode during electrochemical lithiation/delithiation cycling. The arrows in the figure indicate the cycling direction. (a-d) Optical images of the Ge electrode surface corresponding to the points labeled in the figure during cycling. The zoom-in image is an optical micrograph that shows cracks in image d. The scale bars are 500 μm in (a-d) and 100 μm in the zoom-in image.

(image c, $Li_{0.5}Ge$). Further lithiation/delithiation of the Ge electrode causes massive cracking (image d). As previously stated, the cracking is induced by high tensile stress developed due to the colossal volumetric deformation of the electrode during cycling. Cracking of the electrode leads to loss of electrical contact and results in more surface area for SEI growth. Both factors cause rapid capacity fading of the system. It is worth noting that Nadimpali et al. have recently studied the mechanical response of Ge thin-

film electrodes during electrochemical cycling and have shown that their Ge films experience no cracking after the first lithiation/delithiation cycle [104]. Such discrepancy might be attributed to a variety of factors such as difference in film thickness, cycling rates and cut-off voltages, and pre-existing defects in the film and at the interface. Compared with the Ge films in their work, the films used in this work have a two times larger thickness, and are cycled with a three times faster rate and an 80% lower cut-off voltage during lithiation, all of which may facilitate crack formation and fracture [78, 110, 111].

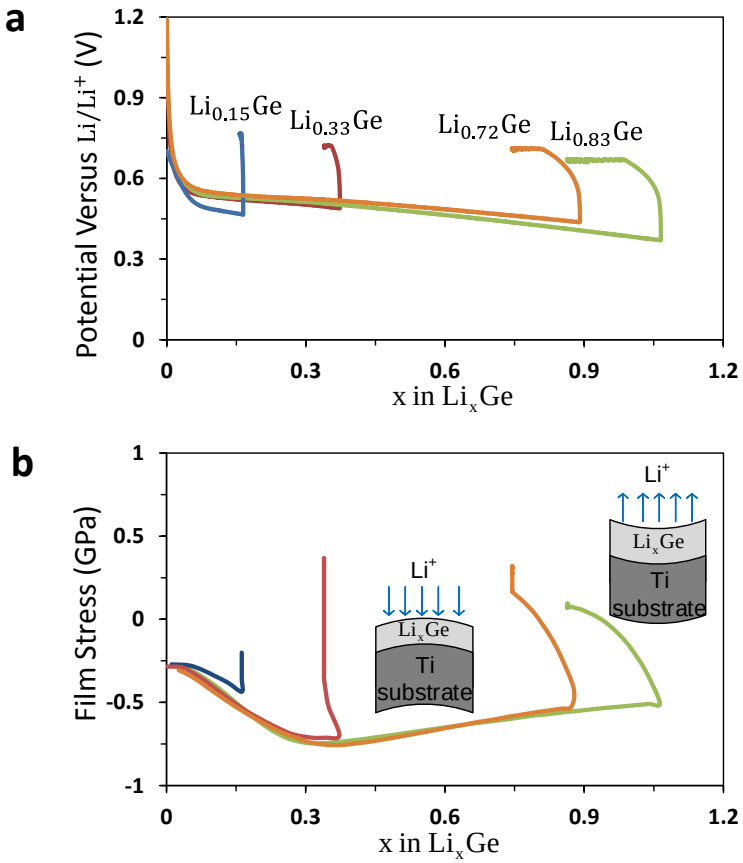

Figure 2.9 (a) Voltage profiles of four thin-film Ge electrodes lithiated/delithiated to various lithium concentrations. (b) Film stress evolution in the electrodes corresponding to the electrochemical testing in (a). The two insets in (b) illustrate the development of compressive and tensile stresses during lithium insertion into and extraction from the Ge electrodes, respectively.

Figure 2.9a shows the electrochemical profiles of four tested Ge film electrodes for fracture toughness measurement. The corresponding stress evolution in the Li_xGe films during the electrochemical testing are plotted in Fig. 2.9b. The SEI formation on the electrode surfaces during initial lithiation is reported to have a negligible effect on the film stress [92], so its effect is not considered here. All the stress curves start with an initial compressive film stress of 0.3 GPa resulting from the sputtering process. During lithiation of the Ge films, lithium ions are inserted into the films and cause volume expansion. However, the substrate constrains the Ge films from in-plane expansion, resulting in a dramatic increase in the compressive film stress. As the lithiation proceeds, the compressive film stress first increases linearly, revealing the elastic deformation of the films. After reaching a maximum compressive stress, the Li_xGe films lithiated beyond $x = 0.33$ show a slower rate of stress change due to plastic deformation. The large compressive stress present in the films, if left unmanaged, could retard crack growth during nanoindentation and therefore impede the fracture toughness evaluation. To circumvent this problem, the Ge electrodes were delithiated for a short period immediately following the lithiation process. During the delithiation process, the substrate constrains the contraction of the films, causing the compressive film stress to be relieved to promote crack formation during subsequent nanoindentation. To minimize possible lithiation-rate effects, we used the same lithiation rate for preparing the lithiated thin film electrodes. Because the focus of this work was primarily on the lithium-concentration-dependent fracture property, no additional effort was made to quantitatively examine the effects of lithiation rate on the stress generation. Furthermore, it was observed that the film stress kept evolving when the lithiation/delithiation process

was completed. Therefore, upon the completion of lithiation/delithiation of each electrode specimen, the stress evolution in the electrode was monitored until the stress value became stabilized. The vertical rising portion of each stress curve shown in Fig. 2.9b is due to this stress stabilization.

It is worth noting that recent lithiation experiments of silicon micropillars have shown that micro- and nano-crack formation during deep lithiation can expose new surface area and cause the formation of new SEI layers, leading to an overestimate of the lithium content in the electrode [112]. Unlike these micropillars in which large lithiation-induced hoop stress of a few GPa can promote crack formation, the thin film electrodes used in our experiments were under large compressive in-plane stress during lithiation. Following the lithiation process, the electrodes were slightly delithiated in order to alter their stress state to facilitate fracture toughness measurement. Such delithiation would induce tensile stress of 100-400 MPa, but it was not high enough to cause the formation of micro- and nano-cracks, as confirmed by post-mortem SEM observation.

After the electrochemical testing and film-stress measurement, the lithiated Ge electrodes were fracture tested by nanoindentation. The generated crack patterns under various levels of indentation loads can be divided into three categories: no cracking, radial cracking, and massive cracking. Figure 2.10 shows the two critical load curves separating the three crack-pattern regimes. The three inserts in the figure represent the SEM images of three indents made on a pristine Ge electrode at various levels of indentation loads. Under a small load of 4.13 mN, the indentation causes plastic deformation in both the film and substrate without introducing visible cracking (insert a). As the load increases to 8 mN, three radial cracks emerge from the sharp corners of the

indent (insert b). When the load is further increased to 19.6 mN, massive cracking around the indent is observed (insert c). The two critical load curves in Fig. 2.10 are seen to vary significantly with the Li content in the Ge electrodes. Furthermore, beyond a Li/Ge molar ratio of 0.83, no cracks are observed for indentation loads up to 93 mN, suggesting an extremely ductile deformation behavior at high lithium concentrations.

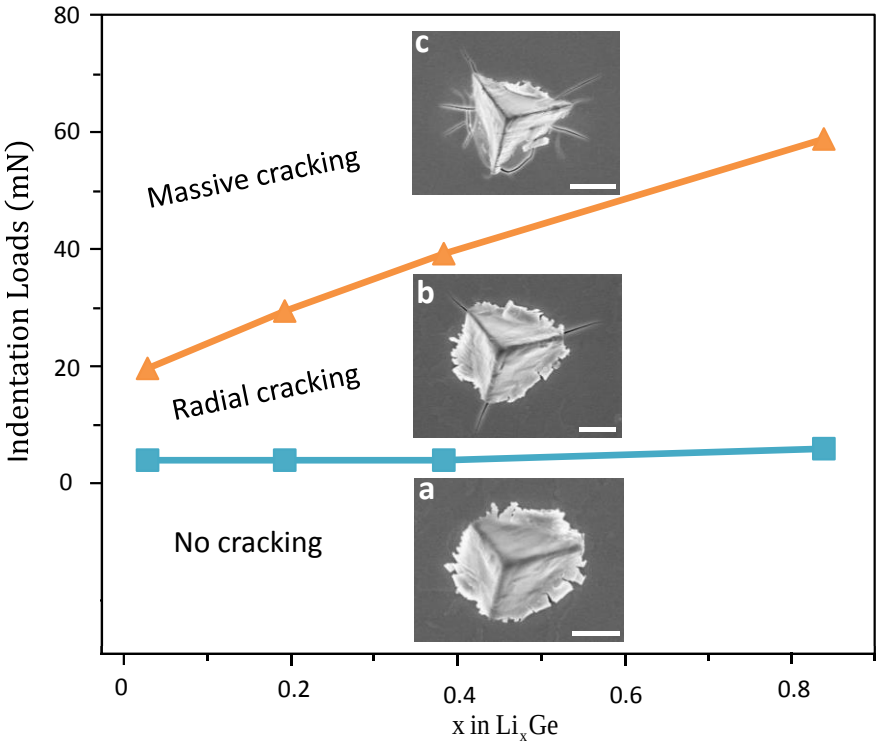

Figure 2.10 Indentation-induced crack patterns under different indentation loads for the lithiated Ge electrodes. The inserts show the SEM images of indents on a pristine Ge film electrode with (a) no cracking, (b) radial cracking, and (c) massive cracking. The scale bars are 1 μm in (a) and (b) and 2 μm in (c).

Figure 2.11 shows the measured fracture toughness of the Li_xGe thin films at various levels of lithiation. At each degree of lithiation, indents with radial cracks were chosen for the fracture toughness evaluation using the Morris Model. The fracture toughness of unlithiated Ge is measured to be 0.218 $MPa\sqrt{m}$, comparable in magnitude to that of typical brittle materials. As the degree of lithiation increases, the fracture

toughness of lithiated Ge increases steadily, reaching 0.81 $\mathrm{MPa}\sqrt{\mathrm{m}}$ for $Li_{0.72}Ge$. The fracture energy of lithiated Ge is calculated using the relationship $\Gamma = K_{IC}^2 / E$ and plotted in Fig. 2.11. The Young's modulus of lithiated Ge needed for the calculation is obtained by a linear rule of mixture $E = \left(xE_{Li} + E_{Ge}\right)/\left(1+x\right)$. Qi et al. has recently performed first principles density functional theory (DFT) calculations to investigate the dependency of the elastic properties on Li concentration for a large set of anode and cathode materials [113]. The authors found that, for alloy-forming electrode materials, such as Si, β-Sn and Al, the Young's moduli of lithiated compounds follow the linear rule of mixture. Although the elastic properties of Li_xGe were not specifically investigated in this work, it is reasonable to assume that the rule of mixture is applicable to lithiated Ge since it also has an alloying reaction mechanism. The obtained fracture energy curve of lithiated Ge in Fig. 2.11 is seen to increase monotonically with the increase of lithium concentration. The increasing trend in fracture resistance indicates that Li_xGe undergoes a sharp brittle-to-ductile transition as lithiation proceeds. This transition as well as the extremely high ductility of Li_xGe thin films at high lithium concentrations (beyond x = 0.83) suggests that $Li_{2.1}Ge$ possesses a much larger fracture resistance than $Li_{0.5}Ge$. Due to this high fracture resistance, $Li_{2.1}Ge$ is more resistant to fracture and can prevent cracking induced by tensile film stress at the initial delithiation of the Ge electrode, as shown in image b of Fig. 2.8. However, as delithiation proceeds, the fracture resistance of the Li_xGe thin films decreases, leading to crack formation at the end of delithiation during the first cycle (image c of Fig. 2.8). Therefore, a cutoff voltage below the threshold voltage for crack formation during delithiation can potentially prevent fracture of the electrode. Such findings provide significant guidelines for the design and operation of Ge-based LIBs.

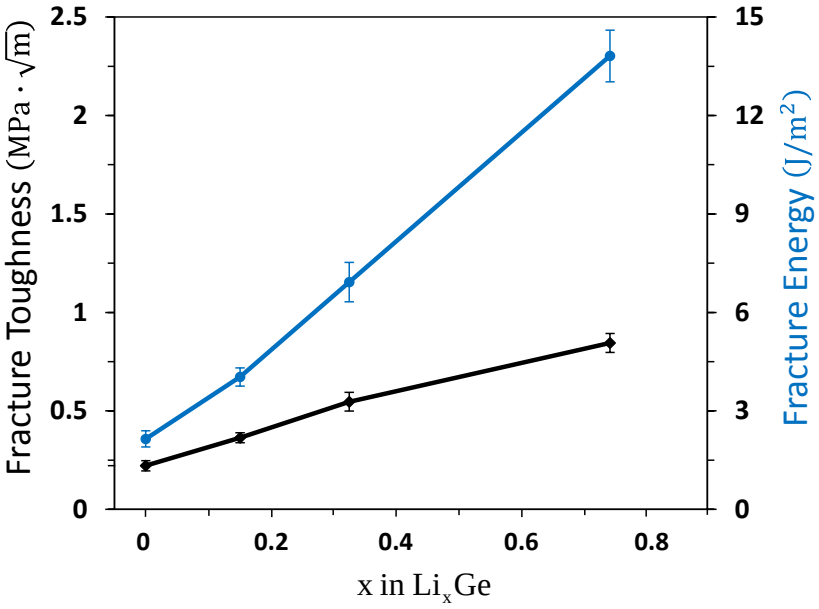

Figure 2.11 Fracture toughness and fracture energy of lithiated Ge electrodes as a function of lithium concentration.

Figure 2.12 shows a direct comparison between the fracture energy of lithiated Ge obtained in this work and the previously measured fracture energy of lithiated Si [109]. The fracture energy of pristine Si is 3 J/m^2, which is slightly higher than that of unlithiated Ge of 2.33 J/m^2. However, the fracture energy of lithiated Si decreases in the early stage of lithiation, which causes Si to crack more easily during charging and discharging if the concentration of Li is low. At higher levels of Li, the fracture energy of lithiated Si increases with the Li content, indicating that Si undergoes a brittle-to-ductile transition as lithiation proceeds. In our previous work, we also combined *in situ* TEM study and reactive-force field molecular dynamics (MD) simulations with nanoindentation testing to gain mechanistic insights into the fracture mechanisms of lithiated Si [109]. All of the three different techniques have consistently shown that

lithium-rich Si is more damage tolerant than lithium-lean Si. The interested reader is referred to there for more details.

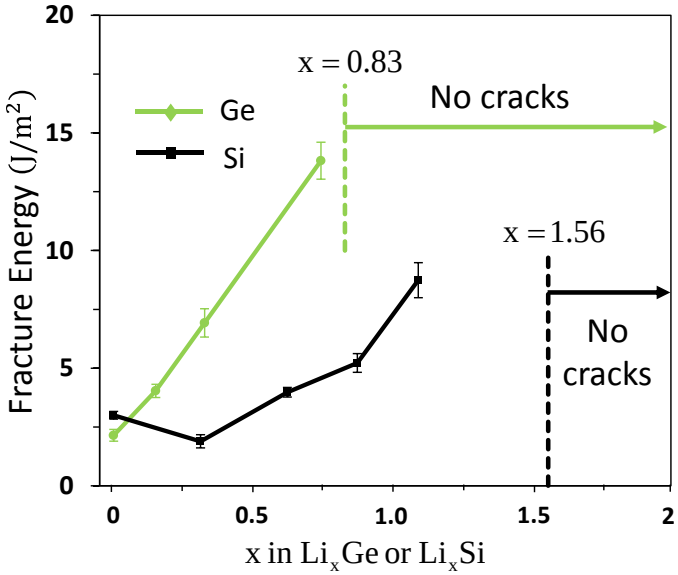

Figure 2.12 Comparison between the fracture energy of lithiated Ge electrodes and that of their Si counterparts as a function of lithium concentration. Beyond an *x* value of 0.83 for Li_xGe and 1.56 for Li_xSi, the lithiated products do not show signs of indentation cracking due to the substantial toughening effects of lithiation.

Ge, on the other-hand, does not exhibit the lithiation-induced embrittlement and shows a brittle-to-ductile transition through which the fracture energy and fracture toughness steadily increase as lithiation progresses. As shown in Fig. 2.12, after a small amount of lithiation (x = ~0.03), the fracture energy of Li_xGe exceeds that of Li_xSi. The fracture energy difference between the two lithiation products at a given degree of lithiation also increases as lithiation proceeds. This trend indicates that lithiated Ge is mechanically tougher than lithiated Si except at very low lithium concentrations. Furthermore, for both Li_xGe and Li_xSi, there is a critical lithium concentration, beyond which no electrode cracking is observed up to the maximum indentation load (93mN) of the nanoindentation setup. The critical values are approximately 1.56 for Si ($Li_{1.56}Si$) and

0.83 for Ge ($Li_{0.83}Ge$), which are also a clear indication of considerably higher fracture resistance of lithiated Ge. These quantitative results explain the robust behavior of Ge nanoparticles and pillars observed in previous works [86, 107]. Lithiated Ge is clearly seen to be intrinsically more resistant to crack initiation and propagation than lithiated Si. This attribute of Ge offers substantial potential for the development of durable, high-capacity, and high-rate anodes for advanced lithium-ion batteries.

In the works reported by Lee et al. [107, 108], the lithiation behaviors of Si and Ge micropillars were investigated and compared. When these micropillars are lithiated, a compressive hoop stress first develops at the surface and then turns into a tensile stress state which promotes the initiation of surface cracks. The unlithiated core, though inherently brittle, remains under a compressive stress state and therefore does not allow crack initiation. The authors showed that both the Si and Ge pillars display a size effect for mechanical fracture, with smaller pillars less prone to cracking. The tested Ge pillars have a critical diameter of ~1.2μm, below which no surface cracking occurs [107]. This critical value is much larger than the critical dimension of ~300 nm for fracture of Si pillars [108]. The authors have attributed this difference to the more isotropic expansion of Ge pillars which results in lower tensile stress concentrations at the surface [107]. The experimental results from our work suggest that the higher intrinsic fracture resistance of lithiated Ge may be another possible reason for their larger critical dimension for fracture.

Recent *in situ* TEM studies have revealed the formation of reversible nanopores in Ge after cyclic lithiation-delithiation [114]. The porous Ge network structure can facilitate the relaxation of mechanical stress during lithiation/delithiation cycling, and

therefore retard fracture and pulverization processes. However, the formation of nanopores is observed to occur only under deep delithiation states, as a result of the effective local aggregation of free volumes created during Li extraction. Since the Li_xGe electrodes used in our experiments were prepared via lithiation of Ge thin films followed by very slight delithiation, the formation of nanopores in these electrodes is very unlikely. We believe that the dominant toughening mechanism in Li_xGe is due to the increased fraction of ductile Li-Li and Li-Ge bonds, which can help overcome the brittleness of Ge-Ge bonds and suppress the formation and propagation of cracks. We will conduct MD simulations to further elucidate the atomistic mechanism underpinning the brittle-to-ductile transition in Li_xGe, and the results will be reported elsewhere.

2.2.4 Summary

The development of advanced Li-ion batteries has been hindered by a lack of full understanding of the fracture behaviors of high-performance electrode materials. In this study, we investigated the fracture toughness and fracture energy of lithiated Ge as a viable LIB anode material and found that they increased monotonically as lithiation proceeds, indicating a sharp brittle-to-ductile transition due to lithium insertion. We also compared the fracture energy of lithiated Ge with that of lithiated Si and showed that, despite a slightly lower fracture energy of Ge than that of Si in the unlithiated state, Ge possessed much higher fracture resistance than Si in the lithiated state. This superior characteristic of Ge makes it an outstanding anode material for durable, higher-performance Li-ion batteries. The experimental findings here provide an important input for the multiphysics modeling and design of Ge-based Li-ion batteries. The experimental

technique developed in this research also has general applicability to studies of other high-performance LIB anode and cathode materials.

CHAPTER 3 NANOSCALE DEFORMATION ANALYSIS IN ELECTRODE MATERIALS

3.1 Introduction

The technique of digital image correlation (DIC) is a powerful tool for conducting full-field, non-contact deformation measurement due to its high accuracy and ease of use [38-41]. Combined with various optical imaging methods, DIC has been used for a wide spectrum of applications across multiple length scales. Recently there is a growing need for quantitative deformation analysis at the nanoscale. Attempts have been made to combine DIC with other high-resolution microscopy techniques. For examples, by performing DIC analysis of the surface topographies obtained from atomic force microscopy (AFM) [115-124] and scanning tunneling microscopy (STM) [125-127], full-field deformation measurement techniques have been developed and applied for the mechanical property characterization at the micron and nanometer scales. More recently, DIC has been coupled with scanning electron microscopy (SEM) for quantitative deformation analysis [128-133]. It has been shown that compared to the optical DIC, the SEM-DIC approach is prone to drift and spatial distortions which need to be corrected with a non-parametric method to achieve high measurement accuracy. To further develop SEM-DIC, Kammers et al. proposed new drift distortion techniques accounting for stress relaxation [134] and used a novel speckle patterning method with self-assembled gold nanoparticles [135]. The SEM-DIC approach has shown potential in studying nanoscale thermal deformation [85], ductile fracture [136], and microstructure-property relationship [137, 138].

Compared to the scanning probe and scanning electron microscopies, the high-resolution transmission electron microscopy (HRTEM) offers a unique capability for characterizing internal material structures with sub-atomic spatial resolution [44, 45]. Despite the widespread use of TEM for material characterizations, much of the TEM work to date has been focused on direct imaging and crystallographic analysis. Notably, increasing efforts are devoted to applying TEM for quantitative deformation measurement. A full-field method based on the Fourier analysis of HRTEM images was developed by Hÿtch et al. [139, 140] to measure displacement and strain fields of a crystal lattice over a 25×25 nm area. The same group recently reported a new method, namely the dark-field electron holographic moiré technique [141], which offers larger fields of view without sacrificing measurement precision. Using electron diffraction under TEM, various studies have also been undertaken for the point by point measurement of localized strains in semiconductor materials with the strain measurement sensitivity of 10^{-4} and spatial resolution of <10 nm [142-146].

In this chapter, we present a study of full-field deformation analysis by combining DIC and HRTEM. Owing to the sub-angstrom spatial resolution of HRTEM and the sub-pixel displacement measurement sensitivity associated with DIC, the HRTEM-DIC analysis provides unprecedented nanoscale characterization capabilities that are not possible with optical and SEM-based DIC. To the best of our knowledge, this work represents the first systematic attempt to apply DIC to the quantitative full-field analysis of TEM images. In an effort to quantify the levels of DIC errors induced by the TEM image noise and electromagnetic-lens distortions, we performed experiments of rigid-body motion using amorphous silicon (*a*-Si) as a model material. The random

atomic structure inherent in *a*-Si allows image correlation to be performed without the need of dedicated speckle patterning. For other materials lacking such intrinsic random feature, speckle patterning techniques such as ion-implantation with a foreign species [147] may be employed. To further demonstrate its utility, we applied the HRTEM-DIC analysis to investigate a recently discovered mechanism of two-phase lithiation in *a*-Si [148]. The remainder of this chapter is organized as follows. In Section 3.2, we present the general theory behind two different DIC schemes − local and global DIC − which are used for TEM image correlation in this study. Section 3.3 provides the details of *a*-Si sample preparation and TEM experiments. The results of quantitative error assessment and deformation analysis in lithiated *a*-Si are presented and discussed in Section 3.4. Finally, the conclusions are drawn in Section 3.5.

3.2 Theory

In a two-dimensional DIC analysis, a full-field displacement distribution is obtained by correlating two digital gray-scale speckle images of a test specimen obtained before and after deformation [38, 149, 150]. The correlation is based on the assumption that the gray level is conserved at all pixel locations during deformation. Let f and g be the images in the reference and deformed configurations, respectively. The conservation law at a pixel location in the reference image, $\mathbf{X}$, can be given as

$$f(\mathbf{X}) = g(\mathbf{X} + \mathbf{U}(\mathbf{X})), \tag{3.1}$$

where $\mathbf{U}(\mathbf{X})$ is the displacement vector at $\mathbf{X}$.

In the original DIC approach, the displacement field is obtained by partitioning the region of interest (ROI) in the reference image into an array of uniformly spaced

subsets (usually square shaped) and tracking the movement of these subsets. The local deformation kinematics within a subset, *S*, is usually approximated in a linearized form as

$$\mathbf{U}(\mathbf{X}) \approx \mathbf{U}(\mathbf{X}_0) + \nabla\mathbf{U}(\mathbf{X}_0)\cdot(\mathbf{X}-\mathbf{X}_0), \tag{3.2}$$

in which $\mathbf{X}_0$ is the center of the subset, and $\mathbf{U}(\mathbf{X}_0)$ and $\nabla\mathbf{U}(\mathbf{X}_0)$ are the displacement and its gradient at $\mathbf{X}_0$, respectively. In Eq. (3.2), it is assumed that the deformation within the subset is close to be homogeneous so that the higher-order gradient terms can be neglected. Then, $\mathbf{U}(\mathbf{X}_0)$ is obtained by maximizing a cross-correlation function with respect to $\mathbf{U}(\mathbf{X}_0)$ and $\nabla\mathbf{U}(\mathbf{X}_0)$ according to

$$C = \frac{\int_S f(\mathbf{X})\cdot g(\mathbf{X}+\mathbf{U}(\mathbf{X}))d\mathbf{X}}{\left\{\int_S f(\mathbf{X})^2 d\mathbf{X}\cdot\int_S g(\mathbf{X}+\mathbf{U}(\mathbf{X}))^2 d\mathbf{X}\right\}^{1/2}}. \tag{3.3}$$

It is worth noting that some DIC algorithms employ higher-order gradient terms in Eq. (3.2) to improve the accuracy of correlation [151, 152]. In Eq. (3.3), the coordinates of the points in the deformed subset can be non-integer multiples of pixel. Therefore, the gray levels of these points need to be calculated through a pixel interpolation scheme. The most commonly used interpolation schemes in the literature include bilinear interpolation, bicubic interpolation, and bicubic spline interpolation [126, 150, 153]. By performing the above maximization independently for all subsets, a full-field displacement map of the test specimen can be constructed. Due to the use of the cross-correlation function in Eq. (3.3), the displacement measurement is highly immune to image noises and can achieve sub-pixel accuracy.

Recently, a new DIC method, which is conceptually different from the above subset-based local method, was developed based on a global description of the

deformation kinematics over the whole ROI [154, 155]. The global DIC method relies on minimizing the following sum-squared difference function:

$$\Phi = \int_{\mathrm{ROI}} [\, f(\mathbf{X}) - g(\mathbf{X} + \mathbf{U}(\mathbf{X}))]^2 \, d\mathbf{X} \,. \tag{3.4}$$

To formulate the minimization problem, the true displacement field is approximated by a trial displacement field with a finite number of degrees of freedom. A straightforward choice among many possible ones is to follow the finite element framework and express the trial displacement field as

$$\mathbf{U}_{\mathrm{Trial}}(\mathbf{X}) = \sum_{i=1}^{n} N_i(\mathbf{X}) \mathbf{U}_i \,, \tag{3.5}$$

in which $N_i(\mathbf{X})$ are the polynomial shape functions associated with a finite element mesh with n nodes, and $\mathbf{U}_i$ are the nodal displacements. This formulation turns the DIC problem into a nonlinear, multi-variable minimization of Φ with respect to $\mathbf{U}_i$, which can be well solved numerically using a Newton or gradient-descent iterative procedure. The final values of the nodal displacements are interpolated according to Eq. (3.5) to provide a full-field measure of the deformation within the ROI.

An alternative choice for the trial displacement field is to assume an analytical form as follows, based on *a priori* knowledge of the deformation field under analysis:

$$\mathbf{U}_{\mathrm{Trial}}(\mathbf{X}) = \mathbf{U}_{\mathrm{Ana}}(\mathbf{X}, \alpha_1, ..., \alpha_m) \,, \tag{3.6}$$

where $\alpha_i (i = 1, \, ..., m)$ are the unknown parameters that are used to describe the displacement field. These parameters can be determined by the same minimization process as above, with α_i in place of $\mathbf{U}_i$ as the minimization variables. This scheme was recently employed by Réthoré et al. [156, 157] to determine the stress intensity factors (SIFs) at a crack tip inside an elastic body. In their study, an analytical trial displacement

field is assumed around a crack tip using the Williams asymptotic expansion [158], with α_i being the mode I and II SIFs and other higher-order coefficients in the Williams expansion.

In several recent case studies [159, 160], global DIC and subset-based local DIC are thoroughly evaluated and compared to each other. It is shown that, when applied to analyze weakly-to-moderately inhomogeneous deformation, subset-based local DIC in general outperforms global DIC in terms of accuracy and computational efficiency. Nevertheless, local DIC is less suitable for analyzing highly heterogeneous deformation, since the local heterogeneous deformation within a subset cannot be well captured with the finite-order kinematics as assumed by local DIC. Such cases are better handled using global DIC which is able to capture more complex deformation modes. In the present work, we combine both types of DIC in the analysis of the deformation associated with two-phase lithiation in *a*-Si. We employ local DIC to measure smooth strain maps induced by lithium (Li) diffusion in the amorphous lithiated silicon (*a*-Li_xSi) region. Across the sharp phase boundary between the *a*-Si and *a*-Li_xSi regions, there is a large deformation gradient due to the reaction of *a*-Si with lithium. Accordingly, we turn to a global DIC scheme assuming an analytical trial displacement function, which will be introduced later, to obtain the reaction-induced strain at the phase boundary.

3.3 Experimental

3.3.1 Sample preparation

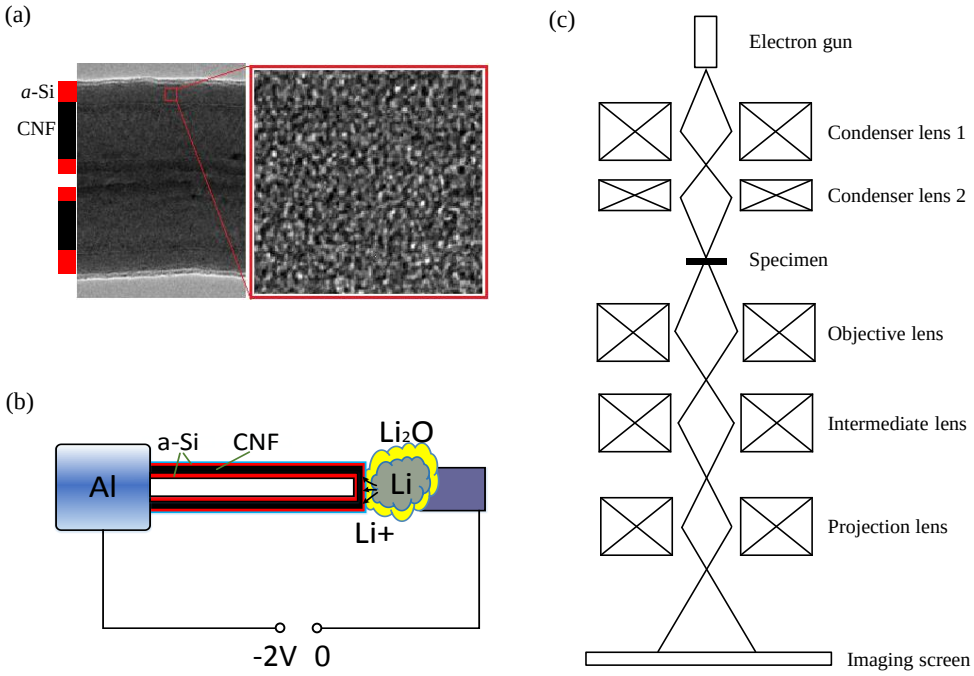

Figure 3.1 (a) A transmission electron microscopy (TEM) image showing the random atomic structure in amorphous silicon (*a*-Si), which serves as a high-quality speckle pattern for DIC analysis. (b) Schematic illustration of an *in situ* electrochemical lithiation experiment inside a TEM. (c) Schematic ray diagram of a TEM.

The *a*-Si samples used in this study were prepared by coating 20 nm thick *a*-Si layers onto both the inner and outer surfaces of hollow carbon nanofibers (CNFs) with the chemical vapor deposition (CVD) method. The amorphous atomic structure of *a*-Si, as shown in Fig. 3.1 (a), served as a random speckle pattern that was essential to image correlation. To prepare specimens for electrochemical lithiation experiments, a nano-sized battery was constructed in the half-cell configuration, which consisted of a working electrode, a counter electrode, and a solid electrolyte. As schematically shown in Fig. 3.1(b), an *a*-Si/CNF composite nanowire was glued to an aluminum rod with conductive

silver epoxy and used as the working electrode. On the surface of the *a*-Si layer, a 3 nm thick amorphous carbon (*a*-C) layer was coated to promote lithium ion and electron transport along the longitudinal direction. A lithium metal attached to a tungsten (W) probe was used as the counter electrode. A thin layer of LiO_2 (about 700 nm) on the lithium surface acted as the solid electrolyte.

3.3.2 TEM experiments

A high-resolution TEM (FEI Tecnai F30) was used for *in situ* imaging of the *a*-Si specimens that were subjected to rigid-body translation or electrochemical lithiation. To set the stage for the results that will be presented below, it is necessary to briefly review the working principle of a TEM. Fig. 3.1 (c) shows the schematic outline of a typical TEM, which largely resembles that of an optical transmission microscope. The electron beam from an electron emitter is illuminated onto a thin sample with a set of electromagnetic condenser lenses. The electron beam interacts with the sample and partially transmits through it. The transmitted beam, after passing a series of objective, intermediate and projection lenses, is projected onto a fluorescent screen to create a magnified image that represents the internal structure of the sample. Similar to optical light microscopy, TEM can operate in a variety of imaging modes including bright-field, dark-field and phase-contrast imaging. In this work, we used the phase-contrast imaging mode due to its ultra-high spatial resolution (~ 0.1 nm).

We performed two sets of experiments for TEM-DIC analysis. The first set of experiments was designed to assess the DIC errors related to different sources. In these experiments, an *a*-Si/CNF composite nanowire was supported on a copper grid which was mounted in a single-tilt TEM holder. An *a*-Si region in the nanowire was selected

and imaged, while the nanowire was held still or subjected to rigid-body movement using the TEM sample stage. In the second set of experiments, we applied the TEM-DIC technique to analyze the lithiation-induced deformation in *a*-Si. A nano-battery as described in Section 3.3.1 was assembled and mounted into a Nanofactory TEM-scanning tunneling microscopy (STM) holder in a helium-filled glovebox, where O_2 and H_2O concentrations were controlled below 0.1 ppm to avoid oxidation of the lithium. The holder was then transferred in a helium-filled plastic bag and inserted into the TEM column. During this process, the lithium metal was exposed to the air for about 5 seconds to form a Li_2O solid electrolyte layer. Inside the TEM, the Li_2O/Li terminal was driven by a piezo- positioner to engage the *a*-Si/CNF terminal. After the contact between the two terminals was established, the relative position of the tungsten probe with respect to the aluminum rod was held the same. A bias voltage of -2 V was applied to the *a*-Si/CNF electrode to drive the electrochemical lithiation process. During the lithiation, a sequence of high-resolution TEM images of the *a*-Si/CNF electrode was taken at an interval of 3 – 5 seconds. All TEM images taken in this study had the same pixel resolution of 0.077 nm. The *z*-height of the sample and the focusing condition for TEM imaging were kept unchanged during each experiment, in order to prevent their influences on the contrast of TEM images.

3.4 Results and discussion

3.4.1 Error assessment

Measurement errors can arise from several different sources in a TEM-DIC analysis. Digital images obtained from TEM experiments usually contain undesired pixel noise originating from the shot noise of the electron source, the electronic noise of the

detector [161], as well as the environmental noise [162]. Such pixel noise results in a degradation of the pixel intensity conservation law (Eq. (3.1)) and therefore can cause appreciable errors in the image correlation. Another common type of errors is due to the geometric distortion of the TEM imaging system. Unlike the distortion of optical lenses, which is relatively easy to correct using parametric distortion models, the electromagnetic-lens distortion of a TEM poses a greater challenge to model and compensate. In this study, we employed several testing procedures to quantitatively assess the levels of noise and distortion-induced errors. However, the correction of such errors is beyond the scope of the present work and will be left for future consideration.

We first quantified the noise-induced errors by correlating two TEM images of the same *a*-Si region in a nanowire. The two images were acquired 1 second apart while keeping the sample stationary. The DIC analysis was conducted using subset-based commercial software (VIC-2D, Correlated Solution, Inc., W. Columbia, SC). A subset size of 59×59 pixels and a step size of 10 pixels were chosen for the analysis. The subset size was made much larger than the speckle size to reduce the effects of image noise, since TEM images usually have a higher noise level than typically seen in optical images. Also, to avoid the edge effects, the boundary points at a distance of less than half the subset size from the ROI boundary are excluded for all the local DIC analysis reported in this paper. The obtained displacement and strain maps are presented in Fig. 3.2. Although no external displacement was applied to the sample, the horizontal (u_x) and vertical (u_y) displacement components in Figs. 3.2(a) and (b) show small but non-negligible values with means of -0.05 and 0.12 nm, respectively. This displacement was caused by the creeping movement of the sample stage and/or the thermal drift of the TEM components.

As a result of the random Gaussian noise inherent in the TEM images, the two displacement maps show fluctuations of 0.002 nm (0.026 pixel) as measured by their respective standard deviations (SDs). The fluctuations in displacement lead to non-zero strain distributions (ε_{xx} and ε_{yy}) with SDs of 0.02% - 0.03% as shown in Figs. 3.2 (c) and (d). The statistical characteristics of the noise-induced displacement and strain maps are summarized in Table 3.1, together with those of other maps that will be discussed below.

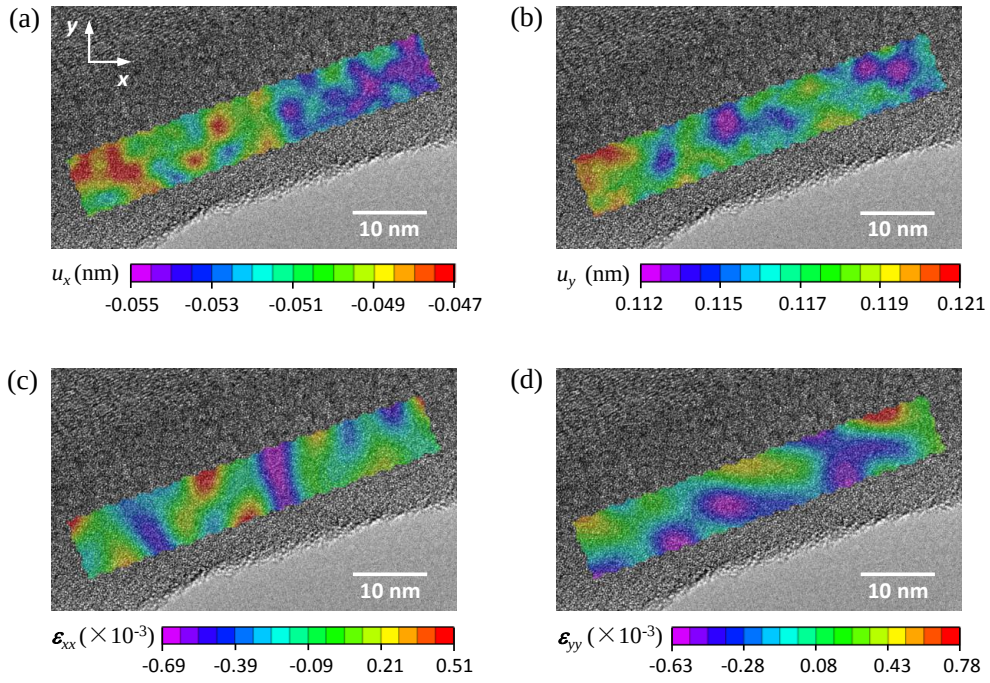

Figure 3.2 Assessment of the DIC errors due to the TEM image noise. Maps of (a, b) displacements and (c, d) DIC strain errors resulting from the TEM image noise.

The errors induced by the electromagnetic-lens distortion were assessed through rigid-body sample translation and image shift. We first subjected an *a*-Si sample to a rigid-body translation and measured the associated displacement. The sample translation was achieved by moving the motorized sample stage for a nominal horizontal displacement of about 3 nm. Figs. 3.3(a) and (b) show the measured distributions of u_x

and u_y. The u_y component is found to have a small deviation from its zero nominal value due to the crosstalk of the sample stage. In similar rigid-body translation experiments conducted at much larger length scales, the DIC error is usually calculated as the bias of the measured displacement from the true one. However, in this TEM experiment, the true displacement imposed on the sample is in the nanometer range and is therefore difficult to determine precisely. To resolve this issue, we consider a combination of several statistical parameters, including the absolute mean strain components ($|\varepsilon_{xx}^{\mathrm{m}}|$ and $|\varepsilon_{yy}^{\mathrm{m}}|$) and the standard deviations of displacement and strain (σ_{u_x}, σ_{u_y}, $\sigma_{\varepsilon_{xx}}$ and $\sigma_{\varepsilon_{yy}}$), as the measure of error (MOE). All of these parameters should be zero in the error-free case and increase with an increasing level of DIC errors. Table 3.1 shows the MOE parameters calculated from Fig. 3.3. These parameters show a two- to three-fold increase compared to those solely resulting from the image noise, thereby quantitatively indicating the presence of electromagnetic-lens distortion. Note that the DIC strain error maps in Figs. 3.3(a)-(d) are highly irregular in appearance, suggesting that a parametric model may not be practical for lens-distortion correction.

Table 3.1 Statistical characteristics of the displacement and strain maps shown in Figs. 3.2 – 3.4

	u_x (nm)		u_y (nm)		ε_{xx} ($\times 10^{-3}$)		ε_{yy} ($\times 10^{-3}$)	
	Mean	SD	Mean	SD	Mean	SD	Mean	SD
Figure 3.2	-0.051	0.002	0.116	0.002	-0.102	0.248	-0.046	0.311
Figure 3.3	2.633	0.007	-1.785	0.006	-0.514	0.742	0.076	0.761
Figure 3.4	3.515	0.007	-0.958	0.005	-0.400	0.676	0.037	0.642

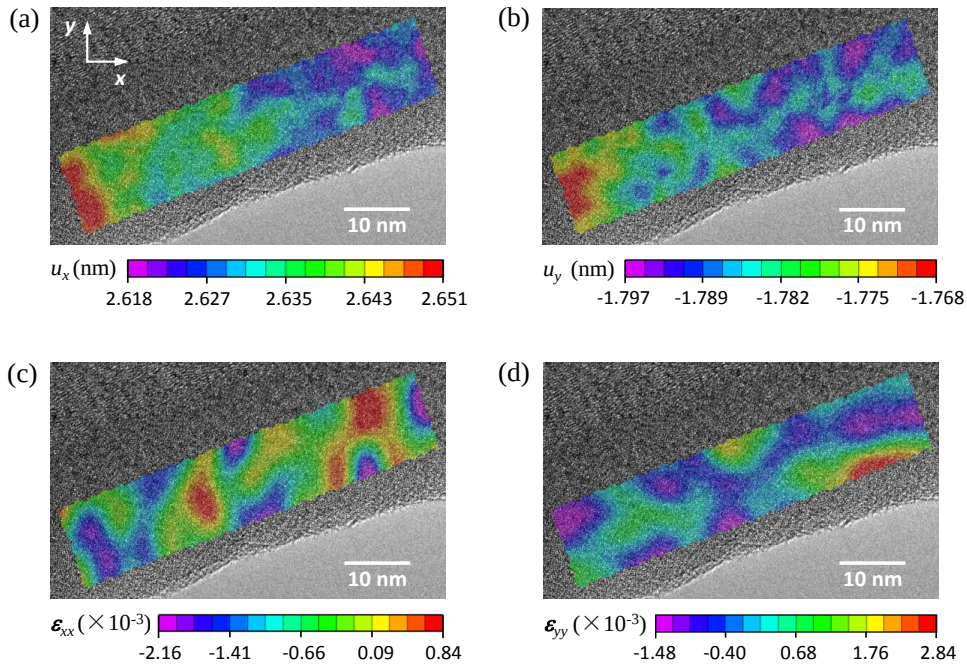

Figure 3.3 Assessment of the DIC errors due to the electromagnetic-lens distortion. Maps of (a, b) displacements and (c, d) DIC strain errors resulting from a rigid-body translation of the *a*-Si sample.

TEM imaging at high magnifications is susceptible to sample drift which can cause the area of interest (AOI) in a sample to move out of the field of view. Modern TEMs offer an "image shift" function to compensate such drift by steering the electron beam to *a targeted AOI* with a set of electromagnetic deflection coils. The image shift procedure may lead to additional electromagnetic-lens distortion and therefore introduce measurement error for image correlation. We assessed this type of error by holding an *a*-Si sample still and applying an image shift of 3.5 nm in the horizontal direction. Fig. 3.4 shows the maps of apparent displacement and strain associated with this shift. The variations in these maps are much greater than those in Fig. 3.2 resulting from the image noise only. Comparing the MOE parameters presented in Table 3.1, the strain errors induced by the image shift and rigid-body sample translation are found to be at similar

levels of ~ 0.1%. In order to obtain physically meaningful deformation fields using local DIC, one has to make sure that the strain under analysis is sufficiently larger than this error level.

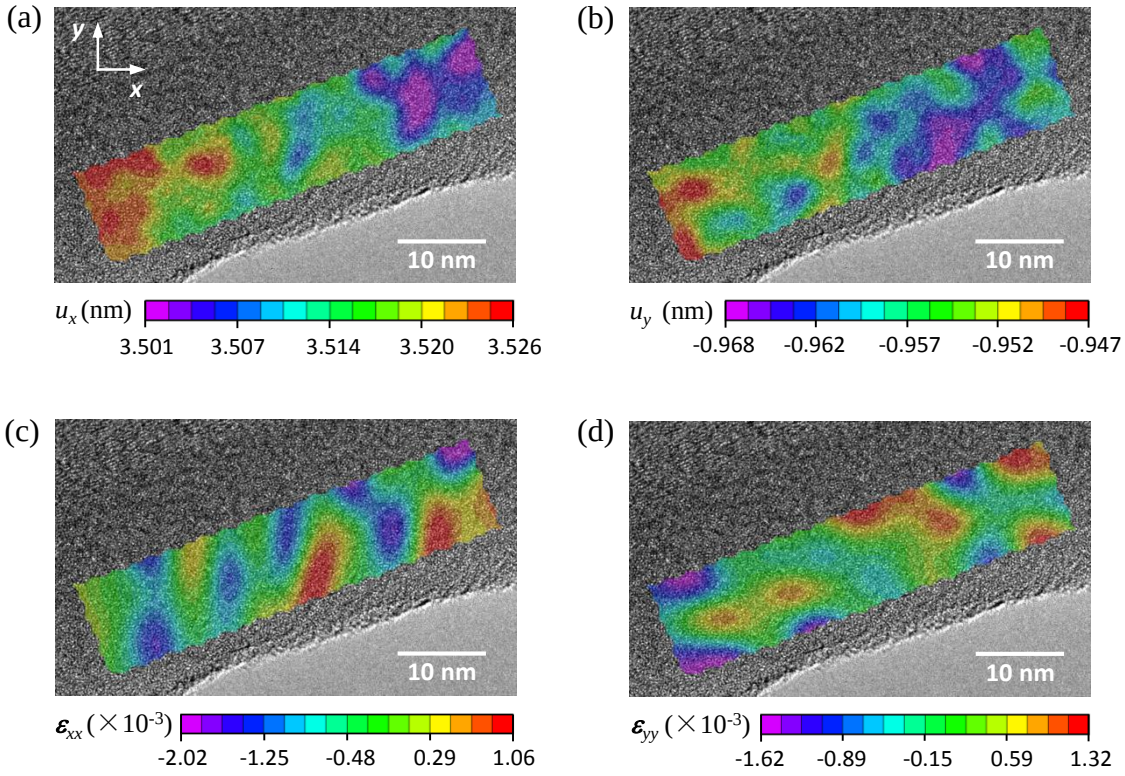

Figure 3.4 Assessment of the DIC errors due to the image shift operation. Maps of (a, b) displacements and (c, d) DIC strain errors resulting from a rigid-body shift of the imaging window.

3.4.2 Nanoscale deformation analysis in lithiated amorphous silicon

To demonstrate its utility, we applied TEM-DIC to quantitatively analyze a two-phase lithiation process in *a*-Si. In the development of next-generation rechargeable lithium-ion batteries (LIBs), a current challenge is to understand the mechanical characteristics of high-capacity electrode materials. Using *in situ* TEM, we recently investigated the lithiation-induced deformation in *a*-Si as a high-capacity LIB anode material. We revealed a striking two-phase lithiation process in *a*-Si [148], which is

contrary to the widely held view that the lithiation in *a*-Si is a single-phase process with gradual and smooth lithium profiles.

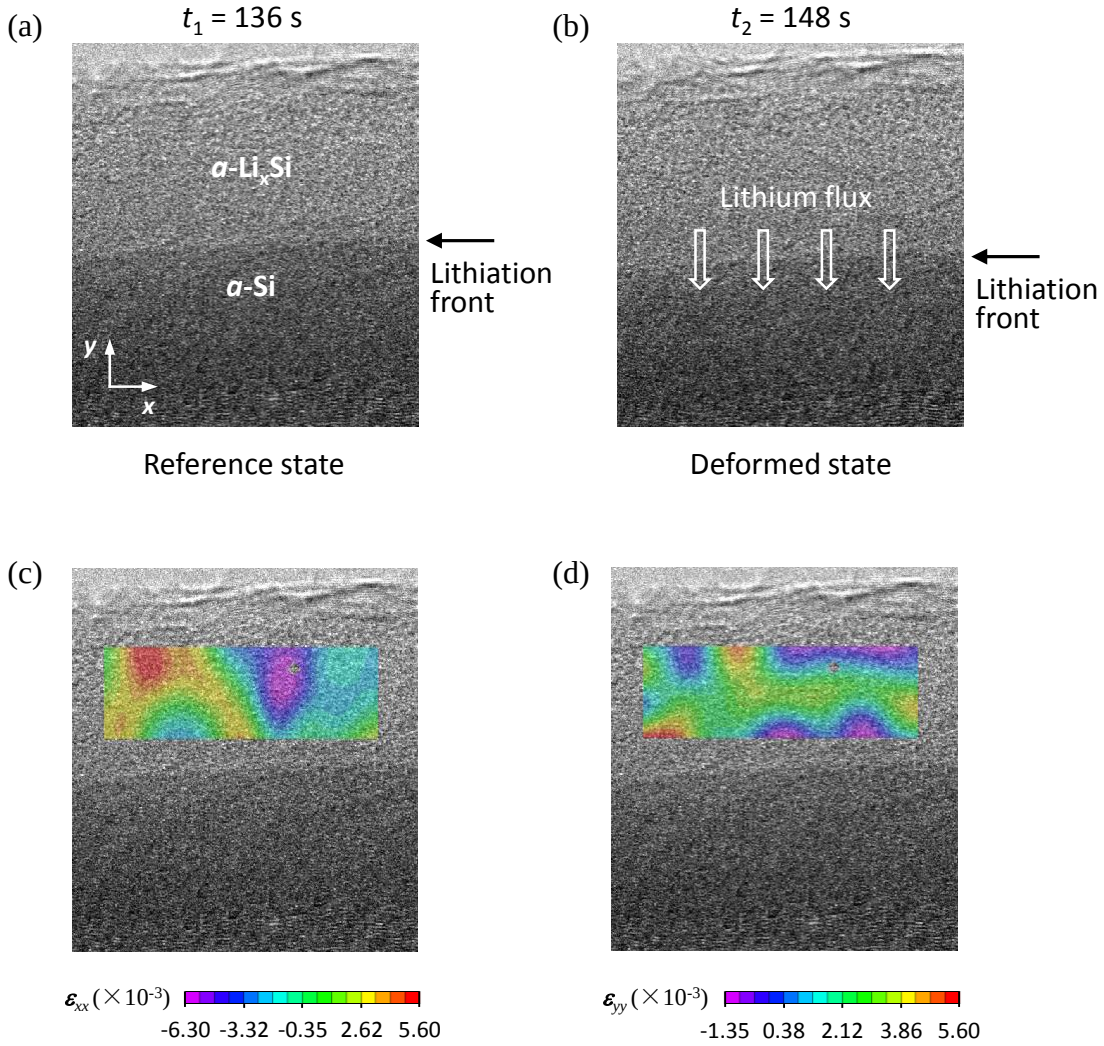

Figure 3.5 Local DIC analysis of the lithium-diffusion-induced strain in a lithiated Si region. (a, b) Reference and deformed TEM images used for the DIC analysis. (c, d) Obtained and strain contour plots superimposed on the reference TEM image as shown in (a).

Figs. 3.5 (a) and (b) show two high-resolution TEM images taken at different time instants during an electrochemical lithiation experiment. The lithium flux was supplied from the top surface. The lithiation is seen to proceed by the movement of a sharp phase

boundary between the *a*-Si reactant and an amorphous *a*-Li_xSi product. The growth kinetics of *a*-Li_xSi is controlled by two concurrent processes: (1) the *reaction* of Li with Si to form an initial product of Li_xSi at the phase boundary, and (2) the *diffusion* of the Li ions in the product phase region. We employed the local DIC method to analyze the diffusion-induced strain in the *a*-Li_xSi region behind the phase boundary. The image at t_1 = 136 s (Fig. 3.5(a)) was chosen as the reference configuration and the image at t_2 = 148 s (Fig. 3.5(b)) as the deformed configuration. Figs. 3.5(c) and (d) present the distributions of the two normal strain components obtained from DIC analysis. The two strain maps show fluctuations with statistical means and standard deviations of $\varepsilon_{xx} = (-0.06 \pm 2.93) \times 10^{-3}$ and $\varepsilon_{yy} = (1.82 \pm 1.49) \times 10^{-3}$. The levels of both strain components are comparable to the strain errors induced by the image noise and lens distortion, indicating the two strain maps should be interpreted as DIC errors rather than true deformation. This result also suggests that the diffusion-induced strain is negligibly small (relative to the measurement capability), and therefore nearly all of the lithiation-induced deformation occurs at the sharp reaction front. It is noteworthy to mention that, to enable DIC analysis, the shape of the speckle pattern should not change significantly during the deformation. In our work, the random atomic structure of Si in the *a*-Li_xSi region is not expected to undergo substantial change, due to the very small mobility of Si compared to that of Li. On the other hand, the atomic-scale distribution of Li ions may change, but it is not resolvable by our HRTEM due to the very small diameter of Li ions and therefore does not affect the DIC analysis.

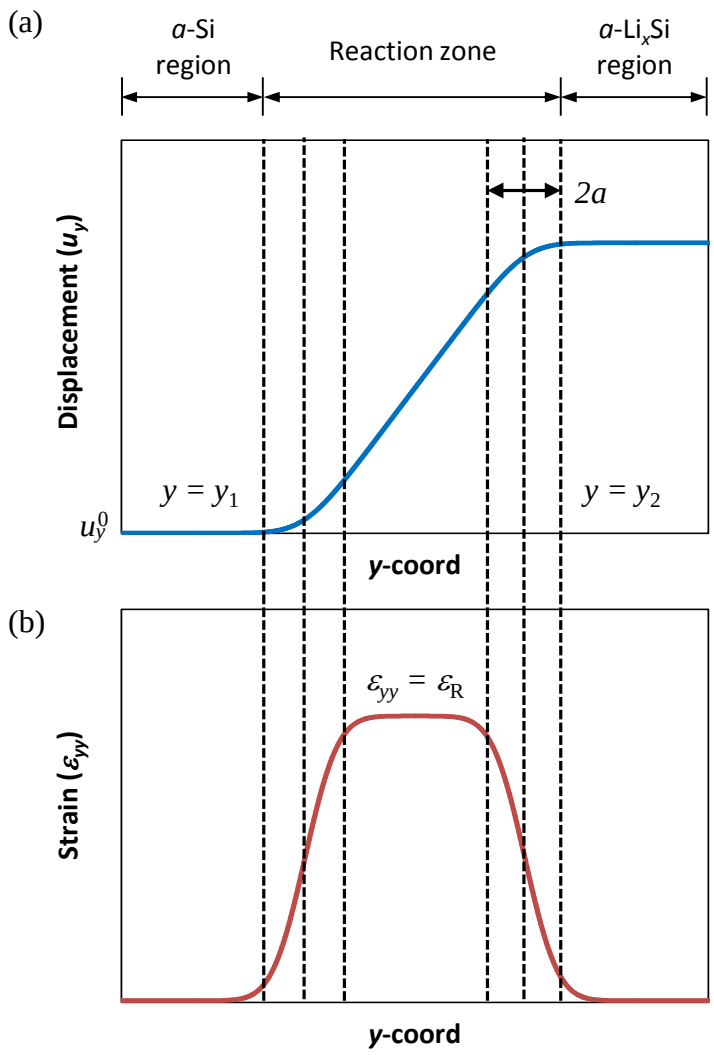

Figure 3.6 Plots of the trial (a) displacement and (b) strain functions use for the Global DIC analysis of the reaction-induced strain at an *a*-Si/*a*-Li$_x$Si phase boundary.

Across the lithiation front, the reaction of Li with Si causes a change in the Li:Si molar ratio from zero to a finite value. The deformation induced by the reaction exhibits a large strain gradient at the sharp reaction front, which is unresolvable by the local DIC method. The use of local DIC in this case would result in under-estimation of the deformation gradient. To obtain the reaction-induced strain, we adopted the global DIC approach using an analytical trial deformation field as follows:

$$\varepsilon_{xx} = \varepsilon_{xy} = 0, \tag{3.7a}$$

$$\varepsilon_{yy}(y) = \frac{\varepsilon_{\mathrm{R}}}{2}\left[\mathrm{erf}\left(\frac{y-y_1}{a}\right) - \mathrm{erf}\left(\frac{y-y_2}{a}\right)\right], \tag{3.7b}$$

where ε_{R} is the reaction-induced strain, y_1 and y_2 are the starting and ending positions of the reaction zone defined in the reference configuration, a is the half width of the strain gradient zone, and the $\mathrm{erf}(\cdot)$ function is the Gauss error function. In choosing the above trial deformation field, we have two considerations that arise from the local DIC result. First, there is no appreciable deformation in the *x*-direction due to the lateral constraint of the unreacted a-Si region, such that the DIC problem can be treated as one-dimensional. Second, the diffusion-induced strain in the *a*-$\mathrm{Li}_x\mathrm{Si}$ region is negligibly small, leading to a nearly rigid-body movement of the *a*-$\mathrm{Li}_x\mathrm{Si}$ region. By integrating Eq. (3.7), the trial displacement field is obtained as

$$u_x = u_x^0, \tag{3.8a}$$

$$u_y(y) = \frac{\varepsilon_{\mathrm{R}}}{2}\left\{(y-y_1)\mathrm{erf}\left(\frac{y-y_1}{a}\right) - (y-y_2)\mathrm{erf}\left(\frac{y-y_2}{a}\right)\right.$$

$$\left. + \frac{a}{\sqrt{\pi}}\left[e^{-\frac{(y-y_1)^2}{a^2}} - e^{-\frac{(y-y_2)^2}{a^2}}\right] + (y_2 - y_1)\right\} + u_y^0, \tag{3.8b}$$

in which u_x^0 and u_y^0 are the rigid-body displacement components of the unreacted *a*-Si region. Figs. 3.6(a) and (b) show schematically the trial displacement and strain profiles as a function of the *y*-coordinate.

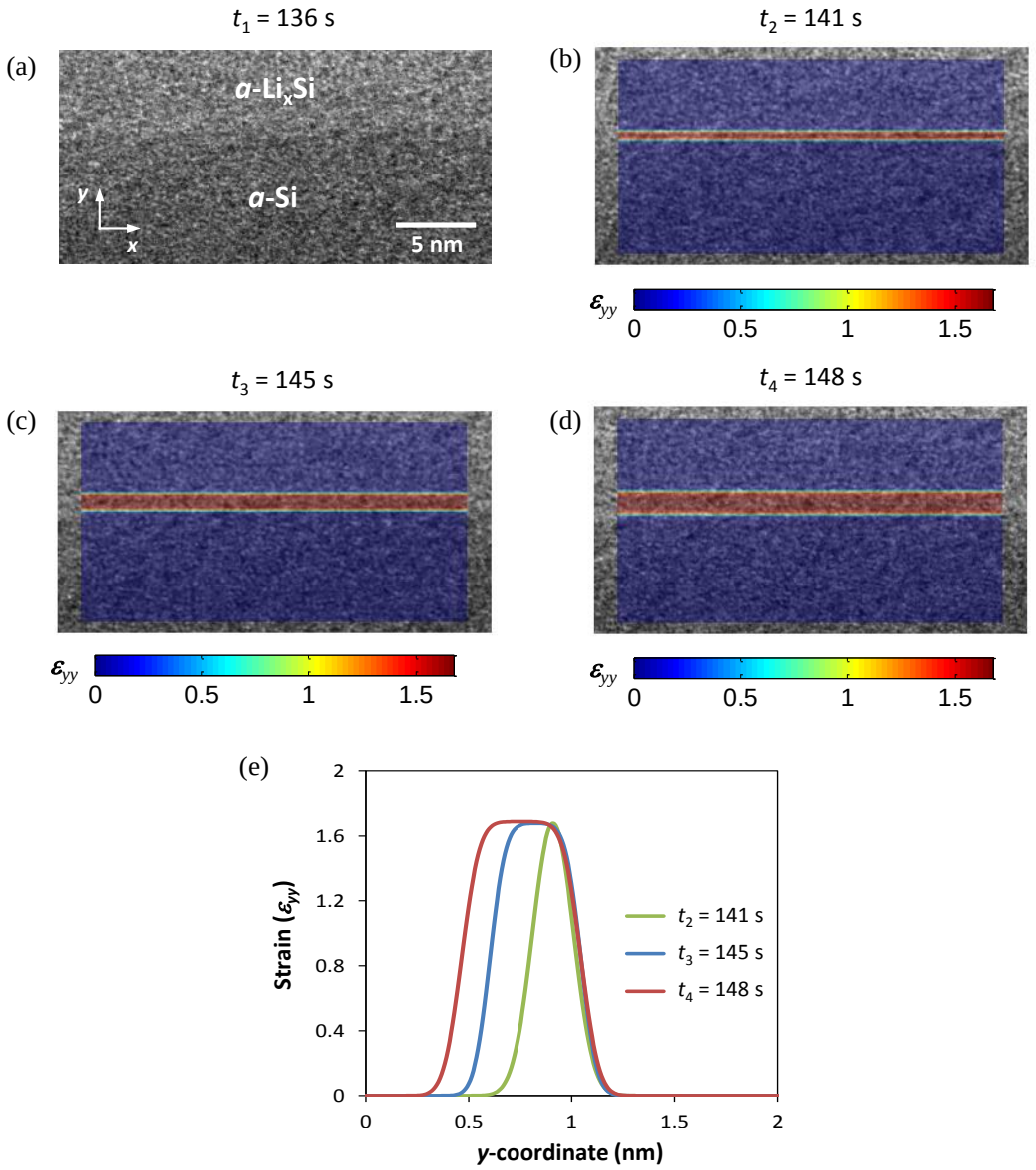

Figure 3.7 Global DIC analysis of the reaction-induced strain at an a-Si/a-LixSi phase boundary. (a) The first image in a sequence of TEM images serving as the reference image for the global DIC analysis. (b-d) Obtained strain contour plots superimposed on the subsequent TEM images at various stages of lithiation. (e) Obtained strain profiles across the *a*-Si/*a*-LixSi phase boundary. Note that the strain analysis is made with respect to the reference image in (a). The width of the reaction zone with large strain increases as the lithiation proceeds.

A global DIC analysis was performed on the same reference (Fig. 3.7(a)) and deformed (Fig. 3.7(d)) images used for the previous local DIC analysis. Additionally, we

sought to obtain an evolution of the reaction-induced strain by correlating two intermediate frames (Figs. 3.7(b) and (c)) at time instants t_2 = 141 s and t_3 = 145 s to the reference frame. At each time instant, the error functional defined in Eq. (3.4) was minimized with respect to the parameter set (ε_R , y_1 , y_2 , a , u_x^0 , u_y^0) of the trial displacement function. The minimization was carried out over a rectangular region of 12×24 nm around the *a*-Si/*a*-Li_xSi boundary using a simplex search method of Lagarias et al. [163]. The distributions of reaction-induced strain resulting from the minimization process are presented in Figs. 3.7(b)-(d), and Fig. 3.7(e) shows the strain profiles across the *a*-Si/*a*-Li_xSi phase boundary. The lithiation front is seen to move steadily towards the *a*-Si region at a speed of 0.05 nm/s. Inside the reaction zone, the reaction-induced strain reaches a maximum value of ε_R =168%, which remains fairly constant as the lithiation proceeds. Invoking a linear relationship between the volumetric strain and lithium concentration [164-166], $\varepsilon = 0.72x$, we obtain a molar Li:Si ratio of x = 2.33 in the reaction zone. Also note from Fig. 3.7(e) that the width of the strain gradient zones (i.e., the zones over which the strain increases from 0 to 168%) is 0.32 nm, which is comparable to the average Si-Si bond length of 0.23 – 0.25 nm in *a*-Si [167-169]; this suggests that the *a*-Si/*a*-Li_xSi phase boundary is atomistically sharp. Finally, we note that the lithiation process in *a*-Si revealed by the *in situ* TEM experiments [148] is a two-step process. In this work, we focused on the first lithiation step in which *a*-Si is transformed into *a*-$Li_{2.33}$Si through a two-phase lithiation mechanism. In the second step of lithiation, the phase of *a*-$Li_{2.33}$Si is further transformed into the fully lithiated phase of *a*-$Li_{3.75}$Si. This step of lithiation proceeded very fast, such that we could not acquire high-quality

TEM images for DIC analysis. Future investigation with a better control of the second-step lithiation is required to elucidate the lithiation mechanism in this step [148].

3.5 Summary

We have shown that it is feasible to combine high-resolution TEM and DIC for performing full-field deformation analysis at the nanoscale. The theories behind two different DIC methods − local and global DIC − were introduced, and their advantages and disadvantages were discussed. A quantitative error assessment was made by correlating TEM images captured during the rigid-body movement of an *a*-Si specimen. It was shown that the strain errors resulting from the TEM image noise and electromagnetic-lens distortion were on the order of 0.1%. The utility of TEM-DIC was demonstrated through a case study of two-phase lithiation in *a*-Si. Local and global DIC were applied to analyze the diffusion-induced strain in the lithiated Si region and the reaction-induced strain at the lithiation front, respectively. The DIC analysis revealed that the lithiation in *a*-Si occurred by the movement of an atomistically sharp phase boundary between the *a*-Si reactant and an amorphous *a*-Li_xSi (x = 2.33) product. Broadly, the TEM-DIC technique presented in this work enables the analysis of full-field deformation at considerably smaller length scales than other microscope-based DIC methods, and thus provides a new avenue for nanoscale material characterization.

CHAPTER 4 COMPUTATIONAL MODELING OF FRACTURE IN ION-INSERTION MATERIALS

4.1 Introduction

The quantitative fracture and deformation analysis in Chapters 2 and 3 are incorporated into a continuum model in this chapter to study the effective fracture properties of ion-storage materials and fracture behaviors of lithiated nanoparticles. Solid-state ionic transport and diffusion under both electrochemical and mechanical driving forces occurs in many material systems, such as fuel cells and rechargeable batteries for energy conversion and storage. In these material systems, ion transport and diffusion often induce large volumetric change, which, if not accommodated appropriately, generates substantial stress. The stress can cause the fracture and ultimate failure of these material systems. For the rational design of energy storage and conversion systems using these ion-storage materials, the effects of both electrochemical and mechanical driving forces on fracture must be thoroughly understood.

In this chapter, we develop a composition-dependent computational cohesive zone model and integrate it with a chemo-mechanical continuum model [79]. The computational framework is then applied to investigate the effective fracture properties of ion-storage materials and the fracture behaviors of lithiated nanostructures. The quantitative results obtained in this work can provide significant guidance for the design, operation, and mechanical testing of ion-storage material systems.

4.2 Theoretical framework

4.2.1 Deformation and diffusion in ion-storage materials

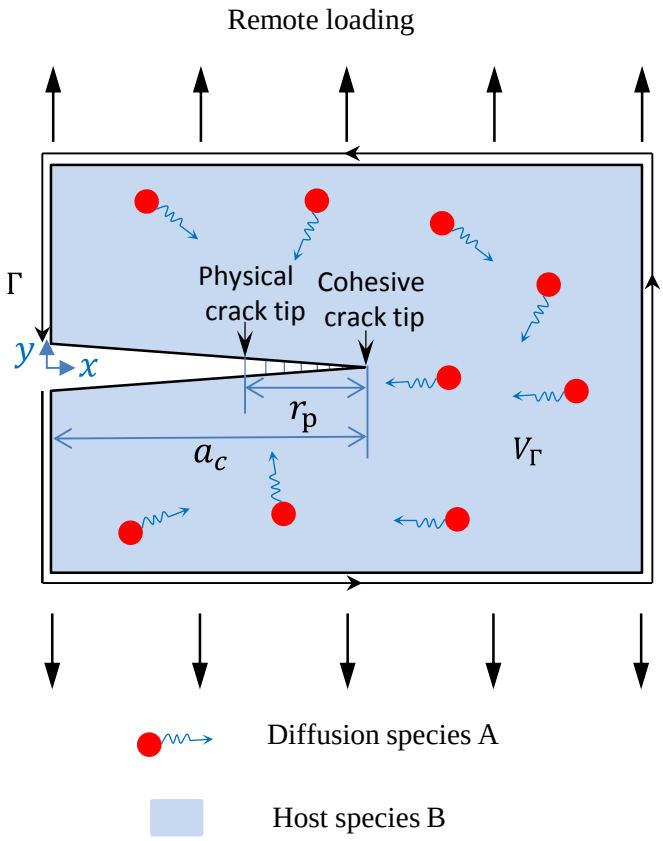

Figure 4.1 Schematic of a cohesive crack growing within an ion-storage solid.

Without loss of generality, we consider a solid $A_\xi B$ that consists of guest species A and host species B. The molar concentration of A in $A_\xi B$, i.e., the solvability of A in B, is assumed to vary from $\xi = 0$ to $\xi = \xi_{max}$. The diffusivity of the host atoms is considered to be infinitesimal compared with the guest ones, which allows the definition of continuum deformation [46]. When subjected to mechanical or electrochemical loadings, such as the transport and diffusion of species A, the solid may change its shape.

For convenience, we employ the reference (Lagrangian) and deformed (Eulerian)

configurations to describe the deformation and motion of the solid. We use **X** and **x** to represent the coordinates in the reference and deformed descriptions, respectively. In what follows, we assume that all field quantities are functions of **X**, unless stated explicitly otherwise.

Based on the above definition, the displacement of a material point can be defined as

$$\mathbf{u} = \mathbf{x} - \mathbf{X}. \tag{4.1}$$

The change in the shape of a representative material element within the solid can then be characterized by the corresponding deformation gradient tensor

$$F_{ij} = \frac{\partial x_i}{\partial X_j} = \delta_{ij} + \frac{\partial u_i}{\partial X_j}, \tag{4.2}$$

where δ_{ij} is the Kronecker delta. The Lagrangian finite strain tensor is defined in terms of the deformation gradient tensor

$$E_{ij} = \frac{1}{2}\left(F_{ki}F_{kj} - \delta_{ij}\right). \tag{4.3}$$

In the solid $\mathrm{A}_{\xi}\mathrm{B}$, the total deformation of a representative material element is attributed to three processes: an irreversible plastic deformation F_{lj}^{p}, followed by a volume change F_{kl}^{c} due to the expansion of the host material during guest species insertion, and a reversible elastic deformation F_{ik}^{e},

$$F_{ij} = F_{ik}^{\mathrm{e}}F_{kl}^{\mathrm{c}}F_{lj}^{\mathrm{p}}. \tag{4.4}$$

Combining equations (4.3) & (4.4), the total Lagrange strain can be written as

$$E_{ij} = F_{jl}^{\mathrm{p}}F_{lk}^{\mathrm{c}}E_{ij}^{\mathrm{e}}F_{kl}^{\mathrm{c}}F_{lj}^{\mathrm{p}} + F_{jl}^{\mathrm{p}}E_{ij}^{\mathrm{c}}F_{lj}^{\mathrm{p}} + E_{ij}^{p}, \tag{4.5}$$

where E_{ij}^{e} , E_{ij}^{c} and E_{ij}^{p} are defined following equation (4.3) and refer to the elastic, compositional strain, and plastic strain, respectively.

The deformation of the velocity gradient follows as

$$L_{ij} = \frac{\partial \dot{x}_i}{\partial x_j} = \dot{F}_{iK} F_{Kj}^{-1} = L_{ij}^{e} + L_{ij}^{c} + L_{ij}^{p} \ , \tag{4.6}$$

where $L_{ij}^{e} = \dot{F}_{ik}^{e} F_{kj}^{e^{-1}}$, $L_{ij}^{c} = F_{in}^{e} \dot{F}_{nl}^{c} F_{lk}^{c^{-1}} F_{kj}^{e^{-1}}$, and $L_{ij}^{p} = F_{in}^{e} F_{nm}^{c} \dot{F}_{mr}^{p} F_{rl}^{p^{-1}} F_{lk}^{c^{-1}} F_{kj}^{e^{-1}}$. These three terms can be interpreted as the velocity gradients due to elastic stretching, the insertion of guest species, and plastic flow, respectively.

For simplicity, the deformation gradient due to the insertion of guest species is assumed to be isotropic and take the form

$$F_{ij}^{c} = \left[\beta(\xi)\right]^{1/3} \delta_{ij} , \tag{4.7}$$

Where $\beta(\xi)$ measures the volume changes of solid $\mathrm{A}_{\xi}\mathrm{B}$ when a concentration of guest species ξ is inserted into the solid network with the following relationship

$$\beta(\xi) = 1 + \Omega\xi , \tag{4.8}$$

where Ω is a dimensionless parameter that relates the guest species concentration and the volume change of the ionic solid.

Constitutive equations that correlate the elastic and plastic parts of the deformation gradients to stress fields within solid $\mathrm{A}_{\xi}\mathrm{B}$ are adopted here. The elastic strain E_{ij}^{e} is considered to be small (represented by ε_{ij}^{e}), and is related to the Cauchy stress as follows

$$\sigma_{ij} = F_{ik}^{\mathrm{e}} (3K\varepsilon_{m}^{\mathrm{e}} \delta_{kl} + 2S\left(\varepsilon_{kl}^{\mathrm{e}}\right)^{\mathrm{dev}}) F_{jl}^{\mathrm{e}} , \tag{4.9}$$

where $\varepsilon_{\mathrm{m}}^{\mathrm{e}} \equiv \varepsilon_{kk}/3$ and $\left(\varepsilon_{ij}^{\mathrm{e}}\right)^{\mathrm{dev}} = \varepsilon_{ij}^{\mathrm{e}} - \varepsilon_{m}^{\mathrm{e}}\delta_{ij}$ are the hydrostatic and deviatoric parts of the elastic strain respectively; K and S are the bulk and shear modulus, respectively.

The plastic deformation of the solid $\mathrm{A}_{\xi}\mathrm{B}$ is assumed to follow the associated flow rule with composition-dependent yield surface $\sigma_{\mathrm{Y}} = \sigma_{\mathrm{Y}}(\xi)$ in the form of

$$Q = Q(\sigma) = \frac{1}{2}\sigma^{\mathrm{dev}} : \sigma^{\mathrm{dev}} - \frac{1}{3}\sigma_{\mathrm{Y}}^{2} = 0. \tag{4.10}$$

The corresponding plastic strain rate is related to the stress by an isotropic viscoplastic constitutive law

$$L_{ij}^{\mathrm{p}} = \frac{3}{2}\frac{\sigma_{ij}^{\mathrm{dev}}}{\sigma_{\mathrm{Y}}}\frac{dE^{\mathrm{p}}}{dt}, \tag{4.11}$$

where $\sigma_{ij}^{\mathrm{dev}} = \sigma_{ij} - \sigma_{kk}/3$ is the deviatoric stress.

Governing equations for the mechanical deformation of the solid are completed by the equilibrium equation of momentum

$$\frac{\partial \sigma_{ij}}{\partial x_{j}} = 0, \tag{4.12}$$

and the boundary conditions $\sigma_{ij}n_{j} = 0$ on stress-free surfaces. We assume quasi-static condition and negligible body force for all the simulations conducted in this work.

The conservation of mass for the solid requires that

$$\frac{\partial C^{\mathrm{A}}}{\partial t} + \frac{\partial J_{i}}{\partial X_{i}} = 0, \tag{4.13}$$

where C^{A} is the stoichiometric concentration of guest species A, i.e. the atom number per unit volume, in the reference configuration, which is related to molar concentration ξ through $\xi = C^{\mathrm{A}}/C^{\mathrm{B}}$. J_{i} is the flux of guest species A crossing unit reference area and is

computed based on Fick's law

$$J_i = -\frac{D}{k_B T} C^A \frac{\partial \mu}{\partial X_i}, \tag{4.14}$$

where D is the diffusion coefficient of guest species A in $A_\xi B$, k_B is the Boltzmann constant, T is the temperature which is taken to be a constant in this work ($T = 300\,\mathrm{K}$), and μ is the electrochemical potential of guest species which can be expressed as

$$\mu = \mu_{chem} - \tilde{\Omega}\sigma_h . \tag{4.15}$$

Here, $\mu_{chem} = \mu_0 + k_B T \ln \frac{\xi}{\xi_{max} - \xi}$ is the potential of the solid due to chemical reactions, $\tilde{\Omega}$ is a parameter relating the mechanical response of the solid to its electrochemical potential, and $\sigma_h = \sigma_{kk}/3$ is the hydrostatic stress. The term $\tilde{\Omega}\sigma_h$ is responsible for the coupling between stress and diffusion.

Eqs. (4.1)-(4.15) describe the two-way coupling between the chemical and mechanical fields in ion-storage materials. The concentration change of the guest species within host materials induces deformation through (4.7)-(4.8). The resulted deformation causes mechanical stresses, which, in return, affect ion diffusion through the stress-dependent electrochemical potential (4.15).

4.2.2 Cohesive zone model and path-independent J-integral

To simulate crack nucleation and propagation in ion-storage materials, we employed the computational cohesive zone approach. A chemical-composition-dependent bilinear traction-separation law, one of the most commonly used cohesive zone laws, was adopted to describe the cohesive zone behavior of a crack propagating in an ion-storage material, as illustrated in Fig. 4.2. σ_m quantifies the strength of the interface where the

crack propagates along, σ_m/δ_m controls the reversible elastic stiffness, δ_c and σ_m determine the fracture energy through $G_c = (\sigma_m \delta_c)/2$, which is characterized as a function of guest species concentration from our previous works [170, 171], and k_c is a large contact stiffness that resists inter-penetration of crack surfaces under compressive loading. σ_m and δ_c were calculated as a function of guest species concentrations from the following equations [172],

$$\sigma_m = 2\sqrt{\frac{SG_c}{\pi(1-\nu)L}}, \tag{4.16}$$

$$\text{and } \delta_c = \sqrt{\frac{\pi(1-\nu)LG_c}{S}}, \tag{4.17}$$

where ν is the Poisson's ratio, and L is the finite element size.

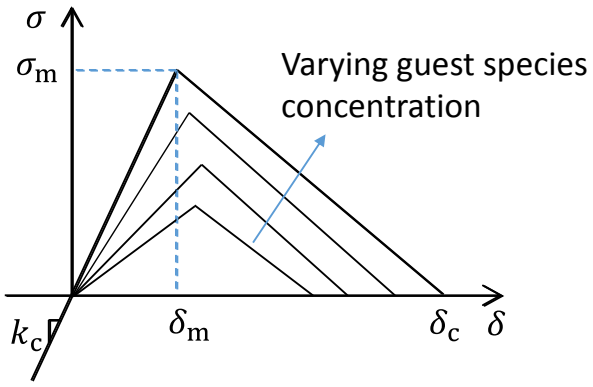

Figure 4.2 Traction-separation relations for a chemical-composition-dependent bilinear cohesive zone law considered in this study. The cohesive strength and characteristic cohesive opening are characterized as a function of guest species concentration.

This cohesive zone model was integrated with the chemo-mechanical constitutive model described above and implemented through the user element subroutine (UEL) in

ABAQUS 6.13. Based on the numerical results from finite element analysis, we implemented a path-independent J-integral method to evaluate the energy release rate, which is discussed below.

The classical J-integral of [173] is defined over a closed contour Γ^*,

$$J_{\Gamma^*} = \oint_{\Gamma^*} \left(w^{\mathrm{e}} n_1 - t_i \frac{\partial u_i}{\partial x_1} \right) ds \,, \tag{4.18}$$

where w_e is the elastic energy density, t_i is the traction vector on the contour Γ^*, n_i is the unit outward normal on Γ^*, u_i is the displacement vector, and ds is the length element along the contour. Using the Cauchy equation $t_i = n_j \sigma_{ji}$ along the integration path and the divergence theorem in (4.18), one obtains

$$J_{\Gamma^*} = \int_{A^*} \left(\frac{\partial w^{\mathrm{e}}}{\partial x_1} - \frac{\partial}{\partial x_j} \left(\sigma_{ji} \frac{\partial u_i}{\partial x_1} \right) \right) dA \,. \tag{4.19}$$

The J-integral represents a balance between the total energy inside the closed contour and the energy passing through the contour line. In the presence of solid state diffusion, the total energy inside the closed contour is highly associated with ion diffusion and redistribution. Therefore, considering the elastic energy w^{e} alone will no longer satisfy the balance between the total energy inside the closed contour and the energy passing through the contour line [174].

In this work, we consider the crack tip as a thermodynamic system, which can exchange mass, energy and entropy with the surrounding continuum body. A path-independent area J-integral for coupled mechano-diffusional driving forces [79] was employed

$$J = J(\Gamma) = \int_{\Gamma} \left[\left(w^{\mathrm{e}} + w^{\mathrm{p}} \right) \delta_{ij} - \sigma_{ji}^{\mathrm{PK1}} \frac{\partial u_i}{\partial X_1} \right] N_j d\Gamma_0 - \int_{V_\Gamma} \mu^{\mathrm{A}} \frac{\partial C^{\mathrm{A}}}{\partial X_1} dA_0 , \qquad (4.20)$$

Where Γ is an arbitrary contour, and V_Γ is the crack tip domain bounded by Γ, as shown in Fig. 4.1. $w^{\mathrm{e}} = \frac{\sigma_{\mathrm{m}}^2}{2K} + \frac{\sigma_{ij}^{\mathrm{dev}} \sigma_{ij}^{\mathrm{dev}}}{4G}$ is the elastic strain energy, $w^{\mathrm{p}} = \int_0^t [\beta(\xi)]^{2/3} \sigma_{jk}^{\mathrm{PK2}} \dot{E}_{jk}^{\mathrm{p}} \mathrm{d}t$ is the plastic potential, and $\sigma_{ij}^{\mathrm{PK1}} = \det(\mathbf{F}) F_{ik}^{-1} \sigma_{kj}$ and $\sigma_{ij}^{\mathrm{PK2}} = \det(\mathbf{F}) F_{ik}^{-1} \sigma_{kl} F_{jl}^{-1}$ are the first and second Piola-Kirchhoff stresses, respectively.

Equation (4.20) was implemented on the numerical results from finite element analysis to evaluate energy release rates. The energy domain integral method originally proposed by Shih et al. [175] was adopted in this study.

The computational framework developed in this section are applied to study the effective fracture properties of ion-storage materials and fracture mechanism maps of lithiated nanostructures in this work, as we discuss as follows.

4.3 Results and discussion

4.3.1 Effective fracture properties of ion-storage materials

We first applied the computational framework in section 4.2 to investigate the effective fracture properties of ion-storage materials. We used a double cantilever beam (DCB) configuration, as schematically illustrated in Fig. 4.1 (a). A two-dimensional (2D) solid medium containing a cohesive crack is subjected to a remote far-field load. For simplicity, we only consider crack propagation perpendicular to the far-field loading, i.e., mode I fracture, and assume a plane strain condition in this work. The medium has an initial crack length of $a_0 = 300\,\mathrm{nm}$, a width of $\mathrm{L} = 3.3a_0$ and a height of $\mathrm{H} = a_0$. In order

to examine the fracture properties of the material under combined electrochemical and mechanical driving forces, we prescribe an initial homogeneous distribution of guest species A within host material B with a concentration of ξ_0 ($A_{\xi_0}B$) through stress-free expansion. The concentration of ξ_0 in $A_{\xi_0}B$ corresponds to an intrinsic fracture energy of $G_c^0 = G_c(\xi_0)$. Around the crack tip, a nonlinear fracture process zone of length r_p exists, whose constitutive behavior is governed by the cohesive traction-separation law described earlier.

Due to the geometrical and loading symmetry about the crack plane, only the upper half of the beam is modeled. In fracture tests of materials, instability caused by simultaneous drop of load and displacement, which is referred as snap-back instability, is often observed. In this work, we employed displacement-controlled boundary conditions in our finite element analysis and introduced slight artificial viscous energy dissipation in some of the simulations as a remedy. Each finite element simulation starts with subjecting the DCB with a constant displacement-controlled loading speed. As the displacement keeps increasing over time, a cohesive crack initiates and propagates steadily in the ion-storage medium. Path-independent area J-integral introduced in Section 4.2 was performed on the loaded specimen in the far field to evaluate the energy release rate. By measuring the corresponding crack-tip positions at different stages of loading, we constructed complete energy release rate curves.

For simplicity, we assume the Young's modulus and Poisson ratio are independent of guest species concentration and only consider the case of linear elastic fracture. Under such assumptions, we carried out systematic parametric studies to investigate the effects of two parameters, crack growth velocity *v* and the gradient of

intrinsic fracture energy with guest species concentration $dG_c/d\xi$, on the effective fracture properties of $A_\xi B$. Two characteristic parameters, crack growth velocity $v_c = ED/G_c^0$ and length $l_c = G_c^0/E$, were identified and used for non-dimensional representation. Furthermore, for convenience, we used a dimensionless parameter $\chi = \frac{1}{G_c^0}\frac{dG_c}{d\xi}$ to denote the normalized gradient of fracture energy with guest species concentration.

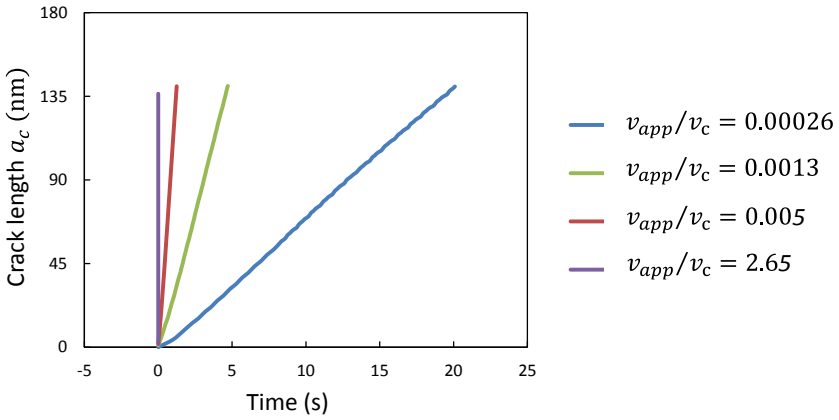

Figure 4.3 Crack extension curves under different loading velocities.

Figure 4.3 shows a plot of crack extension versus time for a wide range of loading velocities under $\chi = \frac{1}{G_c^0}\frac{dG_c}{d\xi} = 3.33$. It is seen that in all cases, crack grows steadily, and the crack length increases linearly with time. Based on such a linear relationship, we obtained a constant crack growth velocity v for each v_{app}/v_c, which will be used and discussed later.

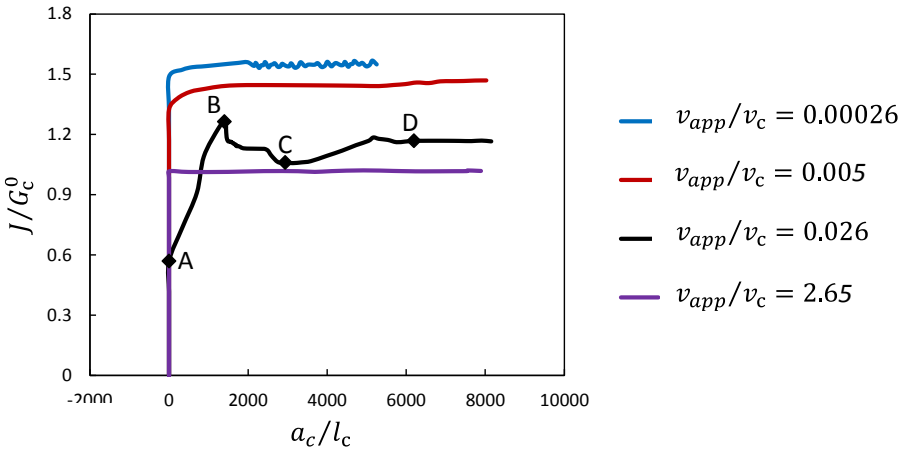

Figure 4.4 Normalized crack growth resistance curves (R-curves) under different loading velocities.

The energy release rates for a wide range of v_{app}/v_c values were obtained by performing J-integral on the cracked $A_\xi B$ medium and plotted as a function of crack length a_c in Fig. 4.4. We can see that for loading velocities $v_{app}/v_c = 0.00026$, 0.005, and 2.65, J is found to increase abruptly with little crack extension and reach a plateau (maximum) value as the crack extends in each condition. In the following, the plateau value of J in these curves will be interpreted as the effective fracture energy G_c^{eff}. It is interesting to observe that unlike the three former cases, the J curve for $v_{app}/v_c = 0.026$ fluctuates considerably as the crack first starts to grow, and eventually converges to a constant value. In this case, the plateau value beyond the fluctuation regime is taken as G_c^{eff}. The mechanism underlying this fluctuation stage will be discussed later. It is also worth noting that we obtained the crack growth velocities (from 0.0000026 to 265) and J-integrals for three additional χ values (0.66, -0.66, and -

3.33), and found that only the J curve with an applied velocity of $v_{app}/v_c = 0.026$ and fracture energy gradient of $\chi = 3.33$ behaves in a different way.

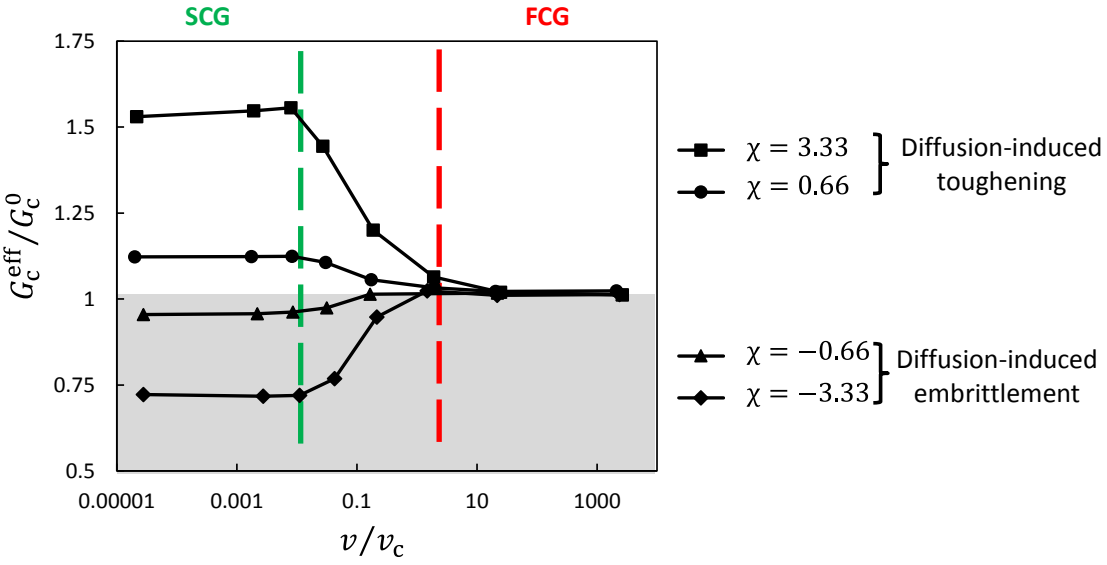

Figure 4.5 Normalized effective fracture energy as a function of crack growth velocities for four different χ values.

In Fig. 4.5 we show a plot of effective fracture energy G_c^{eff} with the crack growth velocity as the independent variable and the gradient of intrinsic fracture energy as the curve parameter. It is observed that both parameters have a dramatic influence on G_c^{eff}. For a constant χ value, 3.33, for example, G_c^{eff} is found to maintain a relatively constant value under small v values ($v/v_c < 0.01$). However, as v increases, G_c^{eff} starts to decrease considerably and eventually converges to an asymptotic value G_c^0 for sufficiently large v values ($v/v_c > \sim 2$). Based on such an observation, we divide the G_c^{eff} curve into three distinct regimes: slow crack growth (SCG) regime, fast crack growth (FCG) regime, and a transition regime between them. It is also seen that the G_c^{eff} curves for the other

three χ ($\chi = 0.66$, -0.66, and -3.33) values are characterized by these three regimes as well. Furthermore, all the four G_c^{eff} curves converge to an essentially identical asymptotic value G_c^0 in the limit of $v >> v_c$.

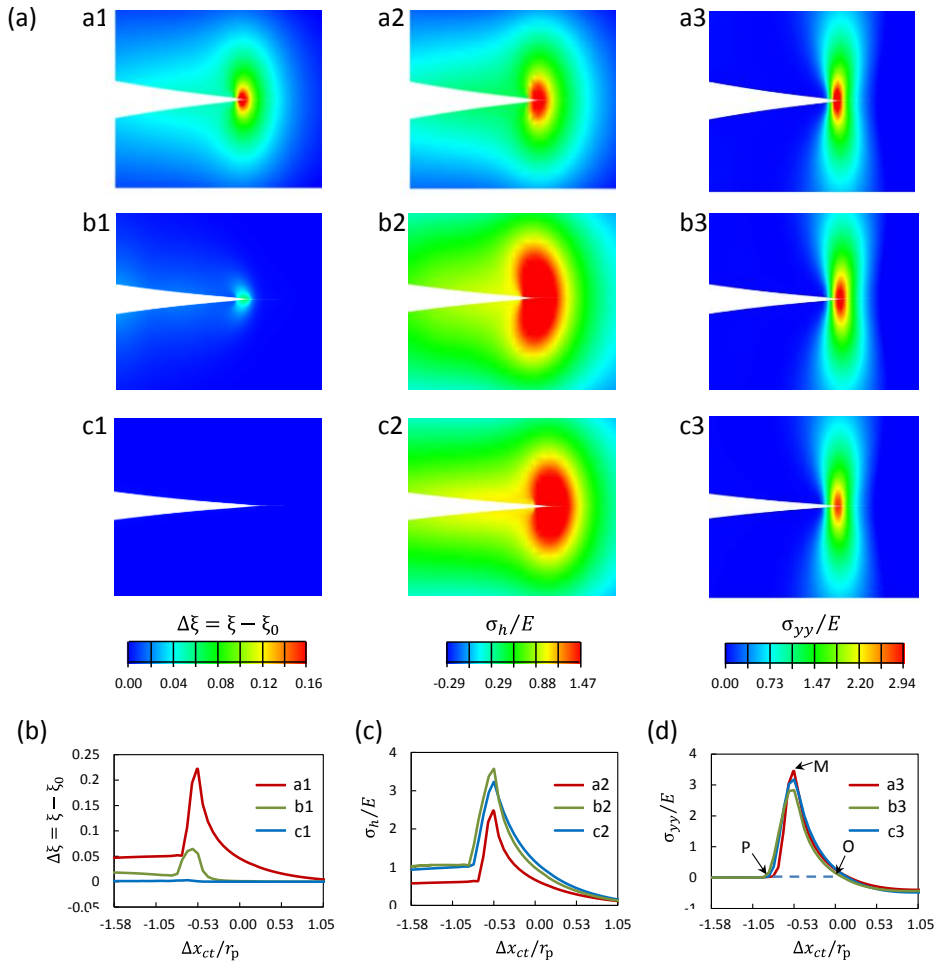

Figure 4.6 (a) Contour plots of the guest species concentration change $\Delta\xi = \xi - \xi_0$ (a1-c1), hydrostatic stress σ_h (a2-c2) and in-plane stress component σ_{yy} (a3-c3) under three distinct loading conditions (a-c) labelled in Fig. 4.5. (b)-(d) Line plots of $\Delta\xi$, σ_h and σ_{yy} along the crack line corresponding to the contour plots in (a).

To elucidate the mechanism underlying the G_c^{eff} curves, we first examined the case for $\chi = \dfrac{1}{G_c^0}\dfrac{dG_c}{d\xi} = 3.33$ by identifying three distinct crack growth velocities, which

are denoted by **a** ($v/v_c = 0.0019$), **b** ($v/v_c = 0.19$), and **c** ($v/v_c = 24.72$) on the G_c^{eff} curve in Fig. 4.5 and represent the SCG, transition, and FCG regimes, respectively. For each crack velocity, we show in Fig. 4.6 the contour plots for three outputs, i.e., guest species concentration change $\Delta\xi = \xi - \xi_0$ (a1, b1, and c1), hydrostatic stress σ_{h} (a2, b2, and c2), and in-plane stress component σ_{yy} (a3, b3, and c3). To further quantify these three parameters around the crack tip, their line plots are presented as a function of the axial distance from the cohesive crack tip, $\Delta x_{\mathrm{ct}} = x - x_{\mathrm{CrackTip}}$, along the crack propagating direction (Figs. 4.6(b-d)), where x_{CrackTip} is the crack tip position. Δx_{ct} is normalized by cohesive zone size r_{p}, which was evaluated from the σ_{yy} line plot based on the adopted bilinear cohesive zone law in Fig. 4.2. The evaluation of r_{p} will be discussed in detail later.

When the crack propagates under a relatively small velocity ($v/v_c = 0.0019$), the gradient in crack-tip hydrostatic pressure σ_{h} drives the guest atoms to diffuse toward the crack tip and accumulate ahead of the tip through Eqs. (4.13)-(4.15). As we can see from contour plot a1, such ion diffusion results in a small localized region of high guest species concentration ahead of the crack tip, which corresponds to the peak value of $\Delta\xi$ in line plot Fig. 4.6(b). Due to the influx of guest species, the localized area surrounding the crack tip expands, which, in return, lowers the stress states (a2 in Figs. 4.6(a) and (c)). The reduction in stress arises from the fact that the volumetric expansion causes a stress-free strain E_{ij}^{c}, as shown in the decomposition in Eq. (4.5). For a given total strain, an increase in E_{ij}^{c} will lower the elastic strain E_{ij}^{e}, leading to a corresponding

reduction in stress (we only consider elastic deformation in this study, where $E_{ij} = E_{ij}^{\mathrm{c}} + E_{ij}^{\mathrm{e}}$). The guest species diffuses toward the crack tip until an equilibrium between the electrochemical and mechanical driving forces is achieved. For relatively small v/v_c (varying from 0.00001 to 0 0.0079), there is plenty of time for guest atoms to diffuse toward the crack tip so that the redistribution of guest species and the relaxation of hydrostatic stress are nearly complete, and therefore $\mathrm{A}_{\xi}\mathrm{B}$ is always fully saturated with A under this equilibrium. We refer such an equilibrium state in the SCG regime as a saturated state. In this state, a relatively constant value of effective fracture energy is maintained, as can be seen from the plateau value of $G_{\mathrm{c}}^{\mathrm{eff}}$ corresponding to small v in Fig. 4.5.

As v/v_c increases, however, the amount of guest species delivered to the crack tip becomes less than the amount needed to sustain the saturated state, which causes the decrease of the guest species concentration ahead of the crack tip (contour plot b1 in Fig. 4.6(a) and curve b1 in Fig. 4.6(b)) and the corresponding reduction in effective fracture energy. The hydrostatic stress in this case cannot be fully relaxed, as we can see from the line plot in Fig. 4.6(b).

To further illustrate the intriguing phenomena existing in this transition regime, we resort to the R curve corresponding to point b. We make contour plots of $\Delta\xi = \xi - \xi_0$ and σ_{h} (Fig. 4.7(a)) at four successive time instants which are marked as A-D on the R curve. The evolution curves of $\Delta\xi = \xi - \xi_0$ and σ_{h} along the crack line are plotted in Figs. 4.7(b) and (c). As the remote loading is applied, the gradient of hydrostatic pressure drives ions to diffuse toward the crack tip and causes ion

accumulation around the crack tip. When the energy release rate reaches the threshold to create new surfaces (point A in Fig. 4.4), the crack starts to grow. However, the crack growth velocity is so large that ion diffusion is not able to capture the movement of the crack tip. Therefore, the localized region of high ion concentration starts to lag behind the crack tip (contour plot B1), which also corresponds to a significant drop in the peak value of $\Delta\xi$ from curve A1 to curve B1 in Fig. 4.7(b). This hysteretic phenomenon is more evident as the crack further propagates till time instant C. Two localized regions of high ion concentration exist ahead of and in the wake of the crack tip, respectively. However,

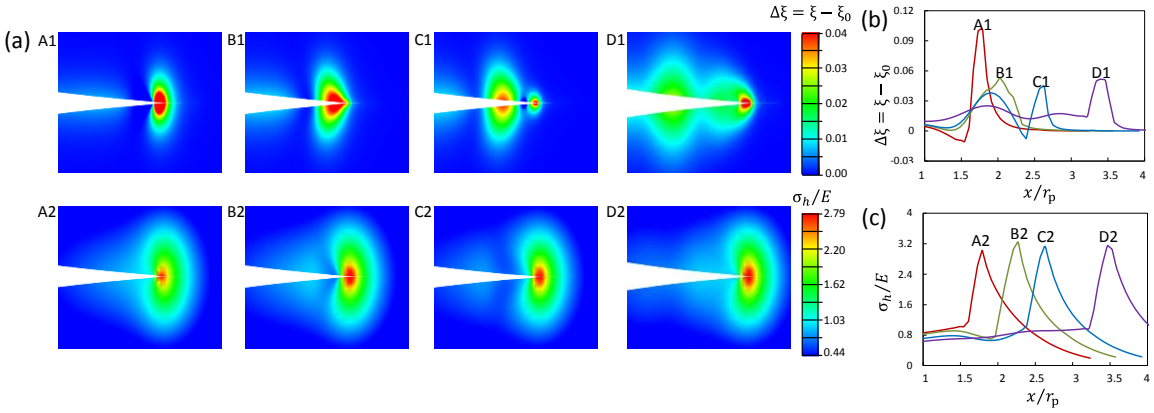

Figure 4.7 (a) Contour plots of the change in guest species concentration $\Delta\xi = \xi - \xi_0$ (A1-D1) and hydrostatic stress σ_h (A2-D2) corresponding to four time instants (A-D) marked on the R curve in Fig. 4.4. (b) and (c) Line plots of $\Delta\xi$ and σ_h along the crack line.

under both electrochemical and mechanical driving forces, the ions in the wake of the crack tip continue to diffuse toward their surroundings as crack further propagates. Such diffusion eventually results in an enlarged region of high ion concentration ahead of the crack tip and a considerably less concentrated region of ions in the wake of the crack tip at time instant D (contour plot D1 in Fig. 4.7(a) and curve D1 in Fig. 4.7(b)). Beyond this

time instant, an equilibrium between ion diffusion and crack propagation is reached and maintained, giving rise to a plateau value of J-integral. It is worth noting that in achieving the equilibrium state, the negotiation of crack with local ion diffusion results in a compromised region of high ion concentration ahead of the crack tip (contour plot D1), which is dramatically smaller compared with that in A1 when crack initially propagates. The corresponding peak value of $\Delta\xi$ is also much lower in curve D1than that in curve A1.

The intriguing competition between ion diffusion and crack propagation in the transition region has a significant effect on the effective fracture energy. When the crack growth velocity increases beyond a critical value $v/v_c = 24.72$ in the FCG regime, crack propagates so fast that it is virtually impossible for an appreciable amount of guest atoms to travel to the front of the crack tip, which can be clearly observed from the almost zero deviation of ξ from ξ_0 in contour plot c1of Fig. 4.6(a) and the corresponding c1 curve in Fig. 4.6(b). Therefore, the effective fracture energy in the FCG regime converges to the intrinsic fracture energy of the initially prescribed guest species concentration ξ_0. The hydrostatic stress in this case cannot be relaxed through stress-diffusion coupling.

We now turn to in-plane stress component σ_{yy}, which is related to the effective fracture energy through Eq. (4.16). The maximum σ_{yy} value around the crack tip represents the strength of the crack interface. Contour plots a3-c3 in Fig. 4.6(a) illustrate σ_{yy} around the crack tip under the three crack growth velocities (a-c) marked on the G_c^{eff} curve in Fig. 4.5. Their corresponding curves along the crack line are plotted in Fig. 4.6(d). From contour plots a3-c3 and Fig. 4.6(d), we observe that the peak value of σ_{yy}

increases as the crack growth velocity decreases from the FCG to the SCG regime, which corresponds to an increase in effective fracture energy from the intrinsic fracture energy in the FCG regime to a much higher plateau value in the SCG regime.

The enhancement in fracture energy implies that guest species diffusion and redistribution in the SCG regime can induce exceptional toughening of ion-storage materials. This enhancement has practical implications for the operation of ion-storage material systems, such as lithium-ion batteries, where repeated Li insertion into and extraction from the electrode materials can generate stresses and cause cracking of the electrode materials. Diffusion-induced toughening within the SCG regime suggests that a relatively slow charging rate of a battery, which allows sufficient time for ions to diffuse toward and accumulate ahead of the crack tip, can lead to higher fracture energy. Such higher fracture energy can retard damage accumulation and crack growth, which may ultimately avert fracture and enable durable batteries.

It is also worth noting that in Fig. 4.6(d), point O corresponds to the cohesive crack tip depicted in Fig. 4.1. Under a combined electrochemical and mechanical loading, σ_{yy} reaches its maximum value at point M. Further increase in the driving force results in a reduction in σ_{yy} and the ultimate creation of two new surfaces at point P, which corresponds to the physical crack tip. Therefore, the distance between P and O in Fig. 6(d) is measured as the cohesive zone size r_p, which is almost identical for the three loading conditions and used as a characteristic length during the description of $\Delta\xi$, σ_h, and σ_{yy} curves in this work.

The discussion above is concerned with the case of $\chi = \frac{1}{G_c^0}\frac{dG_c}{d\xi} = 3.33$, where the diffusion of ions leads to the toughening of ion-storage materials. The mechanism for the case of $\chi = \frac{1}{G_c^0}\frac{dG_c}{d\xi} = 0.66$ is similar, with the mere difference being that the toughening effect is weaker. In what follows, we will discuss the case of diffusion-induced embrittlement with $\chi = \frac{1}{G_c^0}\frac{dG_c}{d\xi} = -3.33$ as a representative example.

In Fig. 4.8 we show the contour plots of $\Delta\xi = \xi - \xi_0$, σ_h, and σ_{yy} under three loading conditions (d-f) marked on the G_c^{eff} curve in Fig. 4.5. Their corresponding curves along the crack line are plotted in Figs. 4.8(b-c). The general features of these plots are similar to those for $\chi = 3.33$. Within the SCG regime, guest ions accumulate ahead of the crack tip, causing a localized region of high $\Delta\xi$ (contour plot d1). Such ion accumulation is driven by the gradient in hydrostatic stress and, in return, relaxes the crack-tip stress through the stress-diffusion coupling. The diffusion of guest species and stress relaxation are nearly in equilibrium within the SCG regime so that the variation of crack growth velocities (v/v_c varying from 0.00001 to 0 0.0079) in this regime bears no significant influence on the effective fracture energy. However, if the crack propagates at a much faster speed, guest ions do not have sufficient time to diffuse toward the crack tip. Further increase in the crack growth velocity leads to little ion redistribution, as can be seen from the almost flat curve of $\Delta\xi$ for f1 in Fig. 4.8(b). The hydrostatic stress σ_h in this case, has little relaxation as well. The major difference between the outputs for $\chi = -3.33$ and $\chi = 3.33$ lies in that diffusion induces the embrittlement of ion-storage materials

for $\chi = -3.33$. Consequently, we can see the decreased peak values for σ_{yy} and a corresponding reduction in G_c^{eff} as the crack growth velocity decreases from the FCG to the SCG regime.

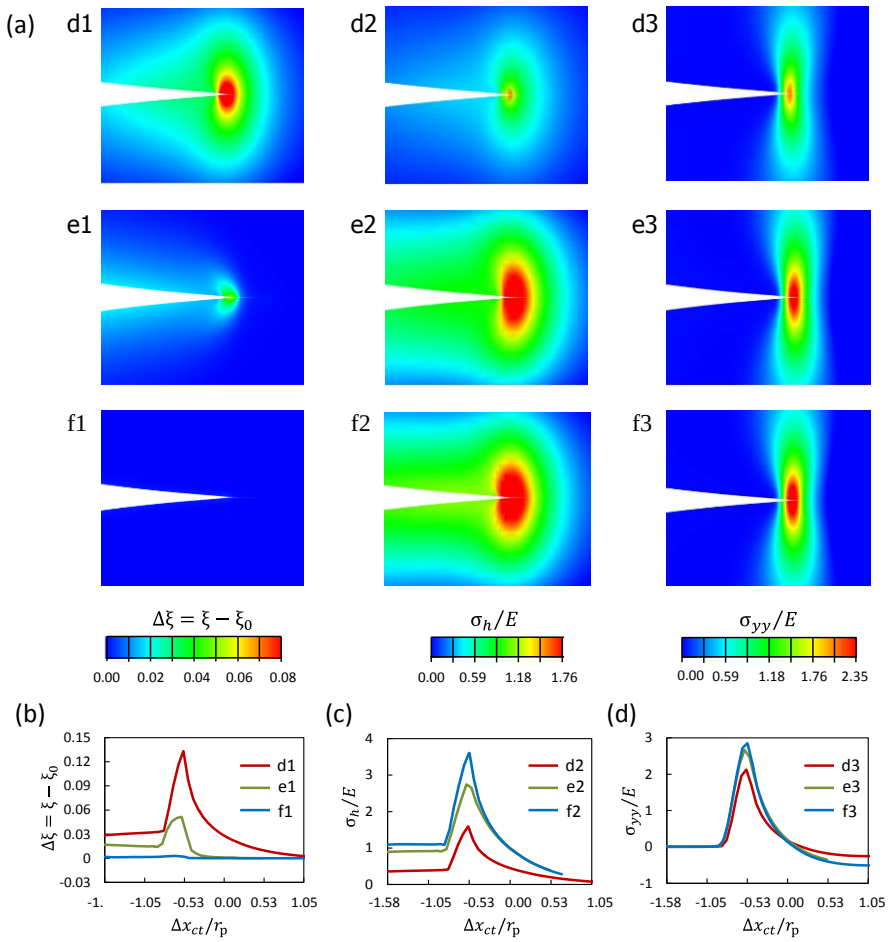

Figure 4.8 (a) Contour plots for $\Delta\xi = \xi - \xi_0$ (d1-f1), σ_h (d2-f2) and σ_{yy} (d3-f3) under three distinct loading conditions (d-f) marked on the G_c^{eff} curve in Fig. 4.5. (b)-(d) are the corresponding $\Delta\xi$, σ_h and σ_{yy} curves shown in the contour plots in (a).

Embrittlement due to insertion and diffusion of atoms occurs in many material systems. Take tin (Sn), a high-capacity anode material for lithium- and sodium-ion batteries, for example, recent in-situ X-ray transmission microscopy (TXM) [176],

transmission electron microscopy (TEM) [177], and synchrotron X-ray hard nanotomography [178] reveal that, in distinct contrast to the ductile nature of Sn metal, the lithiated/sodiated region of micron-sized Sn nanoparticles suffer from cracking after electrochemical testing. The occurrence of cracks indicates the brittle behavior of intermetallic compound Li_xSn, which is probably induced by Li/Na ion insertion and diffusion during electrochemical testing. Although the fundamental mechanism of cracking in lithiated/sodiated tin nanoparticles warrants further investigation, the study here provides important guidelines for the operation of material systems exhibiting diffusion-induced embrittlement, from the perspective of fracture resistance. In these material systems, a relatively fast charging rate, under which ions do not have sufficient time to diffuse toward the crack tip, can avoid ion accumulation ahead of the crack tip and mitigate the corresponding embrittlement effect.

The presented study here provides a fundamental understanding of the fracture mechanism in ion-storage materials under both electrochemical and mechanical driving forces and sheds light on the operation and mechanical testing of such material systems. For the operation of a material system where ion diffusion induces toughening, a crack growth velocity that falls within the SCG regime is favorable, which can attain the toughening effect and increase the damage tolerance of the material. For a material system where ion-diffusion-induced embrittlement happens, a crack growth velocity beyond the SCG regime can avoid the embrittlement effect due to ion diffusion and therefore is desired for the design and operation of the material system. On the other hand, the investigation on the effective fracture properties of ion-storage materials also provides significant insights for the mechanical characterization of these material systems,

where the intrinsic mechanical properties are desired. The asymptotic value of the effective fracture energy for sufficiently large crack growth velocities suggests that during mechanical testing, a crack growth velocity maintained within the FCG regime can prevent ion-diffusion-induced changes in local fracture properties at the crack tip and therefore enable accurate measurement of intrinsic fracture properties.

In our previous work [171], nanoindentation was performed on lithiated silicon samples to evaluate their fracture toughness and fracture energy as a function of Li concentration using Morris's model. In the model, thin film cracking caused by a sharp indenter tip is governed by the pre-existing film-stress field and two elastic stress fields due to indentation as illustrated in Eqs. (4-6) in Chapter 2. The fracture toughness of the test material is comprised of three components arising from these stress fields. Eqs. (4-6) reveal that the evaluation of the film stress, film thickness and factor Ψ are all dependent on the local Li concentration where nanoindentation was performed. Therefore, it is critical to evaluate the crack growth velocity during nanoindentation to ensure that the Li concentration ahead of the crack tip remains unchanged during the testing and the intrinsic fracture properties under this Li concentration is obtained.

In the nanoindentation testing, peak loads ranging from 1 to 93 mN at constant loading and unloading rates of 500 $\mu N/s$ were used for all nanoindentation tests. Based on the magnitude of the indentation load, three cracking behaviors (1) no cracking, (2) radial cracking, and (3) massive cracking were discovered. The crack growth velocity during nanoindentation testing can be calculated as $v=(c-a)/(t_{rc}-t_{nc})$, where, a refers to the center-to-corner distance of the indent, c refers to the average radial crack length measured from the center of the indent to the ends of the radial cracks, and t_{rc} and t_{nc} are

the times to reach the peak load for radial cracking and no cracking, respectively. The crack growth velocity for $Li_{0.87}Si$ is determined to be 218 nm/s, and the corresponding characteristic crack growth velocity $v_c = ED/G_c^0$ is calculated to be 106.9. According to Fig. 4.5, the normalized crack growth velocity of $v/v_c = 2.04$ falls within the FCG regime. This indicates that the duration of the nanoindentation testing is sufficiently short to suppress lithium diffusion toward the crack tip. Therefore, the fracture properties measured in the nanoindentation experiment are considered to be intrinsic.

4.3.2 Fracture behaviors of lithiated nanostructures

The finite element model presented in Section 4.2 is also applied to study the fracture behaviors of Si and Ge nanoparticles during electrochemical cycling. An initial crack is placed at the edge of Si and Ge nanoparticles. Three particle diameters, 100 nm, 250 nm, and 500nm, are used for both Si and Ge in the parametric study, with the initial crack length being 4% of the particle diameter in each simulation. Due to the geometry and loading symmetry about the crack plane, half of the nanoparticles are modeled. A two-phase lithiation mechanism, which has been recently observed in the lithiation of amorphous and crystalline Si [179-181], is implemented into the model by employing a double-well potential [182]. In addition, the experimentally characterized fracture properties from our previous work [171, 183] are incorporated into this model to substantially improve its predictive capability.

In this study, a linear mixture rule is used to calculate composition-dependent bulk and shear moduli. A yield stress of 1 GPa and 0.5 GPa are used for lithiated Si and Ge, respectively to simulate their elastic-plastic behavior. Figure 4.9 shows the simulated

fracture behaviors of Si and Ge nanoparticles during lithiation. Si nanoparticles (SiNPs) have been found to exhibit size-dependent fracture upon lithiation. No cracking is observed for a small particle diameter of 100 nm (Fig. 4.9a), but fracture is seen for particle diameters of 250 nm and 500 nm (Figs. 4.9b and c). In distinct contrast to SiNPs, Ge nanoparticles (GeNPs) have been found to undergo no visible cracking for all the three diameters simulated. These simulation results are consistent with the experimental observations reported by previous works [24, 60]. Ge nanoparticles are more robust than their Si counterparts, and therefore is a promising electrode material candidate for durable, high-rate rechargeable batteries.

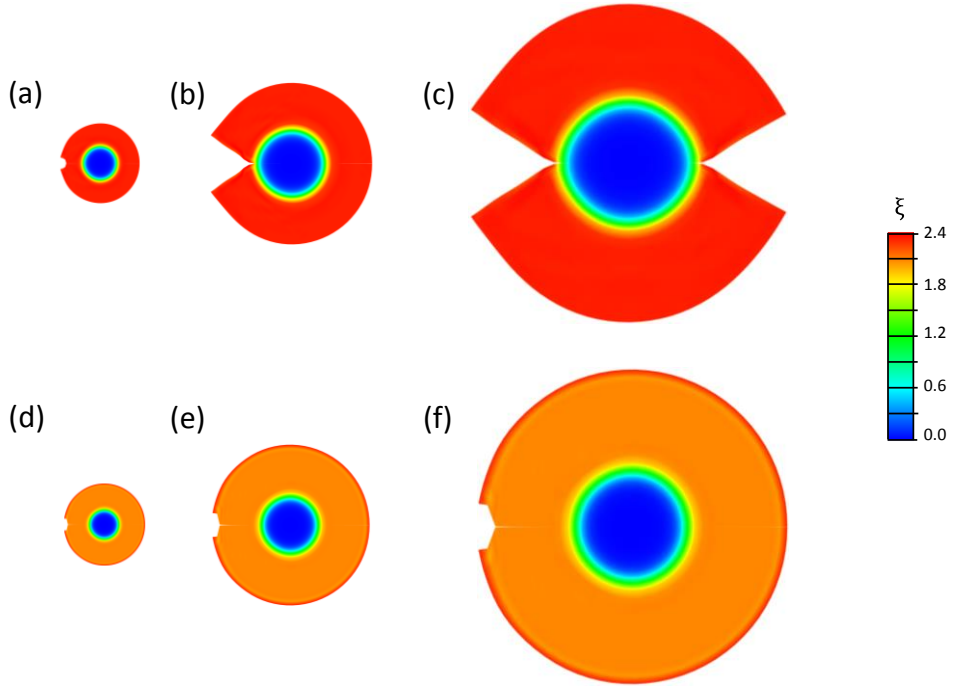

Figure 4.9 (a-c) Size-dependent fracture of lithiated Si nanoparticles. (d-e) Robustness of lithiated Ge nanoparticles. The initial diameters used for the three Si and Ge nanoparticles are 100 nm, 250nm, and 500nm.

4.4 Summary

We develop a composition-dependent cohesive zone model and integrate it with a chemo-mechanical coupling continuum model. We first apply the computational framework to study the effective fracture properties of ion-storage materials. We show that a competition between ion diffusion and crack propagation under both electrochemical and mechanical driving forces determines the ultimate effective fracture energy in these materials. When the crack growth velocity is small, ions have sufficient time to diffuse toward the crack tip and thus the crack tip is always fully saturated with ions under the equilibrium state. Such ion transport and diffusion can provide effective shielding or amplification of the crack-tip driving force. As crack growth velocity further increases, the competition between ion diffusion and crack growth is more evident, which results in a dramatic change of the effective fracture energy. For sufficiently large crack growth velocities, crack propagation is so fast that ions nearly have no time to diffuse toward the crack tip. Therefore, the effective fracture energy converges to the intrinsic fracture energy of ion-storage materials with a prescribed ion concentration.

The quantitative investigation on the effective fracture properties of ion-storage materials can provide significant insights for the operation and mechanical testing of ion-storage materials. For ion-storage materials where diffusion induces toughening, a relatively slow operation condition that allows complete ion diffusion can enhance the effective fracture energy and retard damage accumulation and crack growth. While for material systems where diffusion-induced embrittlement happens, a relatively fast operation condition can suppress ion diffusion and redistribution around the crack tip and therefore avoid the embrittlement effect. On the other hand, for mechanical testing where

intrinsic fracture properties are desired, a relatively large crack growth velocity that allows for no ion redistribution is favorable. It is also worth noting that the current study is based on the assumptions of mode I loading conditions and fully elastic solids. While more complex conditions, such as plasticity, are worth further study, the conclusions drawn from the present results are of general significance for the design and mechanical characterization of ion-storage material systems.

We also apply the integrated model to study the fracture behaviors of lithaited Si and Ge nanostructures by implementing a two-phase lithiation mechanism and incorporating the experimentally characterized fracture properties from our previous work. The results reveal that SiNPs exhibit size-dependent fracture, while GeNPs experience no obvious cracking under the same characteristic structural size. GeNPs are more robust than their Si counterparts and therefore is a more promising candidate for durable rechargeable batteries.

CHAPTER 5 CONCLUDING REMARKS

5.1 Significance of contribution

Energy storage with high performance and low cost is critical for applications in consumer electronics, zero-emission electric vehicles and stationary power management. LIBs are one of the most widely used energy storage systems due to their superior performance. The operation of a LIB involves repeated insertion and extraction of Li ions in active battery electrodes, which are often accompanied with considerable volume changes and stress generation. In the development of next-generation LIBs, mechanical degradation in high-capacity electrode materials arises as a bottleneck. Such high-capacity electrode materials usually experience large volume changes, leading to high mechanical stresses and fracture of electrodes during electrochemical cycling. Fracture causes the loss of active materials and yields more surface areas for solid electrolyte interphase (SEI) growth, both of which contribute to the fast capacity fade of LIBs.

To mitigate the mechanical degradation in LIBs, it is essential to quantitatively understand the electrochemically-induced mechanical responses and fundamental mechanical properties of high-capacity electrode materials. The past decade has witnessed a marked increase in studies on the mechanical behaviors of high-capacity electrode materials. Significant progress has been made in the experimental measurement and modelling of lithiation/delithiation-induced stresses, Li concentration-dependent modulus and hardness, time-dependent creep and strain-rate sensitivities. However, there is still a critical lack of fundamental understanding on the fracture-related properties,

which ultimately dictate the resistance of the electrode material to mechanical degradation and failure.

We have conducted an integrated experimental and computational investigation on the damage tolerance of lithiated Si. The *in situ* nanomechanical bending test on a partially lithiated Si nanowire inside a TEM reveals a direct contrast between the low fracture resistance in the brittle core of pristine Si and the high damage tolerance in the ductile shell of fully lithiated Si. Concurrently, we conduct systematic measurements of the fracture toughness of lithiated Si thin films with an in-housed developed nanoindentation system under precisely controlled electrochemical and mechanical conditions. We show a rapid brittle-to-ductile transition of fracture in Li_xSi alloys with increasing Li concentration. These experimental findings are interpreted by performing continuum finite and molecular dynamics simulations to gain mechanistic insights into the fracture mechanisms of lithiated Si. The integrated experimental and computational study has important implications for the development of durable Si-based anodes for next-generation LIBs.

Using the developed nanoindentation system, we also measured the fracture toughness of lithiated Ge for the first time. The fracture toughness of lithiated Ge is found to increase monotonically with increasing lithium content, indicating a brittle-to-ductile transition of lithiated Ge as lithiation proceeds. A comparison between the fracture energy of lithiated Ge and that of lithiated Si shows that, despite slightly lower fracture energy of Ge than that of Si in the unlithiated state, Ge possesses much higher fracture resistance than Si in the lithiated state. These findings indicate that Ge anodes are intrinsically more resistant to fracture than their Si counterparts, thereby offering

substantial potential for the development of durable, high-capacity, and high-rate LIBs. The quantitative results provide fundamental insights for developing new electrode materials and help to enable predictive modeling of high-performance LIBs.

The fundamental mechanisms of electrochemical reaction, microstructural evolution, and mechanical degradation in various rechargeable battery electrodes have also been extensively investigated by in-situ transmission electron microscopy (TEM) at the nanoscale. Despite of its widespread use for material characterizations, much of the TEM work till date has been focused on direct imaging and crystallographic analysis. We present a quantitative deformation measurement method by combing digital image correlation (DIC) and high-resolution TEM, and apply it to the deformation analysis in the two-phase lithaition in a-Si. We show that the lithiation in a-Si occurs by the movement of an atomistically sharp phase boundary between the a-Si reactant and an amorphous a-$\mathrm{Li}_x\mathrm{Si}$ $(x = 2.33)$ product. Broadly, this TEM-DIC technique enables full-field deformation analysis at considerably small length scales, and thus provides a new avenue for nanoscale material characterization.

Informed by the experimentally measured deformation and fracture characteristics, we develop a computational cohesive zone model and integrate it with a chemo-mechanical two-way coupling continuum model. We apply the computational framework to evaluate the effective fracture properties of ion-storage materials. The results reveal that due to a competition between ion diffusion and crack propagation, relatively small crack growth velocities lead to the enhancement or embrittlement of fracture resistance, while intrinsic fracture properties are recovered under sufficiently large crack growth velocities. These results provide significant guidance for the operation

and mechanical characterization of ion-storage materials. We also apply the integrated continuum model to study the fracture behaviors of lithiated nanoparticles. We show that lithiated SiNPs exhibit a size-dependent fracture while their Ge counterparts experience no obvious cracks. This suggests that Ge is a more promising material for durable rechargeable batteries.

5.2 Future research directions

The proposed experimental and computational methodologies in this work can be extended to study other micro- or nano-structured electrode/electrolyte architectures in various electrochemical systems.

Li-ion batteries have been under substantial investigation over the past few decades and have been widely used in various applications. Currently, sodium-ion batteries (SIBs) are being considered as potential low-cost candidates for large-scale energy storage applications in renewable energy and power grid due to the abundant and ubiquitous sodium resources. Since Li and Na share common properties as alkali metals, it is natural to transfer the insights gained from the science of LIBs to SIBs while accommodating the potential mass transport and storage problem brought by the larger radius of Na^+ than that of Li^+. For example, the nanomechanical study on anode materials for LIBs in this research can be applied to identify and characterize potential anode materials for SIBs. Furthermore, the experimental and computational methodologies in this work can also be extended to other rechargeable batteries, such as magnesium- and aluminum-ion batteries, and other electrochemical systems, such as fuel cells for energy conversion.

In addition, the mechanical property characterization and deformation analysis method can also be extended to all-solid-state batteries. This type of batteries has attracted substantial attention because they are potentially safer than conventional batteries based on liquid electrolytes. However, in these batteries, the volume change of active electrode materials during electrochemical cycling results in cracking and fracture, which is one of the critical causes for capacity fade and performance degradation of the batteries. The mechanical properties, such as elastic modulus, hardness and deformation, of solid electrolytes over cycling play a pivotal role in fracture. The nanoindentation technique in this research can be extended to characterize the elastic moduli and hardness of solid electrolytes, while their deformation can be quantitatively measured by coupling DIC analysis with SEM or TEM.

The current work focuses on the individual component of active electrode materials, such as pure Si thin films and nanoparticles. However, rechargeable battery electrodes are typically composite materials consisting of conductive binder and additives and are operated in the environment of liquid electrolyte. The computational methodologies in this study can be applied to the design of rechargeable batteries at the microstructural and device levels. Modeling the mechano-electrochemical response of composite electrodes has great practical importance for the design and operation of real battery systems.

REFERENCES

[1] J. M. Tarascon and M. Armand, "Issues and challenges facing rechargeable lithium batteries," *Nature*, vol. 414, pp. 359-367, Nov 2001.

[2] B. Dunn, H. Kamath, and J.-M. Tarascon, "Electrical energy storage for the grid: a battery of choices," *Science*, vol. 334, pp. 928-935, 2011.

[3] J. B. Goodenough and Y. Kim, "Challenges for Rechargeable Li Batteries," *Chemistry of Materials*, vol. 22, pp. 587-603, Feb 2010.

[4] A. Magasinski, P. Dixon, B. Hertzberg, A. Kvit, J. Ayala, and G. Yushin, "High-performance lithium-ion anodes using a hierarchical bottom-up approach," *Nature Materials*, vol. 9, pp. 353-358, Apr 2010.

[5] N. Liu, Z. Lu, J. Zhao, M. T. McDowell, H. W. Lee, W. Zhao, *et al.*, "A pomegranate-inspired nanoscale design for large-volume-change lithium battery anodes," *Nat Nanotechnol*, vol. 9, pp. 187-92, Mar 2014.

[6] Y. S. Hu, W. H. Kong, L. Hong, X. J. Huang, and L. Q. Chen, "Experimental and theoretical studies on reduction mechanism of vinyl ethylene carbonate on graphite anode for lithium ion batteries," *Electrochemistry Communications*, vol. 6, pp. 126-131, Feb 2004.

[7] D. Larcher, S. Beattie, M. Morcrette, K. Edstroem, J. C. Jumas, and J. M. Tarascon, "Recent findings and prospects in the field of pure metals as negative electrodes for Li-ion batteries," *Journal of Materials Chemistry*, vol. 17, pp. 3759-3772, 2007.

[8] M. N. Obrovac and L. Christensen, "Structural changes in silicon anodes during lithium insertion/extraction," *Electrochemical and Solid State Letters*, vol. 7, pp. A93-A96, 2004.

[9] M. N. Obrovac and L. J. Krause, "Reversible cycling of crystalline silicon powder," *Journal of the Electrochemical Society*, vol. 154, pp. A103-A108, 2007.

[10] J. Graetz, C. C. Ahn, R. Yazami, and B. Fultz, "Nanocrystalline and thin film germanium electrodes with high lithium capacity and high rate capabilities," *Journal of the Electrochemical Society*, vol. 151, pp. A698-A702, 2004.

[11] L. Y. Beaulieu, T. D. Hatchard, A. Bonakdarpour, M. D. Fleischauer, and J. R. Dahn, "Reaction of Li with alloy thin films studied by in situ AFM," *Journal of the Electrochemical Society*, vol. 150, pp. A1457-A1464, Nov 2003.

[12] X. H. Liu, Y. Liu, A. Kushima, S. L. Zhang, T. Zhu, J. Li, *et al.*, "In Situ TEM Experiments of Electrochemical Lithiation and Delithiation of Individual Nanostructures," *Advanced Energy Materials*, vol. 2, pp. 722-741, Jul 2012.

[13] X. Xiao, P. Liu, M. W. Verbrugge, H. Haftbaradaran, and H. Gao, "Improved cycling stability of silicon thin film electrodes through patterning for high energy density lithium batteries," *Journal of Power Sources,* vol. 196, pp. 1409-1416, Feb 1 2011.

[14] R. A. Huggins and W. D. Nix, "Decrepitation model for capacity loss during cycling of alloys in rechargeable electrochemical systems," *Ionics,* vol. 6, pp. 57-63, 2000.

[15] L. Y. Beaulieu, K. W. Eberman, R. L. Turner, L. J. Krause, and J. R. Dahn, "Colossal reversible volume changes in lithium alloys," *Electrochemical and Solid State Letters,* vol. 4, pp. A137-A140, Sep 2001.

[16] C. K. Chan, H. L. Peng, G. Liu, K. McIlwrath, X. F. Zhang, R. A. Huggins, *et al.*, "High-performance lithium battery anodes using silicon nanowires," *Nature Nanotechnology,* vol. 3, pp. 31-35, Jan 2008.

[17] Y. T. Cheng and M. W. Verbrugge, "Evolution of stress within a spherical insertion electrode particle under potentiostatic and galvanostatic operation," *Journal of Power Sources,* vol. 190, pp. 453-460, May 15 2009.

[18] K. Zhao, M. Pharr, J. J. Vlassak, and Z. Suo, "Fracture of electrodes in lithium-ion batteries caused by fast charging," *Journal of Applied Physics,* vol. 108, p. 073517, Oct 1 2010.

[19] V. A. Sethuraman, M. J. Chon, M. Shimshak, V. Srinivasan, and P. R. Guduru, "In situ measurements of stress evolution in silicon thin films during electrochemical lithiation and delithiation," *Journal of Power Sources,* vol. 195, pp. 5062-5066, Aug 1 2010.

[20] X. H. Liu, J. W. Wang, S. Huang, F. Fan, X. Huang, Y. Liu, *et al.*, "In situ atomic-scale imaging of electrochemical lithiation in silicon," *Nature Nanotechnology,* vol. 7, pp. 749-756, 2012.

[21] H. Li, X. J. Huang, L. Q. Chen, Z. G. Wu, and Y. Liang, "A high capacity nano-Si composite anode material for lithium rechargeable batteries," *Electrochemical and Solid State Letters,* vol. 2, pp. 547-549, Nov 1999.

[22] X. H. Liu, H. Zheng, L. Zhong, S. Huang, K. Karki, L. Q. Zhang, *et al.*, "Anisotropic Swelling and Fracture of Silicon Nanowires during Lithiation," *Nano Letters,* vol. 11, pp. 3312-3318, 2011.

[23] M. J. Chon, V. A. Sethuraman, A. McCormick, V. Srinivasan, and P. R. Guduru, "Real-Time Measurement of Stress and Damage Evolution during Initial Lithiation of Crystalline Silicon," *Physical Review Letters,* vol. 107, p. 045503, Jul 2011.

[24] X. H. Liu, L. Zhong, S. Huang, S. X. Mao, T. Zhu, and J. Y. Huang, "Size-Dependent Fracture of Silicon Nanoparticles During Lithiation," *Acs Nano,* vol. 6, pp. 1522-1531, Feb 2012.

[25] M. T. McDowell, S. W. Lee, J. T. Harris, B. A. Korgel, C. Wang, W. D. Nix, *et al.*, "In Situ TEM of Two-Phase Lithiation of Amorphous Silicon Nanospheres," *Nano Letters,* vol. 13, pp. 758-764, 2013/02/13 2013.

[26] M. T. McDowell, S. W. Lee, W. D. Nix, and Y. Cui, "25th Anniversary Article: Understanding the Lithiation of Silicon and Other Alloying Anodes for Lithium-Ion Batteries," *Advanced Materials,* vol. 25, pp. 4966-4984, Sep 2013.

[27] W. H. Woodford, Y. M. Chiang, and W. C. Carter, ""Electrochemical Shock" of Intercalation Electrodes: A Fracture Mechanics Analysis," *Journal of the Electrochemical Society,* vol. 157, pp. A1052-A1059, 2010.

[28] H. Haftbaradaran, X. C. Xiao, M. W. Verbrugge, and H. J. Gao, "Method to deduce the critical size for interfacial delamination of patterned electrode structures and application to lithiation of thin-film silicon islands," *Journal of Power Sources,* vol. 206, pp. 357-366, May 2012.

[29] H. Wang, B. Hou, X. Wang, S. Xia, and H. B. Chew, "Atomic-Scale Mechanisms of Sliding along an Interdiffused Li-Si-Cu Interface," *Nano Letters,* vol. 15, pp. 1716-1721, Mar 2015.

[30] F. Fan, S. Huang, H. Yang, M. Raju, D. Datta, V. B. Shenoy, *et al.*, "Mechanical properties of amorphous Li x Si alloys: a reactive force field study," *Modelling and Simulation in Materials Science and Engineering,* vol. 21, p. 074002, 2013.

[31] V. B. Shenoy, P. Johari, and Y. Qi, "Elastic softening of amorphous and crystalline Li-Si Phases with increasing Li concentration: A first-principles study," *Journal of Power Sources,* vol. 195, pp. 6825-6830, Oct 2010.

[32] B. Hertzberg, J. Benson, and G. Yushin, "Ex-situ depth-sensing indentation measurements of electrochemically produced Si-Li alloy films," *Electrochemistry Communications,* vol. 13, pp. 818-821, Aug 2011.

[33] L. A. Berla, S. W. Lee, Y. Cui, and W. D. Nix, "Mechanical behavior of electrochemically lithiated silicon," *Journal of Power Sources,* vol. 273, pp. 41-51, Jan 1 2015.

[34] S. T. Boles, C. V. Thompson, O. Kraft, and R. Moenig, "In situ tensile and creep testing of lithiated silicon nanowires," *Applied Physics Letters,* vol. 103, p. 263906, Dec 23 2013.

[35] M. Pharr, Z. Suo, and J. J. Vlassak, "Variation of stress with charging rate due to strain-rate sensitivity of silicon electrodes of Li-ion batteries," *Journal of Power Sources,* vol. 270, pp. 569-575, Dec 15 2014.

[36] A. Kushima, J. Y. Huang, and J. Li, "Quantitative fracture strength and plasticity measurements of lithiated silicon nanowires by in situ TEM tensile experiments," *ACS nano,* vol. 6, pp. 9425-9432, 2012.

[37] M. Pharr, Z. Suo, and J. J. Vlassak, "Measurements of the Fracture Energy of Lithiated Silicon Electrodes of Li-Ion Batteries," *Nano Letters,* vol. 13, pp. 5570-5577, Nov 2013.

[38] T. Chu, W. Ranson, and M. Sutton, "Applications of digital-image-correlation techniques to experimental mechanics," *Experimental Mechanics,* vol. 25, pp. 232-244, 1985.

[39] B. Pan, K. Qian, H. Xie, and A. Asundi, "Two-dimensional digital image correlation for in-plane displacement and strain measurement: a review," *Measurement Science and Technology,* vol. 20, p. 062001, 2009.

[40] W. H. Peters and W. F. Ranson, "Digital Imaging Techniques in Experimental Stress-Analysis," *Optical Engineering,* vol. 21, pp. 427-431, 1982.

[41] M. A. Sutton, M. Q. Cheng, W. H. Peters, Y. J. Chao, and S. R. Mcneill, "Application of an Optimized Digital Correlation Method to Planar Deformation Analysis," *Image and Vision Computing,* vol. 4, pp. 143-150, Aug 1986.

[42] C. Delacourt, P. Allemand, B. Casson, and H. Vadon, "Velocity field of the “La Clapière” landslide measured by the correlation of aerial and QuickBird satellite images," *Geophysical Research Letters,* vol. 31, 2004.

[43] J. D. Krehbiel, J. Lambros, J. Viator, and N. Sottos, "Digital image correlation for improved detection of basal cell carcinoma," *Experimental Mechanics,* vol. 50, pp. 813-824, 2010.

[44] Z. Wang, "Transmission electron microscopy of shape-controlled nanocrystals and their assemblies," *The Journal of Physical Chemistry B,* vol. 104, pp. 1153-1175, 2000.

[45] D. B. Williams and C. B. Carter, *Transmission electron microscope*: Springer, 2009.

[46] F. Larché and J. W. Cahn, "A linear theory of thermochemical equilibrium of solids under stress," *Acta Metallurgica,* vol. 21, pp. 1051-1063, 1973.

[47] F. C. Larche and J. W. Cahn, "The Effect of Self-Stress on Diffusion in Solids," *Acta Metallurgica,* vol. 30, pp. 1835-1845, 1982.

[48] F. C. Larche and J. W. Cahn, "The Interactions of Composition and Stress in Crystalline Solids," *Acta Metallurgica,* vol. 33, pp. 331-357, 1985.

[49] F. C. Larche and J. W. Cahn, "Stress Effects on Iii-V Solid-Liquid Equilibria," *Journal of Applied Physics,* vol. 62, pp. 1232-1239, Aug 15 1987.

[50] F. C. Larche and J. W. Cahn, "Phase-Changes in a Thin Plate with Nonlocal Self-Stress Effects," *Acta Metallurgica Et Materialia,* vol. 40, pp. 947-955, May 1992.

[51] W. C. Johnson, "Thermodynamic Equilibria in 2-Phase, Elastically Stressed Ionic-Crystals," *Journal of the American Ceramic Society,* vol. 77, pp. 1581-1591, Jun 1994.

[52] W. C. Johnson and H. Schmalzried, "Phenomenological Thermodynamic Treatment of Elastically Stressed Ionic-Crystals," *Journal of the American Ceramic Society,* vol. 76, pp. 1713-1719, Jul 1993.

[53] R. Krishnamurthy and B. W. Sheldon, "Stresses due to oxygen potential gradients in non-stoichiometric oxides," *Acta Materialia,* vol. 52, pp. 1807-1822, Apr 2004.

[54] N. Swaminathan and J. Qu, "Interactions between non-stoichiometric stresses and defect transport in a tubular electrolyte," *Fuel Cells,* vol. 7, pp. 453-462, Dec 2007.

[55] N. Swaminathan, J. Qu, and Y. Sun, "An electrochemomechanical theory of defects in ionic solids. Part II. Examples," *Philosophical Magazine,* vol. 87, pp. 1723-1742, 2007.

[56] N. Swaminathan, J. Qu, and Y. Sun, "An electrochemomechanical theory of defects in ionic solids. I. Theory," *Philosophical Magazine,* vol. 87, pp. 1705-1721, 2007.

[57] H. G. Zhou, J. M. Qu, and M. Cherkaoui, "Finite element analysis of oxidation induced metal depletion at oxide-metal interface," *Computational Materials Science,* vol. 48, pp. 842-847, Jun 2010.

[58] H. G. Zhou, J. M. Qu, and M. Cherkaoui, "Stress-oxidation interaction in selective oxidation of Cr-Fe alloys," *Mechanics of Materials,* vol. 42, pp. 63-71, Jan 2010.

[59] V. A. Sethuraman, V. Srinivasan, A. F. Bower, and P. R. Guduru, "In Situ Measurements of Stress-Potential Coupling in Lithiated Silicon," *Journal of the Electrochemical Society,* vol. 157, pp. A1253-A1261, 2010.

[60] A. F. Bower, P. R. Guduru, and V. A. Sethuraman, "A finite strain model of stress, diffusion, plastic flow, and electrochemical reactions in a lithium-ion half-cell," *Journal of the Mechanics and Physics of Solids,* vol. 59, pp. 804-828, Apr 2011.

[61] Y. F. Gao and M. Zhou, "Strong stress-enhanced diffusion in amorphous lithium alloy nanowire electrodes," *Journal of Applied Physics,* vol. 109, Jan 1 2011.

[62] Y. F. Gao, M. Cho, and M. Zhou, "Stress relaxation through interdiffusion in amorphous lithium alloy electrodes," *Journal of the Mechanics and Physics of Solids,* vol. 61, pp. 579-596, Feb 2013.

[63] S. Huang, F. Fan, J. Li, S. Zhang, and T. Zhu, "Stress generation during lithiation of high-capacity electrode particles in lithium ion batteries," *Acta Materialia,* vol. 61, pp. 4354-4364, Jul 2013.

[64] R. Purkayastha and R. M. McMeeking, "A Linearized Model for Lithium Ion Batteries and Maps for their Performance and Failure," *Journal of Applied Mechanics-Transactions of the Asme,* vol. 79, May 2012.

[65] J. Christensen and J. Newman, "A mathematical model of stress generation and fracture in lithium manganese oxide," *Journal of the Electrochemical Society,* vol. 153, pp. A1019-A1030, 2006.

[66] X. C. Zhang, W. Shyy, and A. M. Sastry, "Numerical simulation of intercalation-induced stress in Li-ion battery electrode particles," *Journal of the Electrochemical Society,* vol. 154, pp. A910-A916, 2007.

[67] K. J. Zhao, M. Pharr, S. Q. Cai, J. J. Vlassak, and Z. G. Suo, "Large Plastic Deformation in High-Capacity Lithium-Ion Batteries Caused by Charge and Discharge," *Journal of the American Ceramic Society,* vol. 94, pp. S226-S235, Jun 2011.

[68] K. J. Zhao, M. Pharr, J. J. Vlassak, and Z. G. Suo, "Inelastic hosts as electrodes for high-capacity lithium-ion batteries," *Journal of Applied Physics,* vol. 109, Jan 1 2011.

[69] L. Anand, "A Cahn-Hilliard-type theory for species diffusion coupled with large elastic-plastic deformations," *Journal of the Mechanics and Physics of Solids,* vol. 60, pp. 1983-2002, Dec 2012.

[70] Z. W. Cui, F. Gao, and J. M. Qu, "A finite deformation stress-dependent chemical potential and its applications to lithium ion batteries," *Journal of the Mechanics and Physics of Solids,* vol. 60, pp. 1280-1295, Jul 2012.

[71] Y. T. Cheng and M. W. Verbrugge, "The influence of surface mechanics on diffusion induced stresses within spherical nanoparticles," *Journal of Applied Physics,* vol. 104, Oct 15 2008.

[72] W. H. Woodford, W. C. Carter, and Y. M. Chiang, "Design criteria for electrochemical shock resistant battery electrodes," *Energy & Environmental Science,* vol. 5, pp. 8014-8024, Jul 2012.

[73] W. H. Woodford, Y. M. Chiang, and W. C. Carter, "Electrochemical Shock in Ion-Intercalation Materials with Limited Solid-Solubility," *Journal of the Electrochemical Society,* vol. 160, pp. A1286-A1292, 2013.

[74] K. Rhodes, M. Kirkham, R. Meisner, C. M. Parish, N. Dudney, and C. Daniel, "Novel cell design for combined in situ acoustic emission and x-ray diffraction study during electrochemical cycling of batteries," *Review of Scientific Instruments,* vol. 82, Jul 2011.

[75] T. Ohzuku, H. Tomura, and K. Sawai, "Monitoring of particle fracture by acoustic emission during charge and discharge of Li/MnO2 cells," *Journal of the Electrochemical Society,* vol. 144, pp. 3496-3500, Oct 1997.

[76] N. Kircheva, S. Genies, C. Chabrol, and P. X. Thivel, "Evaluation of acoustic emission as a suitable tool for aging characterization of LiAl/LiMnO2 cell," *Electrochimica Acta,* vol. 88, pp. 488-494, Jan 15 2013.

[77] K. E. Aifantis, S. A. Hackney, and J. P. Dempsey, "Design criteria for nanostructured Li-ion batteries," *Journal of Power Sources,* vol. 165, pp. 874-879, Mar 20 2007.

[78] K. J. Zhao, M. Pharr, J. J. Vlassak, and Z. G. Suo, "Fracture of electrodes in lithium-ion batteries caused by fast charging," *Journal of Applied Physics,* vol. 108, Oct 1 2010.

[79] Y. F. Gao and M. Zhou, "Coupled mechano-diffusional driving forces for fracture in electrode materials," *Journal of Power Sources,* vol. 230, pp. 176-193, May 15 2013.

[80] R. Grantab and V. B. Shenoy, "Pressure-Gradient Dependent Diffusion and Crack Propagation in Lithiated Silicon Nanowires," *Journal of the Electrochemical Society,* vol. 159, pp. A584-A591, 2012.

[81] A. F. Bower and P. R. Guduru, "A simple finite element model of diffusion, finite deformation, plasticity and fracture in lithium ion insertion electrode materials," *Modelling and Simulation in Materials Science and Engineering,* vol. 20, Jun 2012.

[82] J. Y. Huang, L. Zhong, C. M. Wang, J. P. Sullivan, W. Xu, L. Q. Zhang, *et al.*, "In Situ Observation of the Electrochemical Lithiation of a Single SnO2 Nanowire Electrode," *Science,* vol. 330, pp. 1515-1520, Dec 2010.

[83] R. F. Cook, "Strength and sharp contact fracture of silicon," *Journal of Materials Science,* vol. 41, pp. 841-872, Feb 2006.

[84] G. G. Stoney, "The tension of metallic films deposited by electrolysis," *Proceedings of the Royal Society of London Series a-Containing Papers of a Mathematical and Physical Character,* vol. 82, pp. 172-175, May 1909.

[85] S. Guo, M. Sutton, X. Li, N. Li, and L. Wang, "SEM-DIC based nanoscale thermal deformation studies of heterogeneous material," in *Advancement of*

Optical Methods in Experimental Mechanics, Volume 3, ed: Springer, 2014, pp. 145-150.

[86] W. T. Liang, H. Yang, F. F. Fan, Y. Liu, X. H. Liu, J. Y. Huang, *et al.*, "Tough Germanium Nanoparticles under Electrochemical Cycling," *ACS Nano,* vol. 7, pp. 3427-3433, Apr 2013.

[87] D. J. Morris and R. F. Cook, "Indentation fracture of low-dielectric constant films: Part I. Experiments and observations," *Journal of Materials Research,* vol. 23, pp. 2429-2442, Sep 2008.

[88] D. J. Morris and R. F. Cook, "Indentation fracture of low-dielectric constant films: Part II. Indentation fracture mechanics model," *Journal of Materials Research,* vol. 23, pp. 2443-2457, Sep 2008.

[89] W. C. Oliver and G. M. Pharr, "An improved technique for determining hardness and elastic modulus using load and displacement sensing indentation experiments," *Journal of materials research,* vol. 7, pp. 1564-1583, 1992.

[90] B. R. Lawn, A. Evans, and D. Marshall, "Elastic/plastic indentation damage in ceramics: the median/radial crack system," *Journal of the American Ceramic Society,* vol. 63, pp. 574-581, 1980.

[91] S. Huang, F. Fan, J. Li, S. L. Zhang, and T. Zhu, "Stress generation during lithiation of high-capacity electrode particles in lithium ion batteries," *Acta Materialia,* vol. 61, pp. 4354-4364, 2013.

[92] S. P. V. Nadimpalli, V. A. Sethuraman, G. Bucci, V. Srinivasan, A. F. Bower, and P. R. Guduru, "On Plastic Deformation and Fracture in Si Films during Electrochemical Lithiation/Delithiation Cycling," *Journal of the Electrochemical Society,* vol. 160, pp. A1885-A1893, 2013.

[93] C.-Y. Chou and G. S. Hwang, "Surface effects on the structure and lithium behavior in lithiated silicon: A first principles study," *Surface Science,* vol. 612, pp. 16-23, 2013.

[94] L. A. Berla, S. W. Lee, I. Ryu, Y. Cui, and W. D. Nix, "Robustness of amorphous silicon during the initial lithiation/delithiation cycle," *Journal of Power Sources,* vol. 258, pp. 253-259, Jul 15 2014.

[95] M. T. McDowell, I. Ryu, S. W. Lee, C. Wang, W. D. Nix, and Y. Cui, "Studying the Kinetics of Crystalline Silicon Nanoparticle Lithiation with In Situ Transmission Electron Microscopy," *Advanced Materials,* vol. 24, pp. 6034-6041, 2012.

[96] W. Liang, H. Yang, F. Fan, Y. Liu, X. H. Liu, J. Y. Huang, *et al.*, "Tough Germanium Nanoparticles under Electrochemical Cycling," *ACS Nano,* 2013.

[97] Y. Kamata, "High-k/Ge MOSFETs for future nanoelectronics," *Materials Today,* vol. 11, pp. 30-38, Jan-Feb 2008.

[98] C. S. Fuller and J. C. Severiens, "Mobility of Impurity Ions in Germanium and Silicon," *Physical Review,* vol. 96, pp. 21-24, 1954.

[99] K. C. Klavetter, S. M. Wood, Y. M. Lin, J. L. Snider, N. C. Davy, A. M. Chockla, *et al.*, "A high-rate germanium-particle slurry cast Li-ion anode with high Coulombic efficiency and long cycle life," *Journal of Power Sources,* vol. 238, pp. 123-136, Sep 15 2013.

[100] T. Song, Y. Jeon, M. Samal, H. Han, H. Park, J. Ha, *et al.*, "A Ge inverse opal with porous walls as an anode for lithium ion batteries," *Energy & Environmental Science,* vol. 5, pp. 9028-9033, Oct 2012.

[101] L. Baggetto and P. H. L. Notten, "Lithium-Ion (De)Insertion Reaction of Germanium Thin-Film Electrodes: An Electrochemical and In Situ XRD Study," *Journal of the Electrochemical Society,* vol. 156, pp. A169-A175, 2009.

[102] C. K. Chan, X. F. Zhang, and Y. Cui, "High capacity Li ion battery anodes using Ge nanowires," *Nano Letters,* vol. 8, pp. 307-309, Jan 2008.

[103] M. H. Park, Y. Cho, K. Kim, J. Kim, M. L. Liu, and J. Cho, "Germanium Nanotubes Prepared by Using the Kirkendall Effect as Anodes for High-Rate Lithium Batteries," *Angewandte Chemie-International Edition,* vol. 50, pp. 9647-9650, 2011.

[104] S. P. V. Nadimpalli and R. Tripuraneni, "Stress Response of Germanium Electrodes During Lithiation/Delithiation Cycling," *Proceedings of the ASME 2015 International Mehcanical Engineering Congress and Exposition,* 2015.

[105] T. Song, H. Cheng, H. Choi, J.-H. Lee, H. Han, D. H. Lee, *et al.*, "Si/Ge double-layered nanotube array as a lithium ion battery anode," *ACS Nano,* vol. 6, pp. 303-309, 2011.

[106] X. H. Liu and J. Y. Huang, "In situ TEM electrochemistry of anode materials in lithium ion batteries," *Energy & Environmental Science,* vol. 4, pp. 3844-3860, Oct 2011.

[107] S. W. Lee, W. D. Nix, and Y. Cui, "Fracture of crystalline germanium during electrochemical lithium insertion," *Extreme Mechanics Letters,* vol. 2, pp. 15-19, 2015.

[108] S. W. Lee, M. T. McDowell, L. A. Berla, W. D. Nix, and Y. Cui, "Fracture of crystalline silicon nanopillars during electrochemical lithium insertion," *Proceedings of the National Academy of Sciences of the United States of America,* vol. 109, pp. 4080-4085, Mar 13 2012.

[109] X. J. Wang, F. F. Fan, J. W. Wang, H. R. Wang, S. Y. Tao, A. Yang, *et al.*, "High Damage Tolerance of Electrochemically Lithiated Silicon," *Nature Communications,* vol. 6, p. 8417, 2015.

[110] J. C. Li, A. K. Dozier, Y. C. Li, F. Q. Yang, and Y. T. Cheng, "Crack Pattern Formation in Thin Film Lithium-Ion Battery Electrodes," *Journal of the Electrochemical Society,* vol. 158, pp. A689-A694, 2011.

[111] H. Haftbaradaran, X. C. Xiao, and H. J. Gao, "Critical film thickness for fracture in thin-film electrodes on substrates in the presence of interfacial sliding," *Modelling and Simulation in Materials Science and Engineering,* vol. 21, Oct 2013.

[112] J. Ye, Y. An, T. Heo, M. Biener, R. Nikolic, M. Tang, *et al.*, "Enhanced lithiation and fracture behavior of silicon mesoscale pillars via atomic layer coatings and geometry design," *Journal of Power Sources,* vol. 248, pp. 447-456, 2014.

[113] Y. Qi, L. G. Hector, C. James, and K. J. Kim, "Lithium concentration dependent elastic properties of battery electrode materials from first principles calculations," *Journal of The Electrochemical Society,* vol. 161, pp. F3010-F3018, 2014.

[114] X. H. Liu, S. Huang, S. T. Picraux, J. Li, T. Zhu, and J. Y. Huang, "Reversible nanopore formation in Ge nanowires during lithiation–delithiation cycling: An in situ transmission electron microscopy study," *Nano letters,* vol. 11, pp. 3991-3997, 2011.

[115] I. Chasiotis and W. G. Knauss, "A new microtensile tester for the study of MEMS materials with the aid of atomic force microscopy," *Experimental Mechanics,* vol. 42, pp. 51-57, Mar 2002.

[116] W. G. Knauss, I. Chasiotis, and Y. Huang, "Mechanical measurements at the micron and nanometer scales," *Mechanics of Materials,* vol. 35, pp. 217-231, Mar-Jun 2003.

[117] I. Chasiotis, "Mechanics of thin films and microdevices," *IEEE Transactions on Device and Materials Reliability,* vol. 4, pp. 176-188, Jun 2004.

[118] S. Cho, I. Chasiotis, T. A. Friedmann, and J. P. Sullivan, "Young's modulus, Poisson's ratio and failure properties of tetrahedral amorphous diamond-like carbon for MEMS devices," *Journal of Micromechanics and Microengineering,* vol. 15, pp. 728-735, Apr 2005.

[119] S. Cho, J. F. Cárdenas-García, and I. Chasiotis, "Measurement of nanodisplacements and elastic properties of MEMS via the microscopic hole method," *Sensors and Actuators A: Physical,* vol. 120, pp. 163-171, 2005.

[120] S. Chang, C. S. Wang, C. Y. Xiong, and J. Fang, "Nanoscale in-plane displacement evaluation by AFM scanning and digital image correlation processing," *Nanotechnology,* vol. 16, pp. 344-349, Apr 2005.

[121] Y. Sun and J. H. Pang, "AFM image reconstruction for deformation measurements by digital image correlation," *Nanotechnology,* vol. 17, p. 933, 2006.

[122] S. W. Cho and I. Chasiotis, "Elastic properties and representative volume element of polycrystalline silicon for MEMS," *Experimental Mechanics,* vol. 47, pp. 37-49, Feb 2007.

[123] X. D. Li, W. J. Xu, M. A. Sutton, and M. Mello, "In situ nanoscale in-plane deformation studies of ultrathin polymeric films during tensile deformation using atomic force microscopy and digital image correlation techniques," *IEEE Transactions on Nanotechnology,* vol. 6, pp. 4-12, Jan 2007.

[124] Y. Sun, J. H. Pang, and W. Fan, "Nanoscale deformation measurement of microscale interconnection assemblies by a digital image correlation technique," *Nanotechnology,* vol. 18, p. 395504, 2007.

[125] G. Vendroux and W. Knauss, "Submicron deformation field measurements: Part 1. Developing a digital scanning tunneling microscope," *Experimental Mechanics,* vol. 38, pp. 18-23, 1998.

[126] G. Vendroux and W. Knauss, "Submicron deformation field measurements: Part 2. Improved digital image correlation," *Experimental Mechanics,* vol. 38, pp. 86-92, 1998.

[127] G. Vendnroux, N. Schmidt, and W. Knauss, "Submicron deformation field measurements: Part 3. Demonstration of deformation determinations," *Experimental Mechanics,* vol. 38, pp. 154-160, 1998.

[128] J. Kang, M. Jain, D. S. Wilkinson, and J. D. Embury, "Microscopic strain mapping using scanning electron microscopy topography image correlation at large strain," *Journal of Strain Analysis for Engineering Design,* vol. 40, pp. 559-570, Aug 2005.

[129] N. Sabate, D. Vogel, A. Gollhardt, J. Keller, B. Michel, C. Cane, *et al.*, "Measurement of residual stresses in micromachined structures in a microregion," *Applied Physics Letters,* vol. 88, Feb 13 2006.

[130] F. Lagattu, F. Bridier, P. Villechaise, and J. Brillaud, "In-plane strain measurements on a microscopic scale by coupling digital image correlation and an in situ SEM technique," *Materials Characterization,* vol. 56, pp. 10-18, 2006.

[131] M. A. Sutton, N. Li, D. Garcia, N. Cornille, J. J. Orteu, S. R. McNeill, *et al.*, "Metrology in a scanning electron microscope: theoretical developments and

experimental validation," *Measurement Science and Technology,* vol. 17, p. 2613, 2006.

[132] M. Sutton, N. Li, D. Joy, A. Reynolds, and X. Li, "Scanning electron microscopy for quantitative small and large deformation measurements part I: SEM imaging at magnifications from 200 to 10,000," *Experimental Mechanics,* vol. 47, pp. 775-787, 2007.

[133] M. A. Sutton, N. Li, D. Garcia, N. Cornille, J. Orteu, S. McNeill, *et al.*, "Scanning electron microscopy for quantitative small and large deformation measurements part II: experimental validation for magnifications from 200 to 10,000," *Experimental Mechanics,* vol. 47, pp. 789-804, 2007.

[134] A. D. Kammers and S. Daly, "Digital image correlation under scanning electron microscopy: methodology and validation," *Experimental Mechanics,* vol. 53, pp. 1743-1761, 2013.

[135] A. D. Kammers and S. Daly, "Self-assembled nanoparticle surface patterning for improved digital image correlation in a scanning electron microscope," *Experimental Mechanics,* vol. 53, pp. 1333-1341, 2013.

[136] H. Jin, W. Lu, and J. Korellis, "Micro-scale deformation measurement using the digital image correlation technique and scanning electron microscope imaging," *The Journal of Strain Analysis for Engineering Design,* vol. 43, pp. 719-728, 2008.

[137] M. Tschopp, B. Bartha, W. Porter, P. Murray, and S. Fairchild, "Microstructure-dependent local strain behavior in polycrystals through in-situ scanning electron microscope tensile experiments," *Metallurgical and Materials Transactions A,* vol. 40, pp. 2363-2368, 2009.

[138] N. Sabate, D. Vogel, A. Gollhardt, J. Keller, C. Cane, I. Gracia, *et al.*, "Residual stress measurement on a MEMS structure with high-spatial resolution," *Journal of Microelectromechanical Systems,* vol. 16, pp. 365-372, Apr 2007.

[139] M. Hÿtch, E. Snoeck, and R. Kilaas, "Quantitative measurement of displacement and strain fields from HREM micrographs," *Ultramicroscopy,* vol. 74, pp. 131-146, 1998.

[140] E. Snoeck, B. Warot, H. Ardhuin, A. Rocher, M. Casanove, R. Kilaas, *et al.*, "Quantitative analysis of strain field in thin films from HRTEM micrographs," *Thin Solid Films,* vol. 319, pp. 157-162, 1998.

[141] M. Hÿtch, F. Houdellier, F. Hüe, and E. Snoeck, "Nanoscale holographic interferometry for strain measurements in electronic devices," *Nature,* vol. 453, pp. 1086-1089, 2008.

[142] P. Zhang, A. A. Istratov, E. R. Weber, C. Kisielowski, H. He, C. Nelson, *et al.*, "Direct strain measurement in a 65nm node strained silicon transistor by convergent-beam electron diffraction," *Applied Physics Letters,* vol. 89, p. 161907, 2006.

[143] P. Jones, G. Rackham, and J. Steeds, "Higher order Laue zone effects in electron diffraction and their use in lattice parameter determination," *Proceedings of the Royal Society of London A: Mathematical, Physical and Engineering Sciences,* vol. 354, pp. 197-222, 1977.

[144] A. Armigliato, R. Balboni, G. Carnevale, G. Pavia, D. Piccolo, S. Frabboni, *et al.*, "Application of convergent beam electron diffraction to two-dimensional strain mapping in silicon devices," *Applied Physics Letters,* vol. 82, pp. 2172-2174, 2003.

[145] K. Usuda, T. Numata, T. Irisawa, N. Hirashita, and S. Takagi, "Strain characterization in SOI and strained-Si on SGOI MOSFET channel using nano-beam electron diffraction (NBD)," *Materials Science and Engineering: B,* vol. 124, pp. 143-147, 2005.

[146] F. Uesugi, A. Hokazono, and S. Takeno, "Evaluation of two-dimensional strain distribution by STEM/NBD," *Ultramicroscopy,* vol. 111, pp. 995-998, 2011.

[147] A. Orlov, A. Granovsky, L. Balagurov, I. Kulemanov, Y. N. Parkhomenko, N. Perov, *et al.*, "Structure, electrical and magnetic properties, and the origin of the room temperature ferromagnetism in Mn-implanted Si," *Journal of Experimental and Theoretical Physics,* vol. 109, pp. 602-608, 2009.

[148] J. W. Wang, Y. He, F. Fan, X. H. Liu, S. Xia, Y. Liu, *et al.*, "Two-phase electrochemical lithiation in amorphous silicon," *Nano Letters,* vol. 13, pp. 709-715, 2013.

[149] W. Peters and W. Ranson, "Digital imaging techniques in experimental stress analysis," *Optical Engineering,* vol. 21, pp. 427-431, 1982.

[150] M. Sutton, W. Wolters, W. Peters, W. Ranson, and S. McNeill, "Determination of displacements using an improved digital correlation method," *Image and Vision Computing,* vol. 1, pp. 133-139, 1983.

[151] H. Lu and P. Cary, "Deformation measurements by digital image correlation: implementation of a second-order displacement gradient," *Experimental mechanics,* vol. 40, pp. 393-400, 2000.

[152] M. Bornert, F. Brémand, P. Doumalin, J.-C. Dupré, M. Fazzini, M. Grédiac, *et al.*, "Assessment of digital image correlation measurement errors: methodology and results," *Experimental mechanics,* vol. 49, pp. 353-370, 2009.

[153] H. Bruck, S. McNeill, M. A. Sutton, and W. Peters Iii, "Digital image correlation using Newton-Raphson method of partial differential correction," *Experimental Mechanics,* vol. 29, pp. 261-267, 1989.

[154] Y. Sun, J. H. Pang, C. K. Wong, and F. Su, "Finite element formulation for a digital image correlation method," *Applied Optics,* vol. 44, pp. 7357-7363, 2005.

[155] G. Besnard, F. Hild, and S. Roux, "“Finite-element” displacement fields analysis from digital images: application to Portevin–Le Châtelier bands," *Experimental Mechanics,* vol. 46, pp. 789-803, 2006.

[156] J. Réthoré, S. Roux, and F. Hild, "Hybrid analytical and extended finite element method (HAX - FEM): A new enrichment procedure for cracked solids," *International Journal for Numerical Methods in Engineering,* vol. 81, pp. 269-285, 2010.

[157] J. Réthoré, S. Roux, and F. Hild, "Mixed-mode crack propagation using a hybrid analytical and extended finite element method," *Comptes Rendus Mécanique,* vol. 338, pp. 121-126, 2010.

[158] M. L. Williams, "On the stress distribution at the base of a stationary crack," *ASME Journal of Applied Mechanics,* vol. 24, pp. 109-114, 1957.

[159] F. Hild and S. Roux, "Comparison of local and global approaches to digital image correlation," *Experimental Mechanics,* vol. 52, pp. 1503-1519, 2012.

[160] B. Pan, B. Wang, G. Lubineau, and A. Moussawi, "Comparison of Subset-Based Local and Finite Element-Based Global Digital Image Correlation," *Experimental Mechanics,* vol. 55, pp. 887-901, 2015.

[161] L. Reimer, *Transmission Electron Microscopy: Physics of Image Formation and Microanalysis* vol. 36: Springer, 2013.

[162] D. A. Muller, E. J. Kirkland, M. G. Thomas, J. L. Grazul, L. Fitting, and M. Weyland, "Room design for high-performance electron microscopy," *Ultramicroscopy,* vol. 106, pp. 1033-1040, 2006.

[163] J. C. Lagarias, J. A. Reeds, M. H. Wright, and P. E. Wright, "Convergence properties of the Nelder–Mead simplex method in low dimensions," *SIAM Journal on Optimization,* vol. 9, pp. 112-147, 1998.

[164] L. Beaulieu, T. Hatchard, A. Bonakdarpour, M. Fleischauer, and J. Dahn, "Reaction of Li with alloy thin films studied by in situ AFM," *Journal of The Electrochemical Society,* vol. 150, pp. A1457-A1464, 2003.

[165] Y. He, X. Yu, G. Li, R. Wang, H. Li, Y. Wang, *et al.*, "Shape evolution of patterned amorphous and polycrystalline silicon microarray thin film electrodes

caused by lithium insertion and extraction," *Journal of Power Sources,* vol. 216, pp. 131-138, 2012.

[166] C. R. Becker, K. E. Strawhecker, Q. P. McAllister, and C. A. Lundgren, "In Situ atomic force microscopy of lithiation and delithiation of silicon nanostructures for lithium ion batteries," *ACS Nano,* vol. 7, pp. 9173-9182, 2013.

[167] K. Laaziri, S. Kycia, S. Roorda, M. Chicoine, J. Robertson, J. Wang, *et al.*, "High-energy x-ray diffraction study of pure amorphous silicon," *Physical Review B,* vol. 60, p. 13520, 1999.

[168] M. Wakagi, K. Ogata, and A. Nakano, "Structural study of a-Si and a-Si: H films by EXAFS and Raman-scattering spectroscopy," *Physical Review B,* vol. 50, p. 10666, 1994.

[169] S. Kugler, L. Pusztai, L. Rosta, P. Chieux, and R. Bellissent, "Structure of evaporated pure amorphous silicon: neutron-diffraction and reverse Monte Carlo investigations," *Physical Review B,* vol. 48, pp. 7685-7688, 1993.

[170] X. Wang, A. Yang, and S. Xia, "Fracture toughness characterization of lithiated germanium as an anode material for lithium-ion batteries," *Journal of The Electrochemical Society,* vol. 163, pp. A90-A95, 2016.

[171] X. J. Wang, F. F. Fan, J. W. Wang, H. R. Wang, S. Y. Tao, A. Yang, *et al.*, "High damage tolerance of electrochemically lithiated silicon," *Nature Communications,* vol. 6, Sep 2015.

[172] S. M. Xia, Y. Qi, T. Perry, and K. S. Kim, "Strength characterization of Al/Si interfaces: A hybrid method of nanoindentation and finite element analysis," *Acta Materialia,* vol. 57, pp. 695-707, Feb 2009.

[173] J. R. Rice, "A Path Independent Integral and Approximate Analysis of Strain Concentration by Notches and Cracks," *Journal of Applied Mechanics,* vol. 35, pp. 379-+, 1968.

[174] H. Haftbaradaran and J. M. Qu, "A path-independent integral for fracture of solids under combined electrochemical and mechanical loadings," *Journal of the Mechanics and Physics of Solids,* vol. 71, pp. 1-14, Nov 2014.

[175] C. F. Shih, B. Moran, and T. Nakamura, "Energy-Release Rate Along a 3-Dimensional Crack Front in a Thermally Stressed Body," *International Journal of Fracture,* vol. 30, pp. 79-102, Feb 1986.

[176] S. C. Chao, Y. C. Yen, Y. F. Song, Y. M. Chen, H. C. Wu, and N. L. Wu, "A study on the interior microstructures of working Sn particle electrode of Li-ion batteries by in situ X-ray transmission microscopy," *Electrochemistry Communications,* vol. 12, pp. 234-237, Feb 2010.

[177] J. W. Wang, F. F. Fan, Y. Liu, K. L. Jungjohann, S. W. Lee, S. X. Mao, *et al.*, "Structural Evolution and Pulverization of Tin Nanoparticles during Lithiation-Delithiation Cycling," *Journal of the Electrochemical Society,* vol. 161, pp. F3019-F3024, 2014.

[178] J. J. Wang, C. Eng, Y. C. K. Chen-Wiegart, and J. Wang, "Probing three-dimensional sodiation-desodiation equilibrium in sodium-ion batteries by in situ hard X-ray nanotomography," *Nature Communications,* vol. 6, Jun 2015.

[179] J. W. Wang, Y. He, F. F. Fan, X. H. Liu, S. M. Xia, Y. Liu, *et al.*, "Two-Phase Electrochemical Lithiation in Amorphous Silicon," *Nano Letters,* vol. 13, pp. 709-715, Feb 2013.

[180] M. T. McDowell, S. W. Lee, J. T. Harris, B. A. Korgel, C. M. Wang, W. D. Nix, *et al.*, "In Situ TEM of Two-Phase Lithiation of Amorphous Silicon Nanospheres," *Nano Letters,* vol. 13, pp. 758-764, Feb 2013.

[181] X. H. Liu, J. W. Wang, S. Huang, F. F. Fan, X. Huang, Y. Liu, *et al.*, "In situ atomic-scale imaging of electrochemical lithiation in silicon," *Nature Nanotechnology,* vol. 7, pp. 749-756, Nov 2012.

[182] F. Gao and W. Hong, "Phase-field model for the two-phase lithiation of silicon," *Journal of the Mechanics and Physics of Solids,* vol. 94, pp. 18-32, 2016.

[183] X. J. Wang, A. Yang, and S. M. Xia, "Fracture Toughness Characterization of Lithiated Germanium as an Anode Material for Lithium-Ion Batteries," *Journal of the Electrochemical Society,* vol. 163, pp. A90-A95, 2016.